EXPERIMENTAL AND NUMERICAL INVESTIGATION OF STEADY-STATE AND TRANSIENT ULTRASOUND DIRECTED SELF-ASSEMBLY OF SPHERICAL PARTICLES IN A VISCOUS MEDIUM

Soheyl Noparast

Dissertation submitted to the faculty of the Virginia Polytechnic Institute and State University in partial fulfillment of the requirements for the degree of

Doctor of Philosophy
In
Mechanical Engineering

Bart Raeymaekers
Fernando Guevara Vasquez
Michael Bartlett
Zhenhua Tian

May 3, 2024
Blacksburg, VA

Keywords: Ultrasound directed self-assembly, acoustic radiation force, acoustic interaction force, medium viscosity, particle volume fraction, particle size, particle packing density, boundary element method, transient, vat photopolymerization, monopole and dipole scattering, single scattering, multiple scattering

EXPERIMENTAL AND NUMERICAL INVESTIGATION OF STEADY-STATE AND TRANSIENT ULTRASOUND DIRECTED SELF-ASSEMBLY OF SPHERICAL PARTICLES IN A VISCOUS MEDIUM

Soheyl Noparast

ABSTRACT

Ultrasound directed self-assembly (DSA) utilizes the acoustic radiation force associated with a standing ultrasound wave field to organize particles dispersed in a fluid medium into specific patterns. The ability to tailor the organization and packing density of spherical particles using ultrasound DSA in a viscous fluid medium is crucial in the context of (additive) manufacturing of engineered materials with tailored properties. However, the fundamental physics of the ultrasound DSA process in a viscous fluid medium, and the relationship between the ultrasound DSA process parameters and the specific patterns of particles that result from it, are not well-understood.

Researchers have theoretically described the acoustic radiation force and the acoustic interaction force that act on spherical particles in a standing ultrasound wave field in both inviscid and viscous media. In addition, they have solved the forward and inverse ultrasound DSA problem in an inviscid medium, in which they relate the patterns of particles and the ultrasound DSA operating parameters. However, no theoretical model exists that allows simulating the steady-state and transient local particle packing density in a viscous medium during ultrasound DSA.

Thus, in this dissertation, we (i) theoretically derive and experimentally validate a model to determine the steady-state locations where spherical particles assemble during ultrasound DSA as a function of medium viscosity and particle volume fraction. (ii) We also theoretically derive and experimentally validate a model to quantify the steady-state and transient local packing density

of spherical particles within the pattern features that result from ultrasound DSA. Using these models, we quantify and predict the locations where spherical particles assemble during ultrasound DSA in a viscous medium, considering the effects of medium viscosity and particle volume fraction. We demonstrate that the deviation between locations where particles assemble in viscous and inviscid media first increases and then decreases with increasing particle volume fraction and medium viscosity, which we explain by means of the sound propagation velocity of the mixture. In addition, we quantify and predict the steady-state and transient local packing density of spherical particles within the pattern features, using ultrasound DSA in combination with vat photopolymerization (VP). We show that the steady-state local particle packing density increases with increasing particle volume fraction and increases with decreasing particle size. We also show that the transient local particle packing density increases with increasing particle volume fraction, decreasing particle size, and decreasing fluid medium viscosity. Increasing particle size and decreasing fluid medium viscosity decreases the time to reach steady-state.

Finally, we implement single and multiple scattering in the calculation of the acoustic radiation force for spherical particles in a viscous medium and quantify their relative contributions to the calculation of the acoustic radiation force as a function of ultrasound DSA operating parameters and material properties. We demonstrate that the deviation between considering single and multiple scattering may reach up to 100%, depending on the ultrasound DSA process parameters and material properties. Also, increasing the particle volume fraction increases the need to account for multiple scattering.

Quantifying and predicting the local packing density of spherical particles during ultrasound DSA in a viscous medium, as a function of ultrasound DSA process parameters is crucial towards using ultrasound DSA in engineering applications, in particular (additive)

manufacturing of engineered polymer matrix composite materials with tailored properties whose properties depend on the spatial organization and packing density of particles in the matrix material.

EXPERIMENTAL AND NUMERICAL INVESTIGATION OF STEADY-STATE AND TRANSIENT ULTRASOUND DIRECTED SELF-ASSEMBLY OF SPHERICAL PARTICLES IN A VISCOUS MEDIUM

Soheyl Noparast

GENERAL AUDIENCE ABSTRACT

Ultrasound directed self-assembly (DSA) is a technique that uses ultrasound waves to arrange small particles submerged in a fluid into specific patterns. When combined with other manufacturing techniques, ultrasound DSA can be used to fabricate composite materials that derive their properties from the spatial organization of particles in a matrix material. However, ultrasound DSA in viscous fluids is not well-understood. Researchers have studied the forces associated with ultrasound waves that move small spherical particles in an inviscid fluid medium (fluids that experience little to no internal resistance to flow), and they have demonstrated intricate control of the patterns of particles that form using ultrasound DSA. However, that knowledge is not currently available for ultrasound DSA in viscous media.

In this dissertation, we develop and evaluate theoretical models to understand ultrasound DSA of small spherical particles in a viscous fluid medium. We simulate where particles organize and how densely they pack together. We also determine the difference of the time-dependent motion of particles in a viscous fluid compared to that in an inviscid fluid medium and relate the difference to the number of particles submerged in the fluid and the viscosity of the fluid. Additionally, we examine the effect of particle size and fluid viscosity on the speed by which the particles reach their final location. We also study how ultrasound waves interact with multiple small particles in a viscous fluid, focusing on the forces that move these particles. We explore two models that account for single and multiple ultrasound wave scattering. Scattering is the process

by which ultrasound waves deflect in different directions when they encounter a particle. The results show that the difference between single and multiple scattering models can be significant, depending on the ultrasound DSA process parameters and the properties of the fluid and particles. In general, the importance of accounting for multiple scattering increases with the number of particles submerged in the fluid.

Understanding particle packing density when using ultrasound DSA in a viscous fluid is essential in many engineering applications, in particular manufacturing of composite materials that derive their properties from the spatial arrangement of particles in a matrix material.

TABLE OF CONTENTS

LIST OF FIGURES

LIST OF TABLES

LIST OF ABBREVIATIONS AND SYMBOLS

Abbreviation and Symbol	Unit	Description
$\|\|\bullet\|\|$	-	Norm of a vector
$\langle\bullet\rangle$	-	Time average of harmonic time-dependent functions
$\partial\bullet/\partial\bullet$	-	Partial derivative
$\partial\Omega$	-	Control volume surface
$\nabla\bullet$	-	Gradient
$\bullet^*$	-	The complex conjugate
1D		One-dimensional
2D	-	Two-dimensional
3D	-	Three-dimensional
a	m	Particle radius
B	-	Boundary
BEM	-	Boundary element method
c_{exp}	m/s	Experimental sound propagation velocity of the mixture
c_m	m/s	Wave propagation velocity
$c_{p,c}$	m/s	Compressional wave propagation velocity of the particle
$c_{p,m}$	J/(kg K)	Specific heat of the medium
$c_{p,s}$	m/s	Shear wave propagation velocity of the particle
c_{th}	m/s	Simulation sound propagation velocity of the mixture
D	-	Domain
d_{33}	m/V	Piezoelectric strain constant
d_{inv}	m	Distance between adjacent lines where particles assemble in an inviscid medium
DIW	-	Direct ink writing
DLP	-	Digital light processing
DNA	-	Deoxyribonucleic acid
DSA	-	Directed self-assembly
d_{vis}	m	Distance between adjacent lines where particles assemble in a viscous medium
E	-	Deviation
E_{exp}	-	Experimental deviation
E_{max}	-	Maximum deviation
E_{sim}	-	Simulation deviation
f	Hz	Temporal frequency
$\mathbf{F}$		Acoustic radiation force
f_1	-	Monopole scattering coeficcient
f_2	-	Dipole scattering coeficcient
$\mathbf{F}_b$	N	Buoyancy force
f_c	Hz	Ultrasound transducer center frequency
$\mathbf{F}_d$	N	Drag force
f_{exp}	Hz	Experimental frequency
FFF	-	Fused filament fabrication
$\mathbf{F}_g$	N	Gravity force
$\mathbf{F}_{inc}$	N	Primary acoustic radiation force
$\mathbf{F}_{int}$	N	Acoustic interaction force
$\mathbf{F}_{LJ}$	N	Lennard-Jones-like force
$F_{multiple}$	N	Acoustic radiation force with multiple scattering
f_{sim}	Hz	Simulation frequency
F_{single}	N	Acoustic radiation force with single scattering
$G(\bullet)$	-	Green's function for the Helmholtz equation
$h_0^{(1)}(\bullet)$	-	0^{th} order spherical Hankel function of the first kind

$h_1^{(1)}(\bullet)$	-	1st order spherical Hankel function of the first kind
$h_2^{(1)}(\bullet)$	-	2nd order spherical Hankel function of the first kind
i	-	Imaginary unit
$\mathbf{I}$	-	Identity matrix
k	1/m	Wave number of the ultrasound wave
$\tilde{k}$	1/m	Complex wave number
K_1	-	Non-dimensional particle size
K_2	-	Non-dimensional medium viscosity
K_3	-	Nondimensional time
K_3^*	-	Nondimensional packing time
L	m	Distance between ultrasound transducers
$\mathbf{n}$	-	Unit normal vector
N	-	Number of particles
N_b	-	Number of boundary elements
N_d	-	Number of domain points
p	Pa	Pressure
p_0	Pa	Zeroth order pressure
p_1	Pa	First order pressure
p_2	Pa	Second order pressure
PD	-	Local particle packing density
PD_{exp}	-	Experimental local particle packing density
PD_{sim}	-	Simulation local particle packing density
p_{inc}	Pa	Incident pressure
PVDF	-	Polyvinylidene difluoride
PZT	-	Lead zirconate titanate
q	m	Center point of a boundary element
$\mathbf{r}$	m	Particle location
$\mathrm{R}\{\bullet\}$	-	Real part of the expression
Re	-	Reynolds number
RF	-	Radio frequency
t, T	s	Time
U		Acoustic radiation potential
$\mathbf{u}$	m	Particle velocity
U_{inc}	N m	Primary acoustic radiation potential
U_{int}	N m	Acoustic interaction potential
$\mathbf{v}$	m^2/s	Velocity
$\mathbf{v}_0$	m/s	Zeroth order velocity
$\mathbf{v}_1$	m/s	First order velocity
$\mathbf{v}_2$	m/s	Second order velocity
v_{inc}	m/s	Incident velocity
VP	-	Vat photopolymerization
$V_{p\text{-}p}$	V	Input peak-to-peak voltage of the ultrasound transducers
w	m	Width of a domain around a node
$\tilde{Z}$	-	Impedance ratio
Z_b	Ry	Acoustic impedance of the boundary
Z_m	Ry	Acoustic impedance of the medium
β_m	m^2/N	Medium compressibility
β_p	m^2/N	Particle compressibility
δ	m	Viscous boundary layer thickness
$\delta PD_{sim}/\delta K_3$	-	Nondimensional packing rate
Δt	s	Time step
δ_t	m	Depth of penetration of the thermal wave
ε	m	width of a boundary element

ε_{LJ}	N m	Lennard-Jones-like potential coefficient
η_m	Pa s	Viscosity of the fluid medium
κ_m	W/(m K)	Thermal conductivity of the medium
λ	m	Wavelength of the ultrasound wave
π	-	Ratio of circumference of a circle to its diameter
ρ	kg/m^3	Density
ρ_0	kg/m^3	Zeroth order density
ρ_1	kg/m^3	First order density
ρ_2	kg/m^3	Second order density
ρ_{inc}	kg/m^3	Incident density
ρ_m	kg/m^3	Medium density
ρ_p	kg/m^3	Particle density
τ_s	s	Relaxation time
τ_s	s	Relaxation time
φ	m^2/s	Velocity potential
Φ	-	Particle volume fraction
ϕ	-	Acoustic contrast factor
φ_0	m^2/s	Amplitude of the velocity potential of the ultrasound wave
φ_{inc}	m^2/s	Incident velocity potential
φ_{sc}	m^2/s	Scattering velocity potential
$\varphi_{sc,di}$	m^2/s	Dipole scattering velocity potential
$\varphi_{sc,mono}$	m^2/s	Monopole scattering velocity potential
ω	rad/s	Angular frequency

CHAPTER 1

INTRODUCTION

1.1. Directed self-assembly

Directed self-assembly (DSA) is a process by which particles spontaneously organize due to interactions between the particles and their environment, driven by internal or external forces [1]. DSA categorizes as templated, template-free, or external field-based techniques [2].

Figure 1.1 (a) schematically illustrates the templated DSA process. It is based on mechanical [3] or chemical [4] modification of the surface of a substrate, which create regions of attraction that selectively prompt particle deposition on that substrate. Templated DSA may involve a soft template, where user-specified regions of attraction on the substrate surface control the assembly of particles, or hard templates, where the geometry of the substrate surface controls the assembly of particles [5]. Figure 1.1 (b) shows an example of soft-templated DSA that uses a silicon oxide substrate with periodically spaced regions of attraction that cause silica particles to deposit on the substrate surface in a periodic pattern [6]. Additionally, Figure 1.1 (c) shows an example of hard-templated DSA that uses a mosaic virus with regions of attraction on the virus surface to cause the deposition of gold particles in a tubular pattern [7]. Due to the complex manufacturing techniques that are required to implement the templates, templated DSA methods typically limit template sizes to nano- or micrometer scale dimensions [6,7].

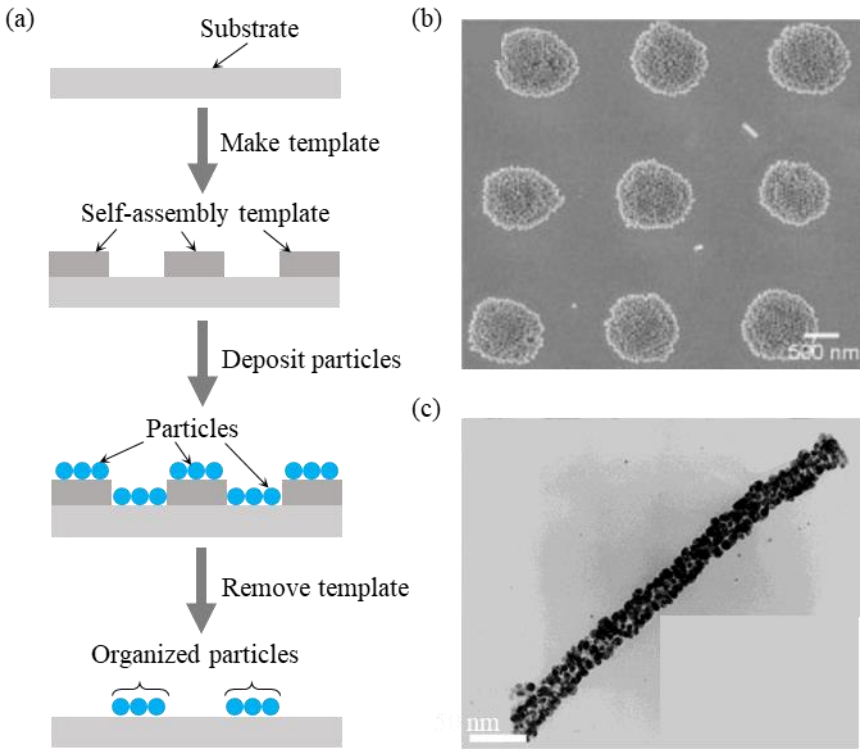

Figure 1.1: (a) Schematic of the templated DSA process. (b) Example of soft-templated DSA using a silicon oxide substrate with regions of attraction that drive the deposition of silica particles in a periodic pattern [6]. (c) Example of hard-templated DSA using a mosaic virus substrate with areas of attraction to compel the deposition of gold particles in a tubular pattern [7]. Images reprinted with permission.

Figure 1.2 (a) schematically illustrates the template-free DSA process. The process relies on capping molecules that interact with each other and with particles dispersed in a medium. The interactions to arrange the particles into nano- or microscale structures [2]. Figure 1.2 (b) shows an example of template-free DSA that uses deoxyribonucleic acid (DNA) capping molecules to organize gold nanorods into specific patterns [8]. The interactions between the capping molecules and particles are triggered through external stimuli such as light [9] and temperature [10], amongst other examples. Template-free DSA does not allow tailoring the nano- or microscale structure that results from the DSA process because the material properties and geometry of the capping molecules and particles control the result [8–10].

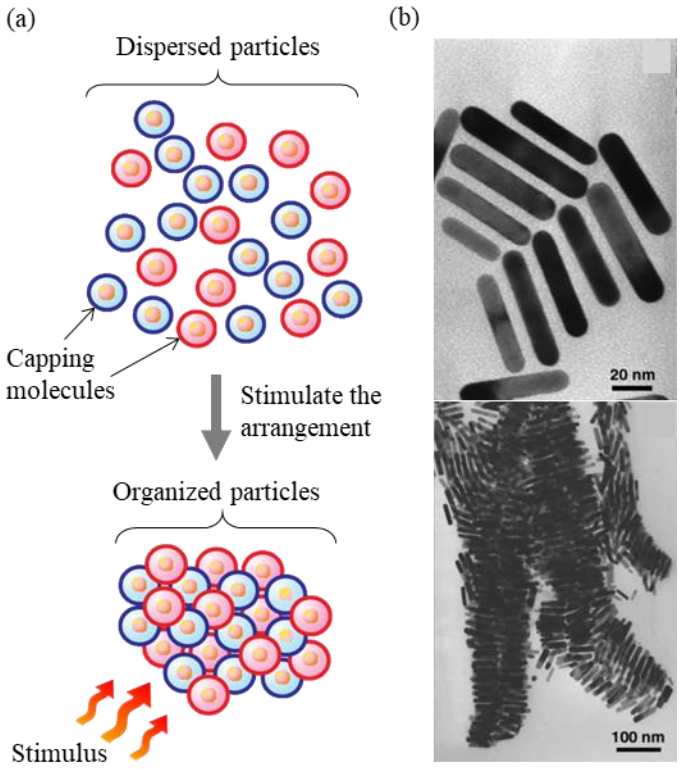

Figure 1.2: (a) Schematic of the template-free DSA process. (b) Example of template-free DSA that uses aligned gold nanorods and DNA capping molecules [8]. Images reprinted with permission. Images reprinted with permission.

Figure 1.3 (a) schematically illustrates external field DSA methods, which utilize forces that derive from shear stress [11], electric [12], magnetic [13], and standing ultrasound wave fields [14] to organize and orient particles into specific patterns. Additionally, Figure 1.3 shows examples of external field DSA processes, including (b) electric field DSA of gold nanoparticles into a microwire structure using a high-strength electrostatic field [12], (c) magnetic field DSA of ferromagnetic particles, i.e., polystyrene particles coated with iron, which orient in the direction of the magnetic force [13], and (d) ultrasound DSA of carbon microfibers in photopolymer resin using a standing ultrasound wave field [14].

Electric and magnetic field DSA are restricted to organizing particles with specific electric or magnetic properties, respectively. Moreover, they require ultra-high electric (20 kV/m [15]) or

magnetic field strength (80 kOe [16]), which limits the scalability of the process. On the other hand, ultrasound DSA uses a standing ultrasound wave to organize and orient particles dispersed in a fluid medium into specific patterns [14]. Ultrasound DSA does not require ultra-high field strengths to organize particles in low-viscosity media [17], which enables scalability over macroscale distances, areas, and volumes. Furthermore, the existence of the acoustic radiation force is only dependent on the acoustic contrast between the particles and the medium, which derives from their density and compressibility [18].

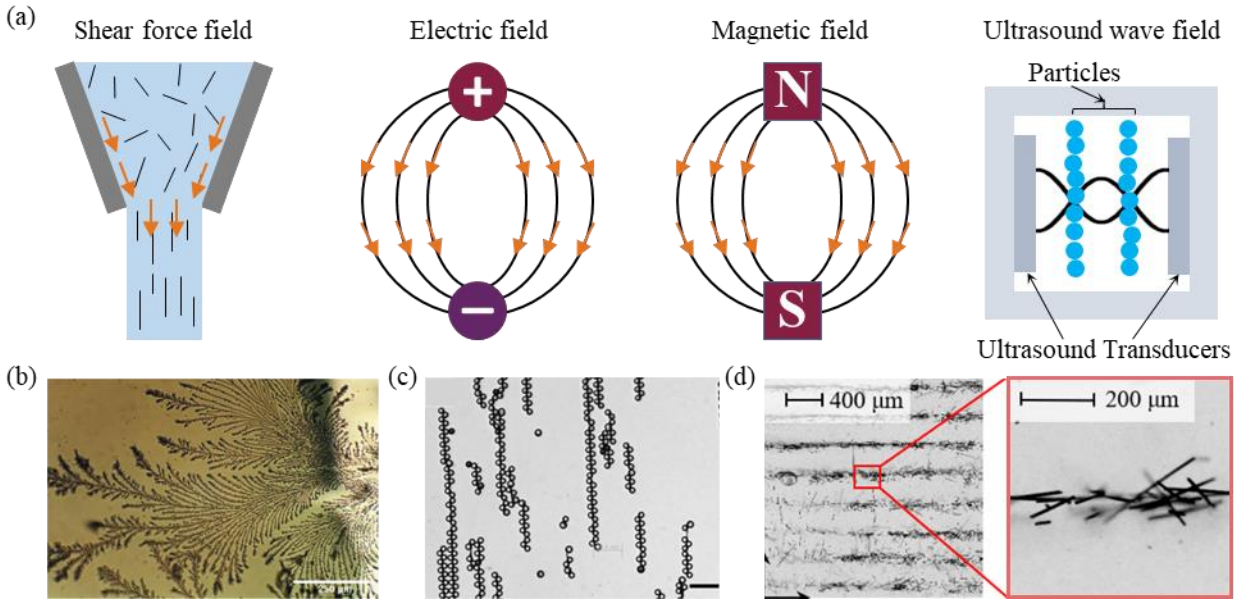

Figure 1.3: (a) Schematic of external field DSA processes, including shear, electric, magnetic, and ultrasound fields. (b) Example of electric field DSA, showing the assembly of gold nanoparticles into a microwire structure [12]. (c) Example of magnetic field DSA, showing an organized chain of ferromagnetic particles [13]. (d) Example of ultrasound DSA showing carbon microfibers organized in line patterns with both macroscale and microscale alignment [14]. Images reprinted with permission.

1.2. Ultrasound directed self-assembly

Ultrasound DSA allows organizing and orienting particles dispersed in a fluid medium into specific patterns, driven by the time-averaged acoustic radiation force that results from scattering of the ultrasound wave [19]. Figure 1.4 shows a typical experimental setup for ultrasound DSA experiments, which consists of an acrylic reservoir with two ultrasound transducers affixed to two

opposing reservoir walls. The reservoir contains a fluid medium with dispersed spherical particles. An ultrasound transducer converts electrical energy (input) to mechanical vibration (output). Hence, energizing both ultrasound transducers with a function generator and radio frequency (RF) amplifier creates a high-frequency standing pressure wave, i.e., a standing ultrasound wave, which organizes the particles into specific patterns (line pattern in Fig. 1.4) that coincide with the nodes of the standing ultrasound wave (Fig. 1.4 inset).

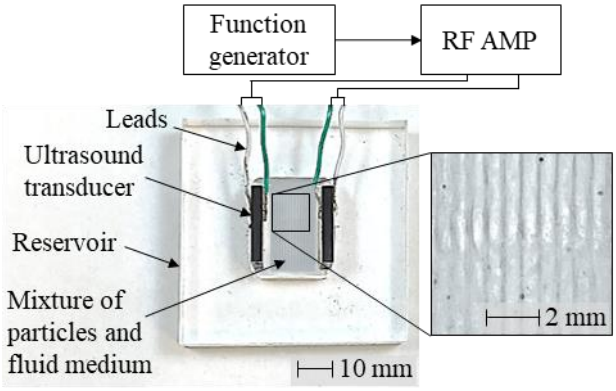

Figure 1.4: Typical setup for an ultrasound DSA experimental, showing the assembly of line patterns of spherical particles dispersed in a fluid medium [20]. Figure reprinted with permission.

The following sections explain the fundamental knowledge required to understand the ultrasound DSA process. We introduce ultrasound waves in Sec. 1.3, ultrasound wave scattering, and the acoustic radiation force in Sec. 1.4, and then relate the organization and orientation of particles to the ultrasound DSA process parameters in Sec. 1.5.

1.3. Ultrasound waves

1.3.1. Concepts and terminology

Mechanical vibrations applied to elastic media produce acoustic waves [21]. Ultrasound waves are the subset of acoustic waves with a frequency f higher than the audible limit of human hearing, i.e., f > 20 kHz [17]. Generally, acoustic waves, including ultrasound waves, can

propagate as a transverse wave (in a solid medium), which causes alternating shear stress orthogonal to the direction of wave propagation, or as a longitudinal wave (in solid, liquid, and gas media), which results in periodic regions of compression and rarefaction [22]. Figure 1.5 schematically illustrates (a) an undeformed elastic medium, (b) a transverse wave propagating in an elastic medium, and (c) a longitudinal wave propagating in an elastic medium.

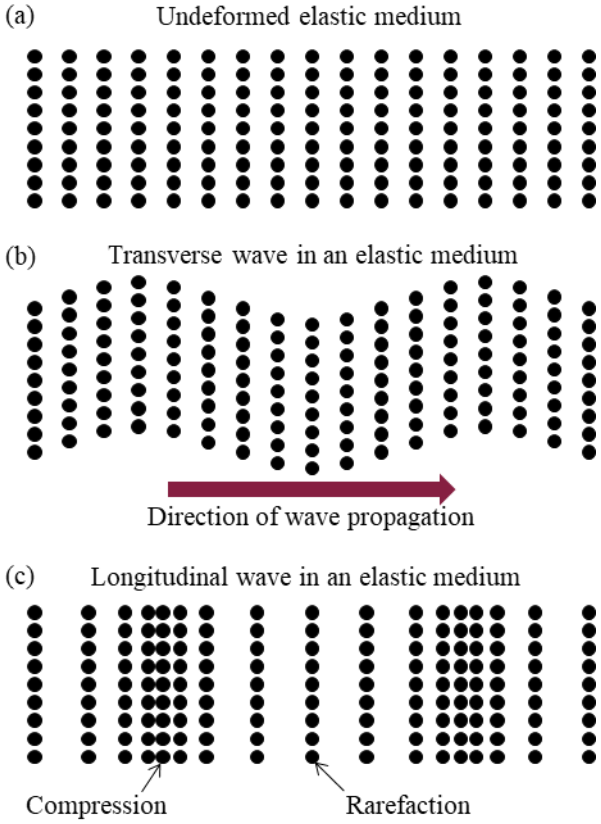

Figure 1.5: Schematic illustration of (a) an undeformed elastic medium, (b) a transverse wave propagating in an elastic medium, and (c) a longitudinal wave propagating in an elastic medium. The direction of wave propagation shows as a maroon arrow, and we illustrate regions of compression and rarefaction by means of the compaction of black dots.

Ultrasound DSA relies on longitudinal ultrasound waves in a fluid medium. A longitudinal ultrasound wave in a fluid medium travels by generating regions of compression that coincide with high pressure, high density, and low velocity, and regions of rarefaction that coincide with low pressure, low density, and high velocity. We describe a traveling ultrasound wave in a fluid

medium as the incident velocity potential φ_{inc}. Thus, a one-dimensional (1D) ultrasound wave that travels in the x-direction through an inviscid fluid medium is given as [17]

$$\varphi_{inc} = \Re\{-\varphi_0 i e^{ikx}\}, \tag{1.1}$$

where $\mathrm{R}\{\bullet\}$ is an operator that extracts the real part of the expression, and $i = (-1)^{1/2}$. We define φ_0 the amplitude of the velocity potential of the ultrasound wave, and $k = 2\pi/\lambda$ is the wave number, with $\lambda = 2\pi c_m/\omega$ the wavelength of the ultrasound wave. Also, x is the length coordinate along the propagation direction of the ultrasound wave, and $\omega = 2\pi f$ and f are the angular and temporal frequencies of the ultrasound wave, respectively. Furthermore, $c_m = (1/\rho_m\beta_m)^{1/2}$ is the wave propagation velocity of the fluid medium that depends on the medium density ρ_m and the medium compressibility β_m.

Figure 1.6 schematically illustrates the pulse-echo technique to measure the wave propagation velocity of the fluid medium c_m [23]. An ultrasound transducer emits an ultrasound pulse in the x-direction. The ultrasound pulse travels the distance L through the fluid medium (so-called pulse), reflects off a reflector, travels the distance L back through the fluid medium (so-called echo), and again reaches the ultrasound transducer. The wave propagation velocity of the fluid medium $c_m = 2L/\Delta t$, where Δt is the travel time of the ultrasound pulse from the ultrasound transducer to the reflector and back to the ultrasound transducer.

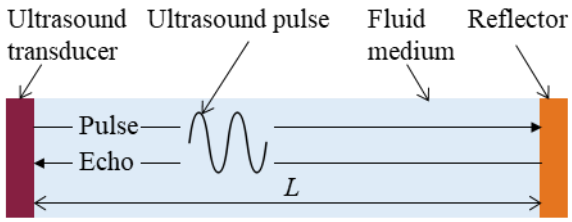

Figure 1.6: Schematic of the pulse-echo technique to measure the wave propagation velocity of a fluid medium c_m.

When considering a viscous instead of an inviscid medium, we must account for attenuation of the ultrasound wave while it travels through the viscous fluid medium. Hence, a 1D ultrasound wave that travels in the x-direction through a viscous fluid medium is given as [17]

$$\varphi_{inc} = \Re\{-\varphi_0 i e^{i\tilde{k}x}\}, \tag{1.2}$$

where $\tilde{k} = (\omega/c_m)/(1-i\omega\tau_s)^{1/2}$ is the complex wave number that accounts for ultrasound wave attenuation in a viscous medium [17]. Here, $\tau_s = 4\eta_m/3\rho_m c_m^2$ is the relaxation time, i.e., the viscous dissipation time required to dampen the acoustic pressure to $1/e$ of its original value, and η_m is the viscosity of the fluid medium. Figure 1.7 compares the normalized amplitude (in arbitrary units) of an ultrasound wave in an inviscid and viscous medium as it propagates in the x-direction, illustrating the attenuation of the ultrasound wave in the viscous medium.

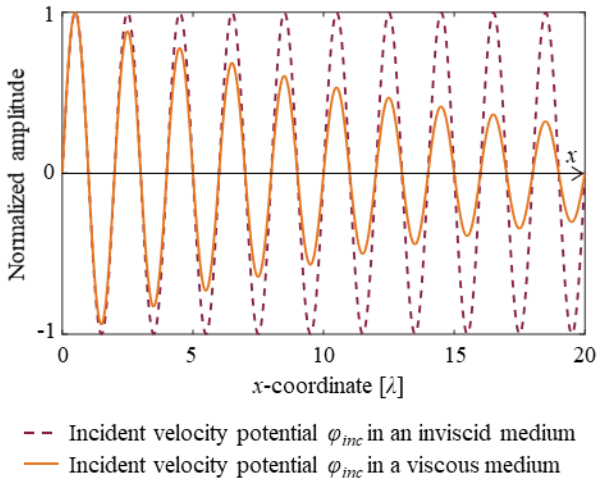

Figure 1.7: Comparison between the normalized amplitude of an ultrasound wave in an inviscid and viscous medium, illustrating the attenuation of the ultrasound wave in the viscous medium.

The interaction between two ultrasound waves with the same frequency f that propagate in a fluid medium in the same direction but with opposite sense results in a standing ultrasound wave. A 1D standing ultrasound wave in the x-direction in an inviscid fluid medium is given as [17]

$$\varphi_{inc} = \Re\{-\varphi_0 i(e^{ikx}-e^{-ikx})\}. \tag{1.3}$$

We derive the ultrasound wave velocity $v_{inc} = -\partial\varphi_{inc}/\partial x$ and pressure $p_{inc} = i\rho_m\omega\varphi_{inc}$ from the incident velocity potential φ_{inc}. A standing ultrasound wave shows nodes at locations where the pressure $p_{inc} = 0$, and antinodes at locations where the pressure oscillates between the minimum and maximum values. Figure 1.8 illustrates the normalized amplitude of the incident velocity potential, velocity, and pressure of a 1D standing ultrasound wave in an inviscid medium, as a function of the x-coordinate in the wave propagation direction. We indicate the locations of the nodes (solid black dots) and antinodes (hollow black dots).

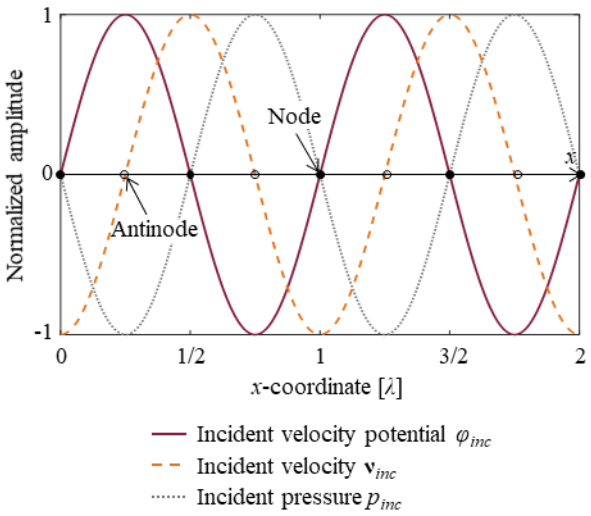

Figure 1.8: Normalized amplitude of the velocity potential φ_{inc}, velocity v_{inc}, and pressure p_{inc} of a 1D standing ultrasound wave as a function of the x-coordinate in the wave propagation direction, showing the locations of the nodes (solid black dots) and antinodes (hollow black dots) of the standing ultrasound wave.

1.3.2. Ultrasound wave generation

An ultrasound transducer converts electrical energy into mechanical energy or vice versa to emit or sense an ultrasound wave (continuous or pulse). An ultrasound transmitter emits ultrasound waves, whereas an ultrasound receiver senses them. An ultrasound transceiver emits and senses ultrasound waves [24]. Figure 1.9 shows examples of commercially available ultrasound transducers (transceivers).

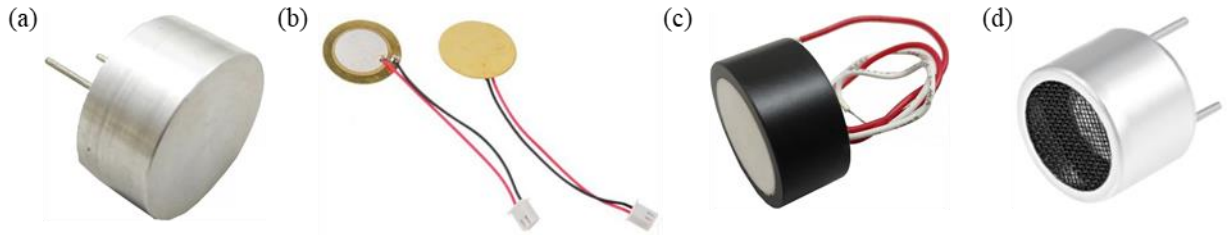

Figure 1.9: Examples of commercially available ultrasound transducers from (a) [25], (b) [26], (c) [27], and (d) [28]. These images are reprinted from their respective source of references. Source: (a) https://www.pzttransducer.com/sale-12680496-sealed-waterproof-ultrasonic-sensor-25khz-center-frequency-diameter-25mm.html (b) https://www.auroraprosci.com/piezoelectric-disc--iameter-27-mm-thin-thickness-0.22-mm (c) https://www.pzttransducer.com/sale-12679425-25mmx12mm-pzt-ultrasonic-transducer-112khz-ultrasonic-piezoelectric-transducer.html (d) https://www.uxcell.com/tct4016t-ultrasonic-transducer-transmitter-probe-2pcs-p-1652326.html.

Different types of ultrasound transducers exist, such as magnetostrictive [24], photoacoustic [29], and piezoelectric [30] ultrasound transducers. Magnetostrictive ultrasound transducers emit ultrasound waves based on expanding and contracting ferromagnetic materials in an alternating magnetic field [31]. A photoacoustic ultrasound transducer emits ultrasound waves based on intensity-modulated absorption of light in an elastic material [32]. Piezoelectric ultrasound transducers emit ultrasound waves based on strained crystalline lattices caused by electrical polarization. Hence, energizing a piezoelectric ultrasound transducer with an alternating voltage with frequency $f > 20$ kHz causes the transducer to expand and contract with frequency f. It acts like a piston source and emits the ultrasound wave into the surrounding fluid medium [33].

Figure 1.10 shows a schematic of the piezoelectric effect in a quartz crystal comprising silicon atoms with a positive charge and oxygen atoms with a negative charge. An alternating voltage source V energizes the quartz crystal in its undeformed state (Fig. 1.10 (a)), contracts it (Fig. 1.10 (b)), and expands it (Fig. 1.10 (c)) as a result of attractive and repulsive forces between the atoms. Figure 1.10 illustrates the positive and negative electrical charges of atoms and the charge accumulated on the quartz crystal as + and – signs.

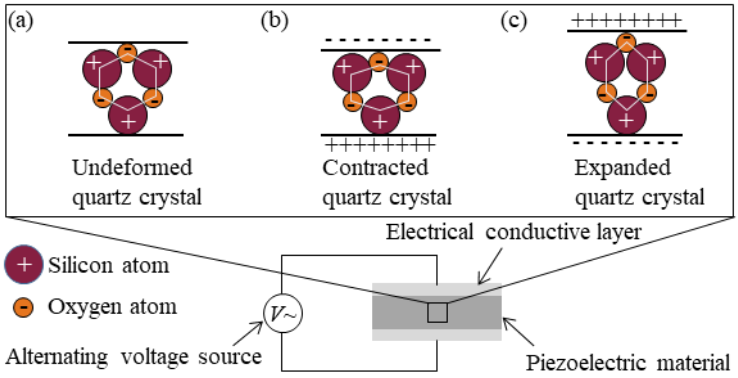

Figure 1.10: Schematic illustration of the piezoelectric effect of a quartz crystal that comprises silicon atoms (maroon) with positive electrical charge and oxygen atoms (orange) with negative electrical charge. (a) Undeformed quartz crystal where $V = 0$, (b) contracted quartz crystal, and (c) expanded quartz crystal due to electrical bias caused by the alternating voltage source.

Piezoelectric materials convert electrical to mechanical energy and vice versa, show stability over a wide range of temperatures, and can operate in dirty and corrosive environments. Thus, piezoelectric materials are commonly used as ultrasound transducers [34]. We use piezoelectric ultrasound transducers for all experiments in this dissertation research.

Several materials show piezoelectric effects, including minerals such as quartz, Berlinite, Topaz, tourmaline, and Rochelle salt, polymers such as polyimide and polyvinylidene difluoride (PVDF), and organic materials such as wood and bone [33]. However, ultrasound transducers commonly use synthetic lead zirconate titanate (PZT) ceramics as their active element because of their low dielectric energy loss, strong dielectric coupling, and high efficiency in converting electrical to mechanical energy [35]. The manufacturing process, chemical composition, and geometry of PZT ultrasound transducers determine their piezoelectric properties. Hence, controlling these parameters allows tuning PZT ultrasound transducers for a specific condition, such as a particular frequency or bandwidth requirement. Figure 1.11 shows examples of the PZT plates with different center frequencies f_c we use for the experiments in this dissertation research

(PZT Type II, Steminc, FL, USA) [36]. The PZT material is covered with a silver coating on either side, which are electrodes to which one can connect leads.

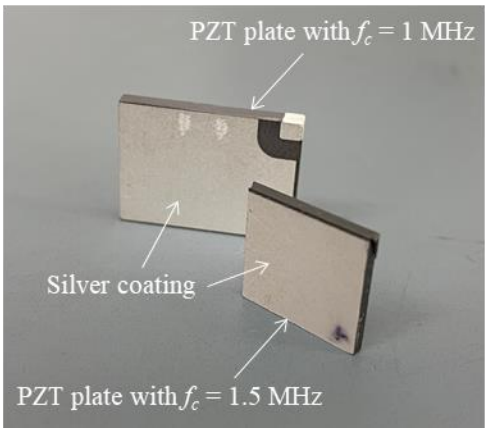

Figure 1.11: Examples of the PZT plates with different center frequencies f_c we use for the experiments in this dissertation research.

1.4. Acoustic radiation force

1.4.1. Acoustic wave scattering

Figure 1.11 shows a spherical particle (gray) of radius a in a fluid medium (light blue), subject to an incident ultrasound wave φ_{inc}. When the incident wave interacts with the surface of the particle, it causes alternating movements and shape changes of the spherical particle with the same frequency as the incident ultrasound wave φ_{inc}. Thus, as a result of these alternating movements and shape changes, the particle emits an ultrasound wave into the fluid medium. This ultrasound wave that emits from the particle is a scattered wave φ_{sc}. In this dissertation research, we note that the incident and scattered ultrasound wave refers to the incident and scattered velocity potentials.

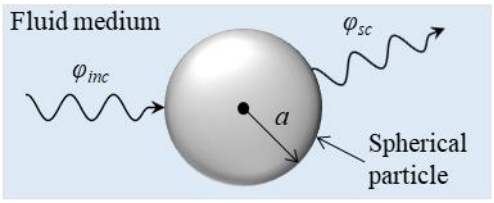

Figure 1.12: Schematic of the interaction between an incident ultrasound wave φ_{inc} and a spherical particle of radius a in a fluid medium, showing the scattered wave φ_{sc} that emits from the particle as a result of alternating movement and shape changes induced by the incident wave φ_{inc}.

Researchers have studied the scattered wave that results from a spherical particle dispersed in a fluid medium, subject to an incident wave. These studies started in 1934 when King examined scattering for incompressible spherical particles in an inviscid medium [37]. Subsequently, researchers have analyzed wave scattering for elastic spherical and cylindrical particles in an inviscid medium [38], elastic spherical particles in a thermoviscous medium [39], and ellipsoidal particles in a poroelastic medium [40].

Three wave scattering regimes for spherical particles exist, which we categorize by means of the relationship between the wavelength λ and the particle radius a and. Figure 1.13 schematically illustrates the Rayleigh regime, where the particle radius a is much smaller than the wavelength ($a << \lambda$) (Fig. 1.13 (a)), the Mie regime, where the particle radius and the wavelength are on the same order of magnitude ($a \approx \lambda$) (Fig. 1.13 (b)), and the Ray regime, where the particle radius is significantly larger than the wavelength ($a >> \lambda$) (Fig. 1.13 (c)). Comparing the Rayleigh regime versus the Mie and Ray regime, we note that the scattered wave is weaker in the Rayleigh regime than in the other regimes because the ratio of the radiation power that scatters from a spherical particle and the incident radiation power is proportional to $(ka)^4$ for spherical particles in a standing ultrasound wave [41].

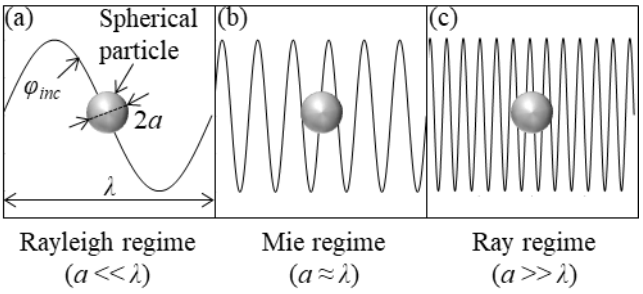

Figure 1.13: Schematic illustration of (a) Rayleigh, (b) Mie, and (c) Ray scattering regimes, showing the relationship between the wavelength of the incident ultrasound wave φ_{inc} and the radius a of the spherical particle.

In this dissertation research, we focus on spherical microparticles (5 μm ≤ a ≤ 30 μm) dispersed in fluid medium and subject to a standing ultrasound wave of frequency f ≤ 1.5 MHz. When considering water-like fluid media with c_m ≈ 1,500 m/s, the wavelength of the ultrasound wave λ ≈ 1 mm. Thus, the radius of the particles is substantially smaller than the wavelength of the ultrasound wave, and the system operates in the Rayleigh regime. In this regime, the scattered wave emitted from a spherical particle in a standing ultrasound wave can be described as a multipole expansion, where the monopole and dipole components dominate. The boundary conditions are; (1) the pressure in the fluid medium equals the normal stress in the spherical particle, (2) no shear stress exists at the particle surface, and (3) the fluid medium does not penetrate the particle [18]. The monopole scattering velocity potential from a particle located at $\boldsymbol{r}_j$ and measured in $\boldsymbol{r}_i$ is given as [42]

$$\varphi_{sc,mono}(\mathbf{r}_i \mid \mathbf{r}_j) = -i(ka)^3 \left[\frac{f_1}{3} h_0^{(1)}(k\|\mathbf{r}_i - \mathbf{r}_j\|)\varphi_{inc}(\mathbf{r}_j) \right], \tag{1.4}$$

where the monopole scattering coefficient $f_1 = 1-\beta_p/\beta_m$ [43]. Here, the particle compressibility $\beta_p = 1/[\rho_p(c_{p,c}^2 - 4c_{p,s}^2/3)]$, where ρ_p, $c_{p,c}$ and $c_{p,s}$ are the density, compressional wave propagation velocity, and shear wave propagation velocity of the spherical particle, respectively [18]. $h_0^{(1)}(z) = -ie^{iz}/z$ is the 0th order spherical Hankel function of the first kind [44]. $\|\mathbf{r}_i - \mathbf{r}_j\|$ is the Euclidean

distance between locations $\mathbf{r}_i$ and $\mathbf{r}_j$, which are vectors with respect to the origin of a Cartesian coordinate system. Figure 1.14 (a) schematically illustrates the monopole scattering velocity potential $\varphi_{sc,mono}$ emitted from a spherical particle in a standing ultrasound wave, which generates an ultrasound wave originating from the spherical particle with a uniform amplitude in all directions.

The dipole scattering velocity potential from a particle located at $\mathbf{r}_j$ and measured in $\mathbf{r}_i$ is given as [42]

$$\varphi_{sc,di}(\mathbf{r}_i \mid \mathbf{r}_j) = -i(ka)^3 \left[-\frac{f_2}{2} h_1^{(1)}(k\|\mathbf{r}_i - \mathbf{r}_j\|) \frac{\partial \varphi_{inc}(\mathbf{r}_j)}{\partial (k\|\mathbf{r}_i - \mathbf{r}_j\|)} \right], \quad (1.5)$$

where the dipole scattering coefficient $f_2 = [2(\rho_p/\rho_m\text{-}1)]/[2\rho_p/\rho_m+1]$. ρ_p is the density of the spherical particle, $h_1^{(1)}(z) = -e^{iz}(z+i)/z^2$ is 1st order spherical Hankel function of the first kind [44], and $\partial \varphi_{inc}(\mathbf{r}_j) / \partial \|\mathbf{r}_i - \mathbf{r}_j\|$ is the derivative of the incident velocity potential at location $\mathbf{r}_j$ in the direction of $\mathbf{r}_i$-$\mathbf{r}_j$. Figure 1.14 (b) schematically illustrates the dipole scattering velocity potential $\varphi_{sc,di}$ emitted from a spherical particle in a standing ultrasound wave, which generates an ultrasound wave originating from the spherical particle in the positive and negative *x*-direction, i.e., the propagation direction of the incident wave.

The scattered velocity potential φ_{sc} from a particle located at $\mathbf{r}_j$ and measured in $\mathbf{r}_i$ is the summation of both monopole $\varphi_{sc,mono}$ and dipole scattering velocity potential $\varphi_{sc,di}$ [42], i.e.,

$$\varphi_{sc}(\mathbf{r}_i \mid \mathbf{r}_j) = -i(ka)^3 \left[\frac{f_1}{3} h_0^{(1)}(k\|\mathbf{r}_i - \mathbf{r}_j\|) \varphi_{inc}(\mathbf{r}_j) - \frac{f_2}{2} h_1^{(1)}(k\|\mathbf{r}_i - \mathbf{r}_j\|) \frac{\partial \varphi_{inc}(\mathbf{r}_j)}{\partial (k\|\mathbf{r}_i - \mathbf{r}_j\|)} \right]. \quad (1.6)$$

Figure 1.14 (c) schematically illustrates the scattered velocity potential φ_{sc} from a spherical particle in a standing ultrasound wave. Note that the relative magnitudes of the monopole and dipole

contributions to φ_{sc} in Fig. 1.14 are for illustration purposes only and, in reality, depend on multiple parameters (Chapter 5).

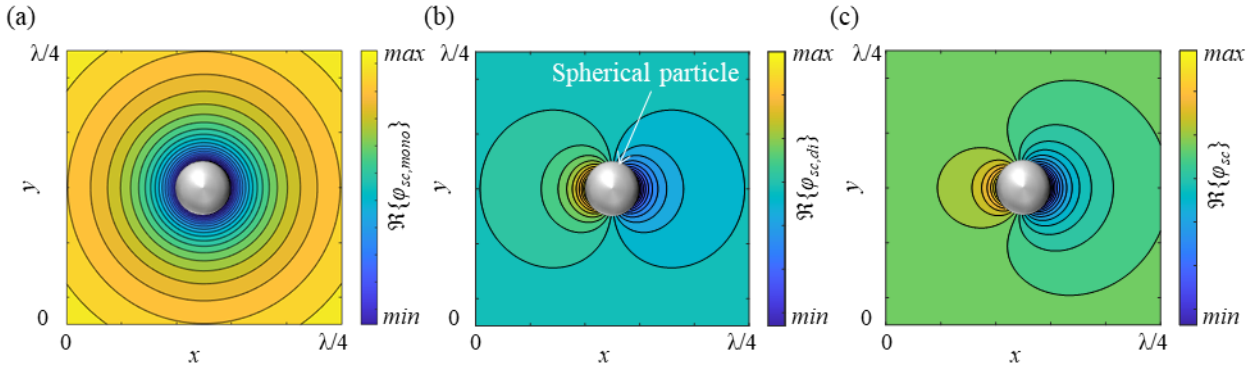

Figure 1.14: Schematic illustration of (a) the monopole scattering velocity potential $\varphi_{sc,mono}$, (b) the dipole scattering velocity potential $\varphi_{sc,di}$, and (c) the scattering velocity potential φ_{sc} from a spherical particle in a standing ultrasound wave.

1.4.2. Primary acoustic radiation force

The standing ultrasound wave transfers momentum to the spherical particle via the radiation pressure applied to the surface of the spherical particle. The time-averaged primary acoustic radiation force $\mathbf{F}_{inc}$ that acts on a spherical particle is the integral of the radiation pressure over the surface of the spherical particle [45]. Theoretical work to calculate the acoustic radiation force began in the 1930s with King [46], who calculated the primary acoustic radiation force that acts on an incompressible spherical particle in an inviscid medium. Yosioka and Kawasima [47] extended King's analysis to compressible spherical particles in an inviscid medium. In 1962, Gor'kov [48] generalized these results in a primary acoustic radiation force theory for compressible spherical particles. Calculating the primary acoustic radiation force that acts on spherical particles dispersed in a viscous medium also requires accounting for the medium viscosity [49]. Hence, Settnes and Bruus [43] included viscosity in the primary acoustic radiation

force theory for compressible spherical particles, and they demonstrated that the primary acoustic radiation force can deviate by orders of magnitude between the viscous and inviscid theories.

The ultrasound wave field in a fluid medium causes locally fluctuating pressure, velocity, and density. Thus, we describe the standing ultrasound wave in terms of the incident pressure p_{inc}, density ρ_{inc}, and velocity $\mathbf{v}_{inc}$ of the fluid medium. The ultrasound wave in a fluid includes the sum of a perturbation series of n order variations. However, we only consider the zeroth, first, and second order because research has shown that the effect of higher-order terms ($n > 2$) can be neglected [50]. Thus, the ultrasound wave in terms of pressure p, density ρ, and velocity $\mathbf{v}$ variations yields

$$p = p_0 + p_1 + p_2 , \tag{1.7}$$

$$\rho = \rho_0 + \rho_1 + \rho_2 , \tag{1.8}$$

and

$$\mathbf{v} = \mathbf{v}_0 + \mathbf{v}_1 + \mathbf{v}_2 , \tag{1.9}$$

where p_0, ρ_0, and $\mathbf{v}_0$ are the quiescent pressure, density, and velocity. The quiescent density $\rho_0 = \rho_m$ and the quiescent velocity $\mathbf{v}_0 = \mathbf{0}$. We substitute $p_1 = p_{inc}$ and $\rho_1 = \rho_{inc}$. Thus, the ultrasound wave yields

$$p = p_0 + p_{inc} + p_2 , \tag{1.10}$$

$$\rho = \rho_m + \rho_{inc} + \rho_2 , \tag{1.11}$$

and

$$\mathbf{v} = \mathbf{v}_1 + \mathbf{v}_2 . \tag{1.12}$$

We calculate the time-averaged primary acoustic radiation force $\mathbf{F}_{inc}$ that acts on a spherical particle as the time-averaged second order forces applied to a fixed control surface $\partial\Omega$ in the bulk

of the fluid medium that encompasses a spherical particle [39]. Hence, the time-averaged primary acoustic radiation force $\mathbf{F}_{inc}$ is the surface integral of the sum of the time-averaged second-order pressure $\langle p_2 \rangle$ and momentum flux tensor $\rho_m \langle \mathbf{v}_1 \mathbf{v}_1 \rangle$, which accounts for all momentum entering and leaving the control volume enclosed by $\partial\Omega$ as

$$\mathbf{F}_{inc} = -\int_{\partial\Omega} \left[\langle p_2 \rangle \mathbf{n} + \rho_m \langle (\mathbf{n} \cdot \mathbf{v}_1) \mathbf{v}_1 \rangle \right] da \,, \tag{1.13}$$

where $\mathbf{n}$ is a unit vector that points normal to $\partial\Omega$, and the angle bracket $\langle \bullet \rangle$ is an operator that indicates the time average of harmonic time-dependent functions. Euler's equations of fluid dynamics show that the second-order time-averaged pressure variations $\langle p_2 \rangle$ are a function of the first order variations, i.e., a function of the incident ultrasound wave field,

$$\langle p_2 \rangle = \frac{1}{2} k \langle p_{inc}^2 \rangle - \frac{1}{2} \rho_m \langle v_1^2 \rangle, \tag{1.14}$$

where $v_1^2 = (\nabla\varphi_{inc} + \nabla\varphi_{sc})^2$, and the time average of the product of two functions (for example, f and g) is

$$\langle fg \rangle = \frac{1}{2} \Re\{ fg^* \}, \tag{1.15}$$

where * represents the complex conjugate.

Applying Gauss's integral theorem for tensors further simplifies Eq. (1.13), and yields the primary acoustic radiation force $\mathbf{F}_{inc} = -\nabla U_{inc}$ that acts on a spherical particle of radius $a << \lambda$ in an inviscid medium. U_{inc} is the primary acoustic radiation potential, calculated in terms of the first-order incident ultrasound wave field variations p_{inc} and $\mathbf{v}_{inc}$ at the location of the particle as

$$U_{inc} = \frac{4\pi}{3} a^3 \left(f_1 \frac{\beta_m}{2} \langle p_{inc}{}^2 \rangle - f_2 \frac{3\rho_m}{4} \langle \mathbf{v}_{inc}{}^2 \rangle \right), \tag{1.16}$$

where f_1 and f_2 are the monopole and dipole scattering coefficients presented in Sec. 1.4.1.

In a standing ultrasound wave field, the primary acoustic radiation force drives particles to locations where the primary acoustic radiation potential U_{inc} is locally minimum, $||\mathbf{F}_{inc}|| = 0$, and points towards these locations in the surrounding region. The acoustic contrast factor

$$\phi = \frac{1}{3} f_1 + \frac{1}{2} f_2 \tag{1.17}$$

determines whether the local minima occur at the nodes ($\phi > 0$) or antinodes ($\phi < 0$) of the standing ultrasound wave field. Combinations of particles that are less compressible than the fluid medium in which they are dispersed result in $\phi > 0$, whereas particles that are more compressible than the fluid medium in which they are dispersed result in $\phi < 0$.

Figure 1.15 shows the normalized incident velocity potential φ_{inc} (dotted maroon line), primary acoustic radiation potential U_{inc} (solid orange line), and the magnitude of the primary acoustic radiation force $||\mathbf{F}_{inc}||$ (dashed gray line) of a 1D standing ultrasound wave. The solid black arrows indicate the direction of the primary acoustic radiation force that acts on particles in the standing ultrasound wave for $\phi > 0$ (Figure 1.15 (a)), which drives the particles to the nodes (solid black dots) and for $\phi < 0$ (Figure 1.15 (b)), which drives the particles to the antinodes (hollow black dots) of the standing ultrasound wave.

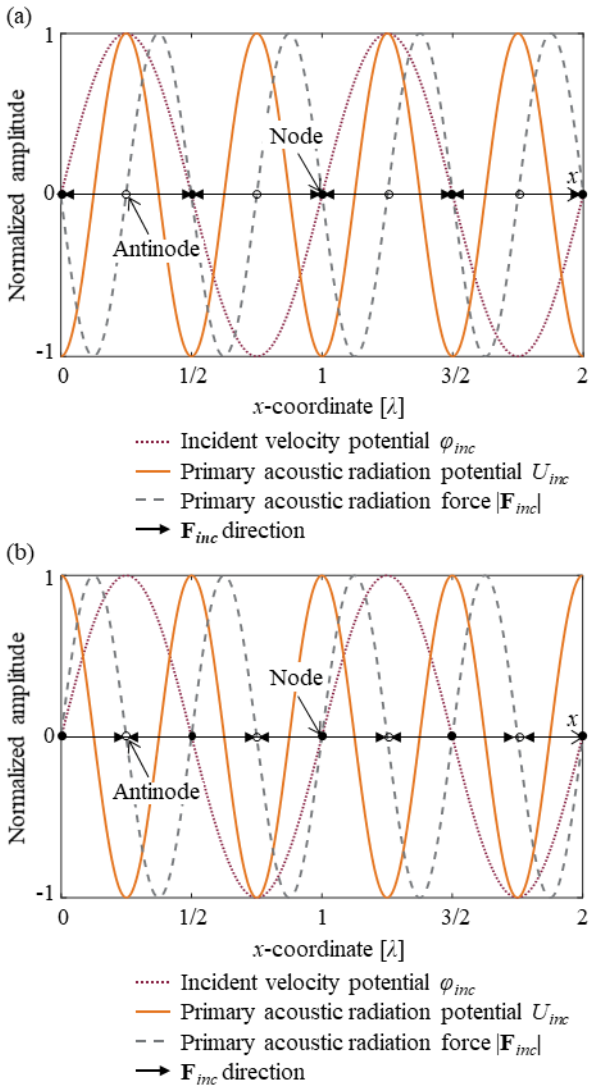

Figure 1.15: Normalized incident velocity potential φ_{inc} (dotted maroon line), primary acoustic radiation potential U (solid orange line), and primary acoustic radiation force $||\mathbf{F}_{inc}||$ (dashed gray line) of a 1D standing ultrasound wave, showing the direction of the primary acoustic radiation force acting on particles in the standing ultrasound wave (solid black arrows) for (a) $\phi > 0$, which drives the particles to the nodes (solid black dots) and for (b) $\phi < 0$, which drives the particles to the antinodes (hollow black dots) of the standing ultrasound wave.

Settnes and Bruus [43] expanded Gor'kov's primary acoustic radiation force theory to include the effect of medium viscosity in the calculation of the primary acoustic radiation force. They calculated the primary acoustic radiation force that a standing ultrasound wave exerts on a compressible, spherical particle in a viscous medium. They included the medium viscosity and

derived an analytical expression for the resulting primary acoustic radiation force. Hence, the primary acoustic radiation potential U_{inc} in the viscous medium is

$$U_{inc} = \frac{4\pi}{3} a^3 \left(f_1 \frac{\beta_m}{2} \left\langle p_{inc}{}^2 \right\rangle - f_2 \frac{3\rho_m}{4} \left\langle v_{inc}{}^2 \right\rangle \right). \tag{1.18}$$

with $f_1 = 1-\beta_p/\beta_m$ and $f_2 = \Re\{[2(1-\gamma)(\rho_p/\rho_m-1)]/[2\rho_p/\rho_m+1-3\gamma]\}$. Here, $\gamma = -3/2[1+i(1+\delta/a)]\delta/a$, with $\delta = (2\eta_m/\omega\rho_m)^{1/2}$ the viscous boundary layer thickness around a particle and η_m the medium viscosity [43].

1.4.3. Acoustic interaction force

The acoustic radiation force is the superposition of the primary acoustic radiation force $\mathbf{F}_{inc}$, which results from the incident standing ultrasound wave, and the acoustic interaction force $\mathbf{F}_{int}$, which originates from the acoustic interactions between neighboring particles [42]. In a mixture of particles and a fluid medium subject to a standing ultrasound wave, a secondary radiation force exists, which is commonly referred to as the acoustic interaction force $\mathbf{F}_{int}$. For a single particle in a mixture of particles and a fluid medium, the acoustic interaction force is caused by the ultrasound wave scattering from other particles in the mixture. Investigations of the acoustic interaction force date back to the 19th century, when Bjerknes studied the acoustic interaction force between a pair of bubbles [51], and Konig evaluated the acoustic interaction force between two rigid spheres [52]. Subsequently, others investigated the acoustic interaction force considering short-range interaction between rigid particles [53,54], bubbles [51,55], bubbles and rigid particles [56], and bubbles and droplets [57]. In addition, researchers studied the long-range interactions between rigid particles [58], bubbles [59,60], and droplets [61].

Furthermore, researchers have studied the acoustic interactions between spherical particles using single scattering, where the incident wave only scatters once [42,51,62–65], and multiple

scattering, where both the incident and scattered wave scatter multiple times when incident to a particle [61,66–69]. Figure 1.16 schematically illustrates a comparison between single and multiple scattering within a mixture of spherical particles and a fluid medium. In Fig. 1.16 (a), each spherical particle in the fluid medium scatters the incident velocity potential φ_{inc} and emits the scattered velocity potential φ_{sc} into the fluid medium. In contrast, in Fig. 1.16 (b), each spherical particle scatters both the incident velocity potential φ_{inc} and the scattered velocity potentials φ_{sc} from other particles into the fluid medium.

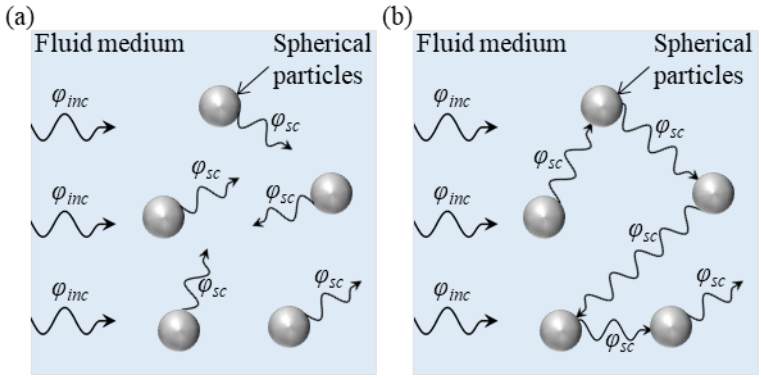

Figure 1.16: Schematic illustration of (a) single scattering and (b) multiple scattering within a mixture of spherical particles dispersed in a fluid medium, showing the incident velocity potential φ_{inc} and the scattered velocity potentials φ_{sc}.

Researchers have calculated the acoustic radiation force that accounts for both the primary acoustic radiation force $\mathbf{F}_{inc}$ and the acoustic interaction force $\mathbf{F}_{int}$ considering both single scattering [42,51,62–65] and multiple scattering. [61,66–69]. These works have demonstrated that single and multiple scattering between spherical particles in a plane (traveling and standing) ultrasound wave is dominated by single scattering, and can strengthen or weaken the acoustic radiation force depending on the size of the particles and their relative positions with respect to each other. For instance, Silva and Bruus [42] derived a theoretical expression for the acoustic interaction force between spherical particles dispersed in an inviscid medium and subject to a plane

(traveling and standing) ultrasound wave, accounting for single scattering only. They showed that the acoustic interaction force can be attractive or repulsive in the plane parallel to the wave propagation direction.

To account for single scattering with N spherical particles when calculating the acoustic radiation force $\mathbf{F}$, we calculate the velocity potential at the location of the ith particle $\mathbf{r}_i$ as a summation of the incident velocity potential at this location $\varphi_{inc}(\mathbf{r}_i)$ and all scattered velocity potentials from other particles, evaluated at the location of the ith particle [42], i.e.,

$$\varphi(\mathbf{r}_i) = \varphi_{inc}(\mathbf{r}_i) + \sum_{\substack{j=1 \\ j\neq i}}^{N} \varphi_{sc}(\mathbf{r}_i, \mathbf{r}_j) \,. \tag{1.19}$$

Using Eq. (1.16) and the definitions of ultrasound pressure $p(\mathbf{r}_j) = i\omega\rho_m\varphi(\mathbf{r}_j)$ and velocity $\mathbf{v}(\mathbf{r}_j) = \nabla\varphi(\mathbf{r}_j)$, we calculate the time-averaged acoustic radiation potential as [42]

$$U(\mathbf{r}_i) = \frac{4\pi}{3} a^3 \left(f_1 \frac{\beta_m}{2} \left\langle (i\rho_m \omega \varphi(\mathbf{r}_i))^2 \right\rangle - f_2 \frac{3\rho_m}{4} \left\langle \nabla\varphi(\mathbf{r}_i)^2 \right\rangle \right). \tag{1.20}$$

The acoustic radiation force $\mathbf{F} = -\nabla U(\mathbf{r}_i)$ is the sum of contributions from the incident velocity potential $\varphi_{inc}(\mathbf{r}_i)$, which we refer to as the primary acoustic radiation force $\mathbf{F}_{inc}(\mathbf{r}_i)$, and from the scattered velocity potentials $\varphi_{sc}(\mathbf{r}_i,\mathbf{r}_i)$, which we refer to as the acoustic interaction force $\mathbf{F}_{int}(\mathbf{r}_i)$ [42]. Thus,

$$\mathbf{F}(\mathbf{r}_i) = \mathbf{F}_{inc}(\mathbf{r}_i) + \mathbf{F}_{int}(\mathbf{r}_i) \,. \tag{1.21}$$

We determine the acoustic interaction force $\mathbf{F}_{int}(\mathbf{r}_i) = -\nabla U_{int}$ by substituting $\varphi(\mathbf{r}_i)$ from Eq. (1.19) in Eq. (1.20) and keeping only the terms that include $\varphi_{sc}(\mathbf{r}_i,\mathbf{r}_j)$ as [42]

$$U_{int}(\mathbf{r}_i) = \pi k^2 a^3 \rho_m \sum_{\substack{j=1 \\ j\neq i}}^{N} \left[\frac{2 f_1}{3} \left\langle \varphi_{inc}(\mathbf{r}_i) \varphi_{sc}(\mathbf{r}_i, \mathbf{r}_j) \right\rangle - f_2 \left\langle \nabla\varphi_{inc}(\mathbf{r}_i) \cdot \nabla\varphi_{sc}(\mathbf{r}_i, \mathbf{r}_j) \right\rangle \right]. \tag{1.22}$$

Here, we note that when only considering a pair of spherical particles in a standing ultrasound wave field, the acoustic interaction potentials U_{int} that these two particles experience are not necessarily equal due to the product of the incident and scattering velocity potentials in Eq. (1.22). Correspondingly, the acoustic interaction forces $\mathbf{F}_{int}$ on both particles are not necessarily the same [42].

1.5. State-of-the-art in ultrasound directed self-assembly

Ultrasound DSA offers the ability to organize and orient particles in specific patterns. Adjusting the parameters of the standing ultrasound wave field (frequency, amplitude, and phase) enables modifying the locations of nodes and antinode and, thus, designing where particles will assemble. However, to arrange specific patterns of particles using ultrasound DSA, one must derive the relationship between the ultrasound wave field parameters and the locations where the acoustic radiation potential is locally minimum, i.e., the locations where particles will assemble.

One can determine the relationship between the operating parameters of an array of ultrasound transducers and its resulting ultrasound wave field by solving either the "forward" or "inverse" ultrasound DSA problem. The forward problem calculates the pattern of particles that results from a specific set of ultrasound transducer operating parameters. Alternatively, the inverse problem determines the optimal operating parameters for each ultrasound transducer required to establish a standing ultrasound wave field where the local minima of the time-averaged acoustic radiation potential coincide with the locations of the specific pattern of particles one intends to assemble. Figure 1.17 schematically illustrates the forward and inverse ultrasound DSA problems.

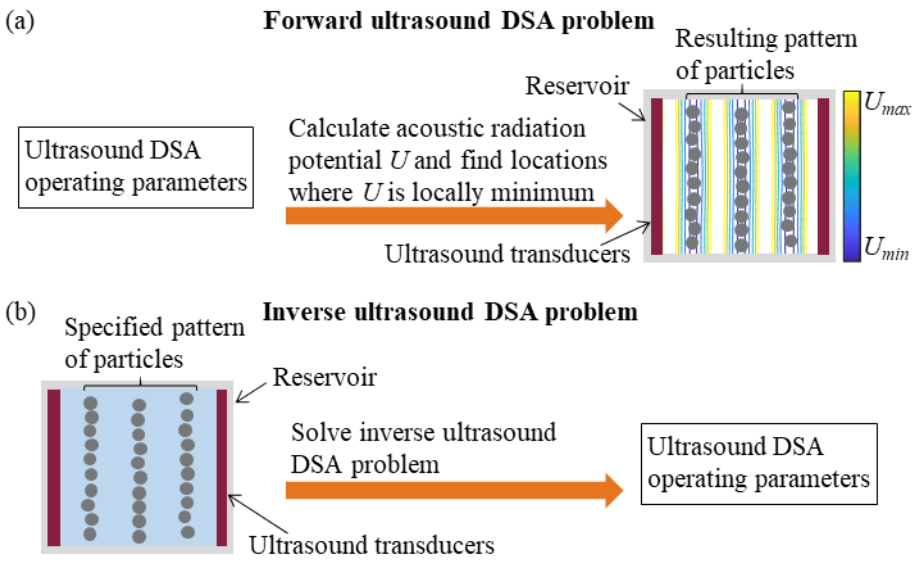

Figure 1.17: Schematic illustration of (a) the forward and (b) inverse ultrasound DSA problems.

The literature documents multiple solution methodologies to the forward ultrasound DSA problem [18,48,70]. However, solving the inverse ultrasound DSA problem is more relevant to manufacturing engineered materials than solving the forward ultrasound DSA problem, and is also more difficult to accomplish. It has been solved either directly or indirectly. Indirectly solving the inverse problem requires establishing a database of attainable patterns by solving the forward problem for a range of ultrasound transducer operating parameters [71–73]. In contrast, the direct solution method involves optimizing an objective function that minimizes the acoustic radiation potential at desired particle locations as a function of the ultrasound transducer operating parameters.

Specifically, multiple research groups have documented solutions to the inverse ultrasound DSA problem for ultrasound DSA of spherical particles in 1D [71], 2D [19,74,75], and 3D [76,77], and high aspect ratio particles in 2D [78], and 3D [79]. Figure 1.18 illustrates selected examples for the inverse ultrasound DSA problem in 1D, 2D, and 3D for spherical particles. We note that this list is illustrative, not exhaustive, i.e., other examples exist in the literature.

Greenhall et al. [71] developed a theoretical model to calculate the location of a particle as a function of the phases of two opposing ultrasound transducers. They showed that a spherical particle can be displaced in a 1D ultrasound wave across several wavelengths only by changing the phases of both ultrasound transducers in a choreographed fashion (Fig. 1.18 (a)). Greenhall et al. [19] also derived a theoretical model and demonstrated a practical solution to the inverse ultrasound DSA problem of spherical particles in 2D. The method is valid for reservoirs of any shape, lined with any number and arrangement of ultrasound transducers to create any specific pattern of spherical particles. They validated the accuracy of the numerical solutions derived from their theory through experiments, and illustrated the capability of their solution using numerical simulations of, e.g. a block "U" logo (red, specific pattern and black, simulated pattern) (Fig. 1.18 (b)). Furthermore, Prisbrey et al. [76] expanded the work of Greenhall et al. [19] to organize spherical particles dispersed in a fluid medium into 3D specific patterns. They performed experimental validation of simple 3D dot and line patterns (Fig. 1.18 (c)) and again illustrated the capability of their method by simulating highly complex patterns of particles (Fig. 1.18 (d)).

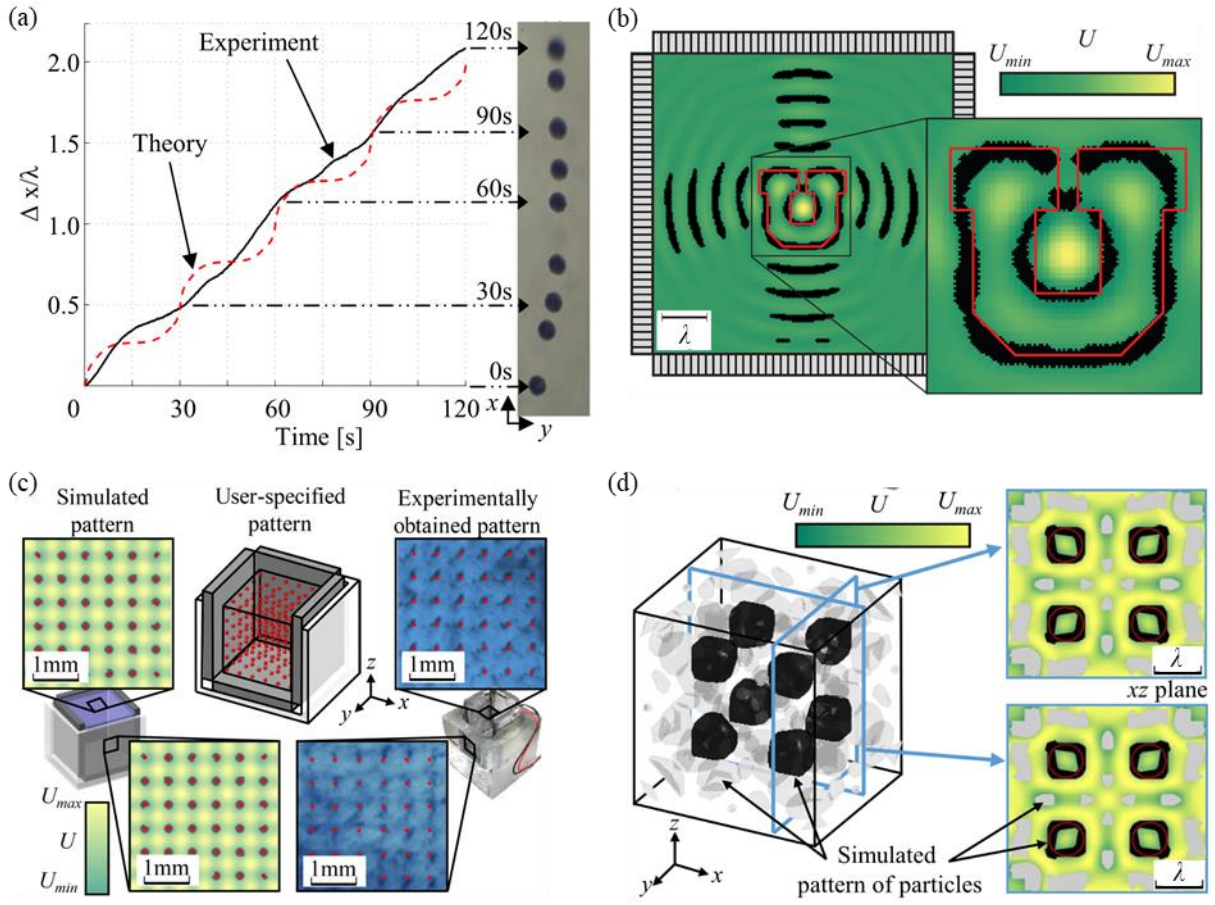

Figure 1.18: Selected examples for the inverse ultrasound DSA problem in 1D, 2D, and 3D for spherical particles. (a) displacement of a spherical particle in a 1D ultrasound wave across several wavelengths only by changing the phases of both ultrasound transducers in a choreographed fashion [71]. (b) A 2D block "U" pattern (red) and the simulated pattern of spherical particles (black) [19]. (c) Simulated and experimental dot patterns of particles implemented by solving the inverse 3D ultrasound DSA problem [76]. (d) A 3D simulated pattern of spherical particles consisting of eight hollow spheres [76]. Figures reprinted with permission.

Researchers have also used ultrasound DSA to organize and orient high aspect ratio particles. This is particularly useful when using ultrasound DSA to manufacture engineered polymer matrix composite materials with discontinuous fiber reinforcement. Figure 1.19 illustrates selected examples for the inverse ultrasound DSA problem in 2D and 3D for high aspect ratio particles. We note that this list is illustrative, not exhaustive; other examples exist in the literature.

Schwarz et al. [80] calculated the operating parameters of four ultrasound transducers arranged in a square formation to rotate high aspect ratio glass particles in a 2D (Fig. 1.19 (a)).

Similarly, Scholz et al. [81] demonstrated the rotation of high aspect ratio glass particles in 2D by sequentially activating a specific group of eight ultrasound transducers configured in an octagon. Prisbrey et al. [78] used ultrasound DSA to create 2D patterns of high aspect ratio particles with specific orientations. They theoretically derived a bead-chain model to determine the operating parameters of any arrangement of ultrasound transducers required to orient high aspect ratio particles in any user-specified orientation. Using their model, they experimentally organized and oriented high aspect ratio particles using ultrasound waves in 2D and documented a < 20% error between theory and experiments (Fig. 1.19 (b)). Marzo et al. [82] maximized the Laplacian of the acoustic radiation potential to drive the orientation of a single disc-shaped particle levitated in air.

Furthermore, Prisbrey et al. [79] theoretically derived and experimentally validated a method to determine the operating parameters (amplitude and phase) of any arrangement of ultrasound transducers that enables explicit control over the 3D organization and orientation of ellipsoidal particles in any 3D orientation (Fig. 1.19 (c)).

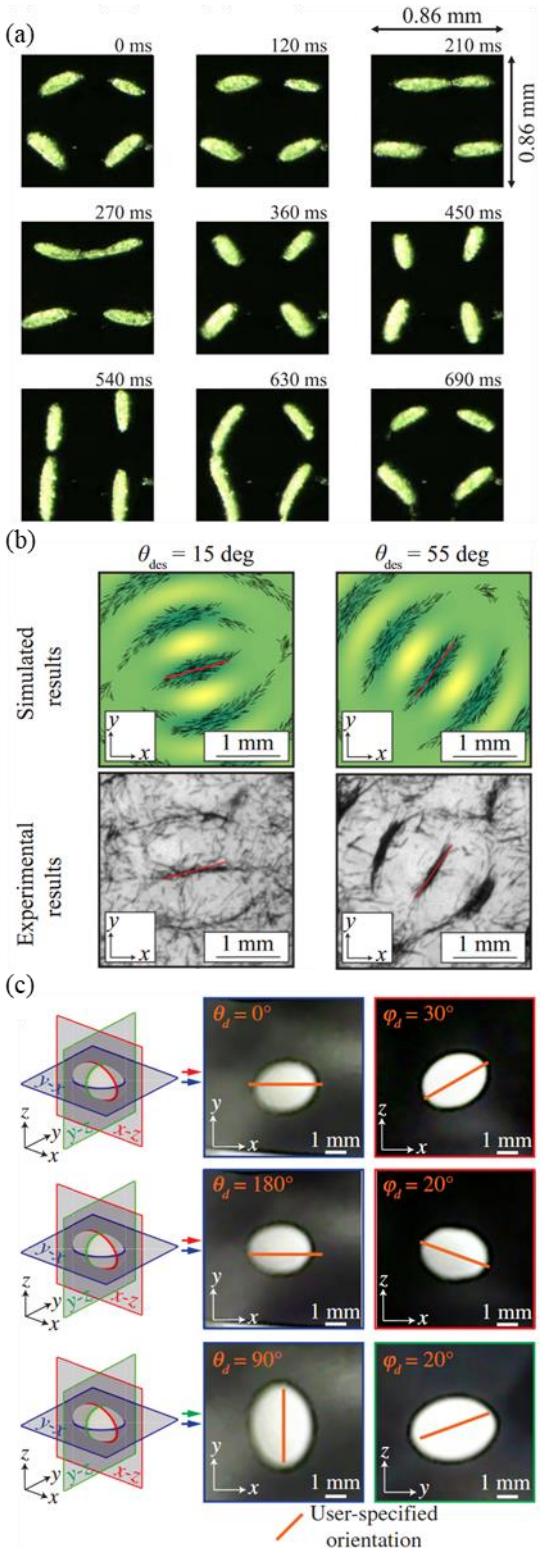

Figure 1.19: Selected examples for the inverse ultrasound DSA problem in 2D and 3D of high aspect ratio particles. (a) 180° rotation of glass high aspect ratio particles [80]. (b) Theoretical and experimental 2D specific orientations θ_{des} of carbon high aspect ratio particles [78], and (c) Theoretical and experimental 3D specific orientations θ_d and φ_d of an ellipsoidal particle [79]. Figures reprinted with permission.

Several groups have also studied the dynamic behavior of a single particle [83,84] and a group of particles [73,85,86] dispersed in a fluid medium and subject to an ultrasound wave. Figure 1.20 illustrates selected examples for the dynamic manipulation of a single particle and a group of particles. Greenhall et al. [83] examined the dynamic behavior of a single particle in a standing ultrasound wave. They determined that a particle can be displaced to a different location by adjusting the operating parameters of the ultrasound transducers in an underdamped, critically damped, or overdamped fashion. Marzo et al. [82] and Hoshi et al. [73] used ultrasound transducers to generate a focused acoustic beam, creating a local minimum of the acoustic radiation potential at a specific point in 3D space. They employed this technique to levitate and manipulate a single spherical particle in the air. Courtney et al. [85] calculated the ultrasound transducer phases needed to manipulate multiple polystyrene spherical particles in a circular reservoir in a 2D space (Fig. 1.20 (a)). Additionally, Prisbrey and Raeymaekers [86] used multiple phased arrays of ultrasound transducers to dynamically move a 3D pattern of particles along specific trajectories and numerically simulated this movement and observed good quantitative agreement (Fig. 1.20 (b)). They showed that an ultrasound power of seven times the ultrasound power required to levitate a particle is needed to successfully translate that particle over a single-step translation distance of one fourth of the wavelength.

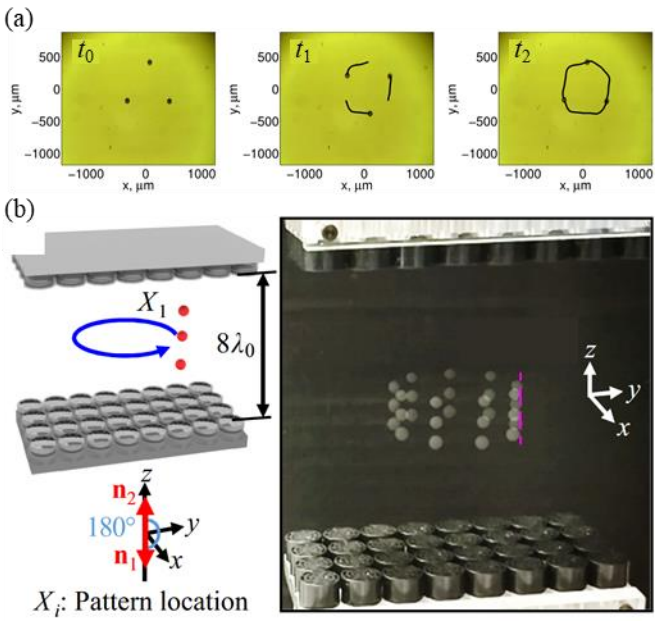

Figure 1.20: Selected examples for the dynamic manipulation of a single particle and a group of particles. (a) Manipulation of three polystyrene spherical particles in a 2D circular, showing three time-steps t_0, t_1, t_2 [85]. (b) Dynamic manipulation of a 3D pattern of particles along a circle trajectory [86]. Figures reprinted with permission.

1.6. Engineering applications of ultrasound directed self-assembly

Ultrasound DSA has been used in various engineering applications, including non-contact manipulation of particles and objects for precise handling or quality control [82,87,88], levitated displays [77,89,90], and organizing [91–93] and separating particles and cells, e.g. in lab-on-a-chip devices [94–96]. Figure 1.21 shows several examples of ultrasound DSA applications in separating particles in lab-on-a-chip devices (Fig. 1.21 (a)), precise handling (Fig. 1.21 (b)), and levitated displays (Fig. 1.21 (c)).

Ultrasound DSA is an efficient technique for quasi-instantaneously manipulating and organizing massive numbers of particles dispersed in a fluid medium. Hence, researchers have also used ultrasound DSA for particle filtration, e.g. to separate carbon particles from air in a smoke stack and to develop integrated microfluidic sensing devices based on particle aggregation [97,98]. In addition, researchers have used ultrasound DSA to separate particles in a continuous flow based

on their properties or size [96]. Figure 1.21 (a) schematically illustrates particle separation using ultrasound DSA; a fluid medium that contains dispersed particles of two different sizes flows through three different standing ultrasound wave fields in an ultrasound separation device. The acoustic radiation force drives particles to assemble in three different locations in the fluid flow.

Marzo et al. [82] showed that acoustic levitation can be employed to translate, rotate, and manipulate particles, e.g. with application in targeted drug delivery or acoustically controlled micro-machines. Figure 1.21 (b) illustrates a polystyrene particle that translates along a 3D trajectory and an ellipsoidal particle that rotates in 3D.

Furthermore, Hirayama et al. [89] presented a levitating volumetric display that simultaneously delivers visual, auditory, and tactile content using ultrasound DSA. Figure 1.21 (c) demonstrates the rendering of a 3D image with color information using their technique.

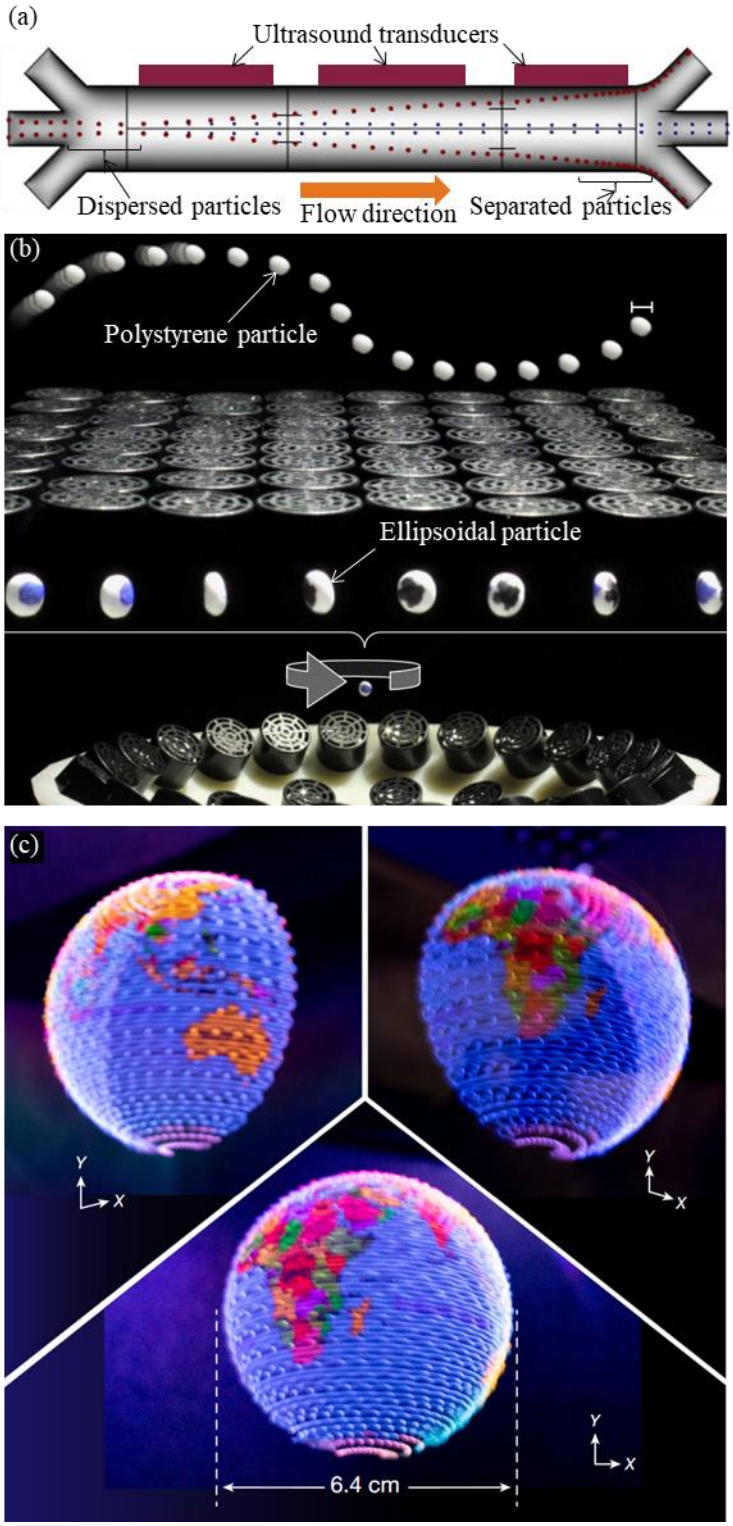

Figure 1.21: Examples of ultrasound DSA applications in (a) separating particles in lab-on-a-chip devices, (b) precise handling, and (c) levitated displays. (a) Schematic demonstration of particle separation using ultrasound DSA [96]. (b) A polystyrene particle accurately translating along a 3D path and an ellipsoidal particle controllably rotating in a 3D space [82]. (c) Rendering of a 3D image with color information using ultrasound DSA [89]. Figures reprinted with permission.

1.6.1. Manufacturing engineered polymer matrix composite materials

This dissertation research primarily focuses on the fundamental theory of ultrasound DSA in the context of manufacturing engineered polymer matrix composite materials.

Composite materials typically comprise a matrix and a filler material. The matrix provides the material geometry and fixes the filler material in place, whereas the filler material modifies the properties of the composite material. Engineered polymer matrix composite materials derive their properties from the properties of the filler (particles) and matrix materials, as well as the spatial organization and orientation of the filler in the matrix material [99]. Figure 1.22 shows examples of engineered polymer matrix composite materials that derive their properties from the spatial organization of the filler in the matrix. These examples include a 3D structure of an embedded electromagnetic coil pattern of conductive wires via aligning conductive copper nanoparticles in a photopolymer resin [100] (Fig. 1.22 (a)), multilayer structures with a network of silicone rubber and expanded graphite to enhance the thermal conductivity [101] (Fig. 1.22 (b)), and 3D printed composite material bolted joints with embedded continuous fibers to improve the stiffness and strength of the joint [102] (Fig. 1.22 (c)).

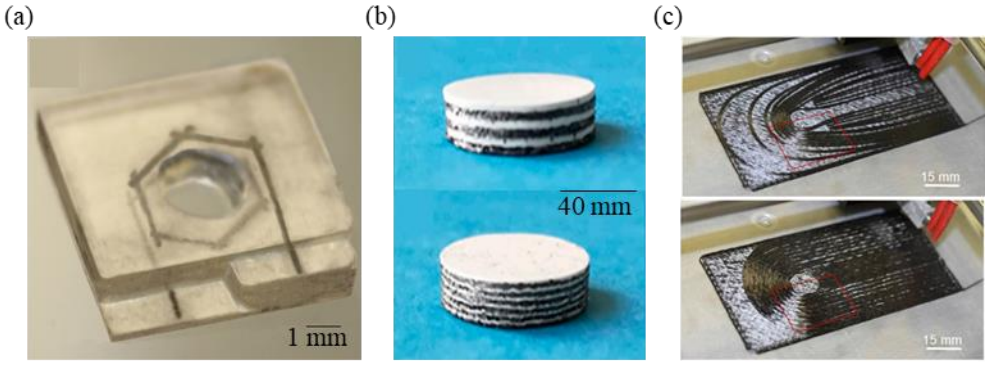

Figure 1.22: Examples of engineered polymer matrix composite materials that derive their properties from the spatial organization of the filler in the matrix. (a) A 3D structure with an embedded electromagnetic coil of conductive wires obtained via aligning conductive copper nanoparticles in a photopolymer resin [100]. (b) Multilayer structures with a network of silicone rubber and expanded graphite to enhance the thermal conductivity [101]. (c) 3D printed composite material bolted joints with embedded continuous fibers to improve the stiffness and strength of the joint [102]. Figures reprinted with permission.

Hence, from the examples of Fig. 1.22, it is clear that engineered polymer matrix composite materials can be designed to display tailored mechanical [103], electrical [104], thermal [105], acoustic [106], and electromagnetic properties [107], which often may not occur in nature. Therefore, they have attracted significant interest from the science and engineering community. However, to manufacture engineered materials with ultrasound DSA, it is necessary to integrate it with formative manufacturing techniques, such as mold casting and freeze casting, or additive manufacturing techniques, such as direct ink writing (DIW) and vat photopolymerization (VP). Then, the formative or additive manufacturing technique enables implementing the 3D geometry of the material or part, whereas ultrasound DSA enables control of the organization and orientation of the filler (particles) within the matrix material. Figure 1.23 schematically illustrates the integration of ultrasound DSA and mold casting, DIW, and VP.

Mold casting is a formative manufacturing technique that relies on a liquid polymer flowing into a 3D mold cavity before solidifying in its shape. The literature has documented that polymer matrix composite materials have been fabricated using mold casting in combination with ultrasound DSA to organize and align the filler material. Scholz et al. [108] used ultrasound DSA to align glass microfibers in several polymer resin materials in combination with mold casting. They reported that the glass fiber alignment increased the material specimen strength by 43% in the direction of the glass fiber alignment. In addition, Haslam et al. [109] used ultrasound DSA to align multi-walled carbon nanotubes (MWCNTs) in a polymer matrix to manufacture composite material specimens, and also reported a substantial increase of the material strength in the direction of MWCNT alignment. Greenhall et al. [110] also used ultrasound DSA in the gauge section of a dogbone-shaped acrylic mold to fabricate polymer matrix composite material specimens with aligned MWCNTs. Specifically, Greenhall et al. used ultrasound waves to concentrate MWCNTs

in one location, thereby obtaining a locally high weight percent of filler material (> 11%) to increase the mechanical properties of the composite material beyond what is possible with low weight percent of filler material (< 2%). Figure 1.23 (a) schematically illustrates the integration of ultrasound DSA and mold casting, whereas Fig. 1.23 (b) illustrates a dog bone specimen with aligned MWCNTs in the gauge section of the polymer matrix composite material.

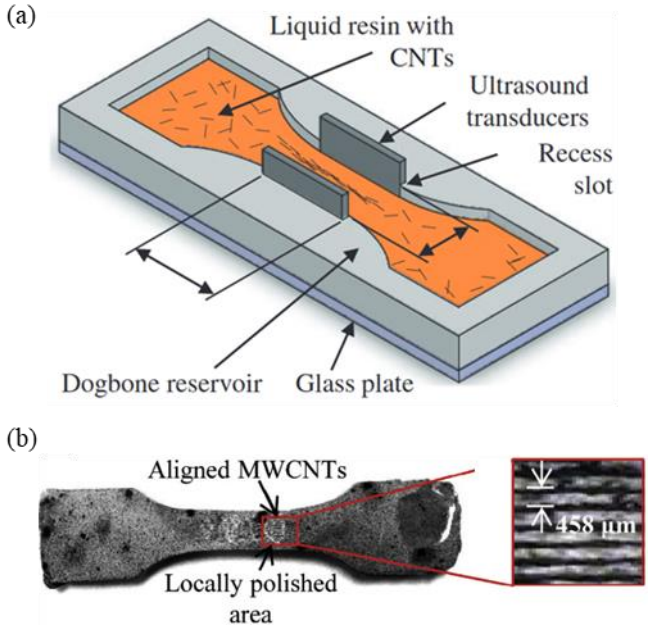

Figure 1.23: (a) Schematic illustration of the integration of ultrasound DSA and mold casting [110]. (b) A dogbone specimen of polymer matrix composite material with aligned MWCNTs [110]. Figures reprinted with permission.

DIW is an additive manufacturing process in which a liquid polymer matrix composite ink selectively extrudes, deposits, and cures to form a 3D material specimen [111]. Researchers have demonstrated the integration of DIW with ultrasound DSA to align filler material dispersed in the liquid ink. Friedrich et al. [112] used DIW in tandem with ultrasound DSA to print composite material specimens that comprise an epoxy matrix with aligned glass microspheres and studied the effect of ultrasound DSA operating parameters on the spatial distribution of the filler material. They determined that the ultrasound transducer voltage (amplitude of the ultrasound wave) has the strongest effect on the distribution of the filler material. Figure 1.24 (a) shows a schematic of their

setup, in which a piezoelectric ultrasound transducer establishes a standing ultrasound wave field across the extruder channel. Similarly, Collino et al. [113] used DIW with ultrasound DSA to fabricate epoxy filament with different filler materials. They demonstrated selectively organizing filler material along different lines according to their material properties. Figure 1.24 (b) shows randomly dispersed silicon carbide microfibers and hollow glass spheres arranged into distinct and separate lines of discontinuous filler material according to their density and compressibility, respectively, and located at the nodes or antinodes of a standing ultrasound wave field. Finally, Felt et al. used cylindrical ultrasound transducers in the nozzle of an experimental extrusion setup that mimics DIW or fused filament fabrication (FFF) and demonstrated that complex patterns of particles retain their shape in a continuous viscous flow, as long as the flow remains laminar [114]. Fig. 1.25 shows the schematic and photograph of their experimental setup that includes an acrylic reservoir with a mixture of viscous medium with randomly dispersed particles, which organize in a concentric circle pattern that flows through the cylindrical ultrasound transducer before extruding from the nozzle.

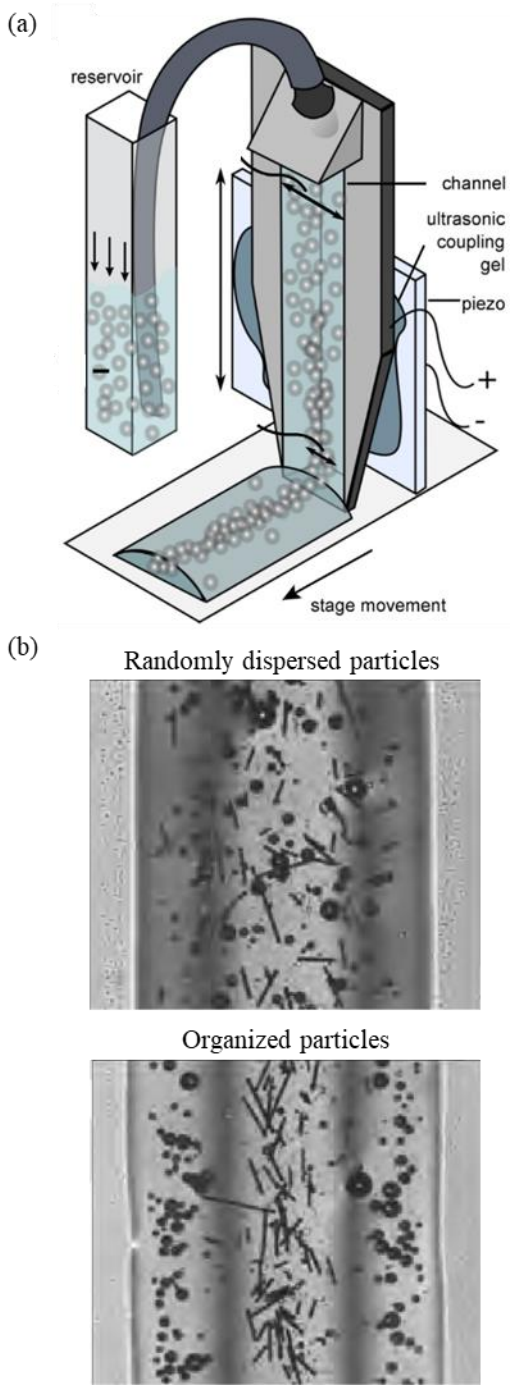

Figure 1.24: (a) Schematic of DIW with ultrasound DSA, in which a piezoelectric ultrasound transducer establishes a standing ultrasound wave field across the extruder channel to print composite material specimens that comprise an epoxy matrix with aligned glass microspheres [112]. (b) Randomly dispersed silicon carbide microfibers and hollow glass spheres arranged into distinct and separate lines of discontinuous filler material according to their density and compressibility, respectively, and located at the nodes or antinodes of a standing ultrasound wave field [113]. Figures reprinted with permission.

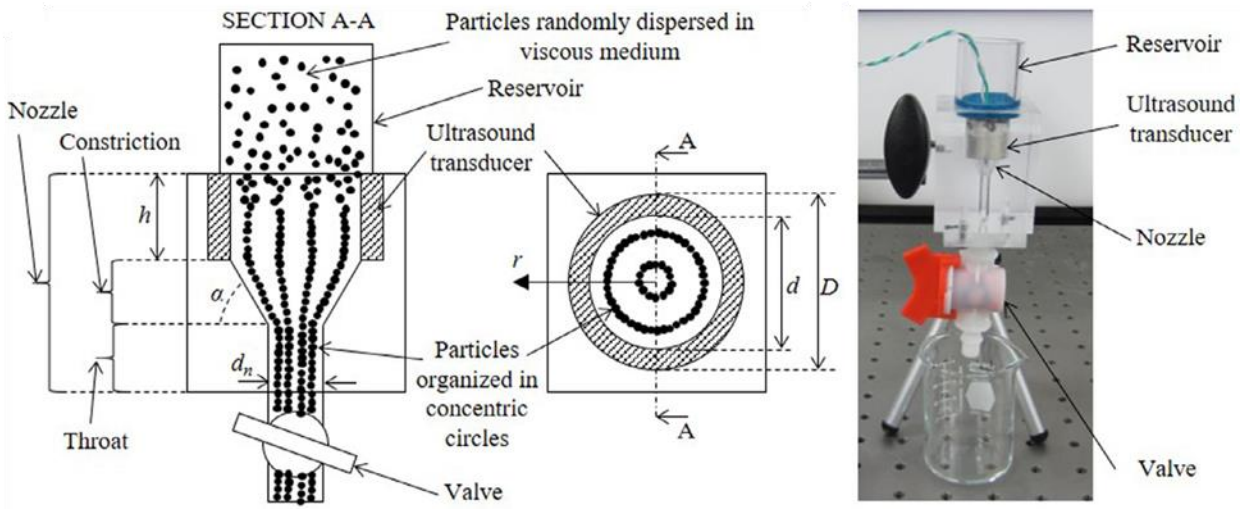

Figure 1.25: Schematic and photograph of the experimental setup with a cylindrical ultrasound transducer in the nozzle of an experimental extrusion setup that mimics DIW or FFF, showing an acrylic reservoir that contains a mixture of viscous medium with randomly dispersed particles, which organize in a concentric circle pattern when the mixture flows through the cylindrical ultrasound transducer, before extrusion from the nozzle [114]. Figure reprinted with permission.

VP is an additive manufacturing process that relies on a scanning laser source or a digital light processing (DLP) projector to selectively cure photopolymer resin layer-by-layer to manufacture a free-form geometry part or material specimen [115]. Figure 1.26 (a) illustrates a VP setup in combination with ultrasound DSA. Niendorf and Raeymaekers [14] combined VP and ultrasound DSA to 3D print polymer matrix composite materials with uniformly spaced parallel lines of aligned carbon microfibers. They characterized macroscale and microscale alignment of the microfiber as a function of ultrasound DSA operating parameters. Figure 1.26 illustrates the macroscale and microscale alignment of the microfiber in a polymer matrix composite material specimen with uniformly spaced parallel lines of aligned carbon microfibers. Melchert et al. [116] fabricated flexible polymer matrix composite materials with aligned carbon and silver-coated glass microfibers using a combination of VP and ultrasound DSA and demonstrated anisotropic electrical conductivity compared to specimens with randomly oriented microfibers. Figure 1.26 (c) illustrates the electrically conductive flexible polymer matrix composite material specimen.

Yunus et al. [100] also used VP with ultrasound DSA to align carbon nanofibers (CNFs), magnetite, and copper particles in photopolymer resin [20]. They reported that electrical conductivity depends on both the volume fraction of filler material and their alignment. Greenhall et al. [117] used ultrasound DSA combined with VP to manufacture multilayer polymer matrix composite materials with the specific alignment of nickel-coated carbon fibers in each layer; they manufactured haystack and Bouligand structures. Figure 1.26 (d) depicts the multilayer polymer matrix composite material specimen. They explained that the ultrasound DSA, combined with VP, enables fabricating engineered polymer matrix composite materials with both macroscale complex 3D geometries and user-specified microstructure.

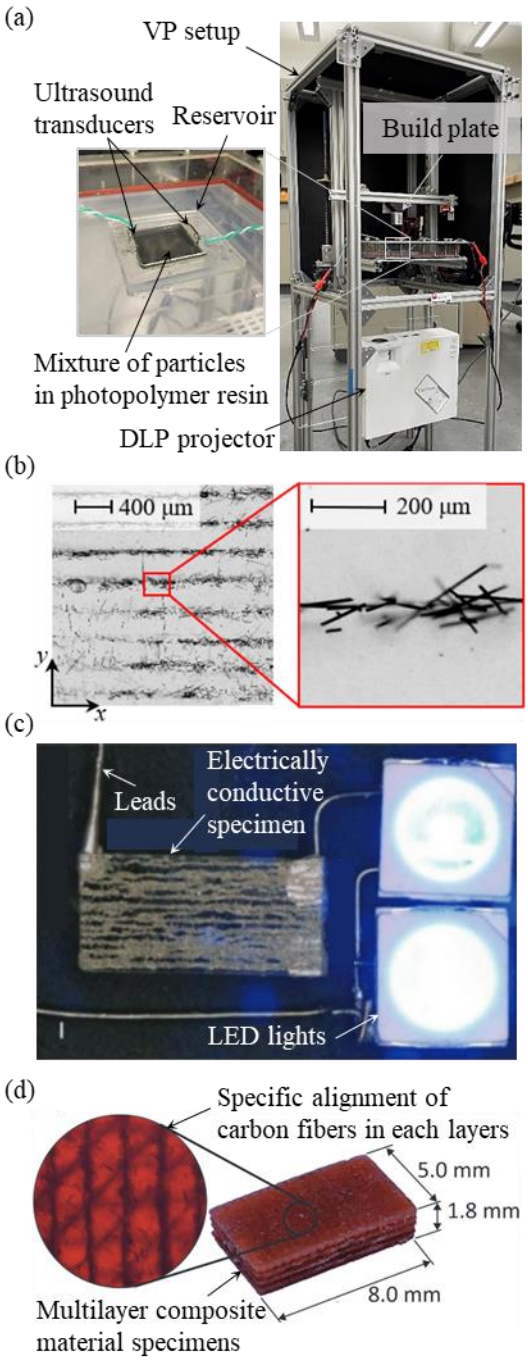

Figure 1.26: (a) VP setup in combination with ultrasound DSA. (b) Macroscale and microscale alignment of the microfiber in a polymer matrix composite material specimen with uniformly spaced parallel lines of aligned carbon microfibers [14]. (c) Electrically conductive flexible polymer matrix composite material specimen [116]. (d) Multilayer polymer matrix composite material specimen with specific alignment of nickel-coated carbon fibers in each layer [117]. Figures reprinted with permission.

1.7. Problem statement and research objective

From this succinct introduction, it is evident that medium viscosity plays a role in both propagation of the ultrasound wave and drag on the particles as they assemble into specific patterns, when integrating ultrasound DSA with VP. However, no theoretical models exist that allow simulating the ultrasound DSA process in a viscous medium either in steady-state or considering transient effects. Yet, knowledge of both viscous and transient effects is crucial to characterize the relationship between the ultrasound DSA process parameters and the locations where particles assemble, in the context of integrating ultrasound DSA with VP to 3D print engineered polymer matrix composite materials with tailored properties. Furthermore, quantifying the relationship between the ultrasound DSA process parameters and the local packing density of particles at the location where they assemble in a viscous medium is critical in terms of predicting the properties of the engineered materials.

Thus, the **research objective** of this dissertation research is twofold.

(1) Theoretically derive and experimentally validate a 2D model to determine the steady-state locations where spherical particles assemble during ultrasound DSA as a function of medium viscosity and particle volume fraction.

(2) Theoretically derive and experimentally validate a 3D model to quantify the steady-state and transient local packing density of spherical particles within the pattern features that result from ultrasound DSA.

To accomplish these research objectives, we attempt to solve the following three scientific problems:

Problem 1: Can we quantify and predict the locations where spherical particles assemble during ultrasound DSA in a viscous medium, considering the effects of medium viscosity and particle volume fraction?

Problem 2: Can we quantify and predict the steady-state and transient local particle packing density of spherical particles within the pattern features that result from ultrasound DSA? Additionally, can we characterize the effect of process parameters such as particle size, particle volume fraction, and medium viscosity on the local particle packing density?

Problem 3: Can we implement single and multiple scattering in the calculation of the acoustic radiation force for spherical particles in a viscous medium? Additionally, can we characterize and quantify their relative contributions to the calculation of the acoustic radiation force as a function of ultrasound DSA operating parameters and material properties?

1.8. Structure of the dissertation

This dissertation is organized as follows. In Chapter 2, we experimentally measure the deviation between locations where spherical particles assemble during ultrasound DSA as a function of medium viscosity and particle volume fraction. Additionally, we simulate the experiments using coupled-phase theory and the time-averaged acoustic radiation potential and derive best-fit equations that predict the deviation between locations where particles assemble during ultrasound DSA when considering viscous as opposed to inviscid theory. Chapter 2 addresses **Problem 1**.

In Chapter 3, we theoretically derive and experimentally validate a 3D model of the ultrasound DSA process to simulate and quantify the local packing density of spherical microparticles when assembled into pattern features. We study the packing density as a function

of ultrasound DSA process parameters, including particle volume fraction, particle size, and medium viscosity. Chapter 3 addresses the steady-state aspect of **Problem 2**.

In Chapter 4, we theoretically derive and experimentally validate a 3D model of the ultrasound DSA process and evaluate the local particle packing density at locations where particles assemble as a function of time, and as a function of ultrasound DSA process parameters. We study the transient packing density as a function of ultrasound DSA process parameters, including particle volume fraction, particle size, and medium viscosity. Chapter 4 addresses the transient aspect of **Problem 2**.

In Chapter 5, We quantify the relative contributions of single and multiple scattering in the calculation of the acoustic radiation force that acts on spherical particles dispersed in a viscous medium as a function of the ultrasound DSA process parameters, including particle size, material properties, and medium viscosity. First, we evaluate a theoretical case with three spherical particles in a viscous medium to study the effect of single and multiple scattering on the acoustic radiation force. Then, we study a realistic system with hundreds of particles dispersed in a viscous medium. Chapter 5 addresses **Problem 3**.

The research presented in this dissertation is relevant to using ultrasound DSA in engineering applications, specifically manufacturing of engineered materials with tailored properties such as polymer matrix composite materials.

1.9. References

[1] Thiruvengadathan, R., Korampally, V., Ghosh, A., Chanda, N., Gangopadhyay, K., and Gangopadhyay, S., 2013, "Nanomaterial Processing Using Self-Assembly-Bottom-up Chemical and Biological Approaches," Rep. Prog. Phys., **76**(6), p. 066501.

[2] Grzelczak, M., Vermant, J., Furst, E. M., and Liz-marza, L. M., 2010, "Directed Self-Assembly of Nanoparticles," **4**(7), pp. 3591–3605.

[3] Clark, T. D., Ferrigno, R., Tien, J., Paul, K. E., and Whitesides, G. M., 2002, "Template-Directed Self-Assembly of 10-Mm-Sized Hexagonal Plates," J. Am. Chem. Soc., **124**(19), pp. 5419–5426.

[4] Pan, Y., Gao, M., Huang, L., Liu, F., and Gao, H.-J., 2009, "Directed Self-Assembly of Monodispersed Platinum Nanoclusters on Graphene Moiré Template," Appl. Phys. Lett., **95**(9), p. 093106.

[5] Nie, Z., Petukhova, A., and Kumacheva, E., 2010, "Properties and Emerging Applications of Self-Assembled Structures Made from Inorganic Nanoparticles," Nat. Nanotechnol., **5**(1), pp. 15–25.

[6] Maury, P., Escalante, M., Reinhoudt, D. N., and Huskens, J., 2005, "Directed Assembly of Nanoparticles onto Polymer-Imprinted or Chemically Patterned Templates Fabricated by Nanoimprint Lithography," Adv. Mater., **17**(22), pp. 2718–2723.

[7] Dujardin, E., Peet, C., Stubbs, G., Culver, J. N., and Mann, S., 2003, "Organization of Metallic Nanoparticles Using Tobacco Mosaic Virus Templates," Nano Lett., **3**(3), pp. 413–417.

[8] Dujardin, E., Hsin, L.-B., Chris Wang, C. R., and Mann, S., 2001, "DNA-Driven Self-Assembly of Gold Nanorods," Chem. Commun., **0**(14), pp. 1264–1265.

[9] Fialkowski, M., Bishop, K. J. M., Klajn, R., Smoukov, S. K., Campbell, C. J., and Grzybowski, B. A., 2006, "Principles and Implementations of Dissipative (Dynamic) Self-Assembly," J. Phys. Chem. B, **110**(6), pp. 2482–2496.

[10] Chen, Y., Liu, H., Ye, T., Kim, J., and Mao, C., 2007, "DNA-Directed Assembly of Single-Wall Carbon Nanotubes," J. Am. Chem. Soc., **129**(28), pp. 8696–8697.

[11] Lewicki, J. P., Rodriguez, J. N., Zhu, C., Worsley, M. A., Wu, A. S., Kanarska, Y., Horn, J. D., Duoss, E. B., Ortega, J. M., Elmer, W., Hensleigh, R., Fellini, R. A., and King, M. J., 2017, "3D-Printing of Meso-Structurally Ordered Carbon Fiber/Polymer Composites with Unprecedented Orthotropic Physical Properties," Sci. Rep., **7**(1), p. 43401.

[12] Hermanson, K. D., Lumsdon, S. O., Williams, J. P., Kaler, E. W., and Velev, O. D., 2001, "Dielectrophoretic Assembly of Electrically Functional Microwires from Nanoparticle Suspensions," Science, **294**(5544), pp. 1082–1086.

[13] K. Smoukov, S., Gangwal, S., Marquez, M., and D. Velev, O., 2009, "Reconfigurable Responsive Structures Assembled from Magnetic Janus Particles," Soft Matter, **5**(6), pp. 1285–1292.

[14] Niendorf, K., and Raeymaekers, B., 2020, "Quantifying Macro- and Microscale Alignment of Carbon Microfibers in Polymer-Matrix Composite Materials Fabricated Using Ultrasound Directed Self-Assembly and 3D-Printing," Compos. Part Appl. Sci. Manuf., **129**, p. 105713.

[15] Kamat, P. V., Thomas, K. G., Barazzouk, S., Girishkumar, G., Vinodgopal, K., and Meisel, D., 2004, "Self-Assembled Linear Bundles of Single Wall Carbon Nanotubes and Their

Alignment and Deposition as a Film in a Dc Field," J. Am. Chem. Soc., **126**(34), pp. 10757–10762.
[16] Fujiwara, M., Oki, E., Hamada, M., Tanimoto, Y., Mukouda, I., and Shimomura, Y., 2001, "Magnetic Orientation and Magnetic Properties of a Single Carbon Nanotube," J. Phys. Chem. A, **105**(18), pp. 4383–4386.
[17] Kinsler, L. E., Frey, A. R., Coppens, A. B., and Sanders, J. V., 2000, *Fundamental of Acoustic*, John Wiley & Sons, Inc, New York.
[18] Chen, X., and Apfel, R. E., 1996, "Radiation Force on a Spherical Object in an Axisymmetric Wave Field and Its Application to the Calibration of High-frequency Transducers," J. Acoust. Soc. Am., **99**(2), pp. 713–724.
[19] Greenhall, J., Guevara Vasquez, F., and Raeymaekers, B., 2016, "Ultrasound Directed Self-Assembly of User-Specified Patterns of Nanoparticles Dispersed in a Fluid Medium," Appl. Phys. Lett., **108**(10), p. 103103.
[20] Noparast, S., Guevara Vasquez, F., and Raeymaekers, B., 2022, "The Effect of Medium Viscosity and Particle Volume Fraction on Ultrasound Directed Self-Assembly of Spherical Microparticles," J. Appl. Phys., **131**(13), p. 134901.
[21] Berg, R. E., and Stork, D. G., 2005, *The Physics of Sound*, Pearson Prentice-Hall, Upper Saddle River, N.J.
[22] Jha, A. K., 2013, *Textbook of Applied Physics*, I. K. International Pvt Ltd.
[23] Carvalho, C. C., Lopes dos Santos, J. M. B., and Marques, M. B., 2008, "A Time-of-Flight Method To Measure the Speed of Sound Using a Stereo Sound Card," Phys. Teach., **46**(7), pp. 428–431.
[24] Mattiat, O. E., ed., 1971, *Ultrasonic Transducer Materials*, Plenum Press, New York.
[25] "Sealed Waterproof Ultrasonic Sensor 25KHz Center Frequency Diameter 25mm" [Online]. Available: https://www.pzttransducer.com/sale-12680496-sealed-waterproof-ultrasonic-sensor-25khz-center-frequency-diameter-25mm.html. [Accessed: 27-Feb-2024].
[26] "Piezoelectric Disc, Diameter 27 Mm, Thin Thickness 0.22 Mm" [Online]. Available: https://www.auroraprosci.com/piezoelectric-disc--iameter-27-mm-thin-thickness-0.22-mm. [Accessed: 27-Feb-2024].
[27] "25mmx12mm PZT Ultrasonic Transducer , 112KHz Ultrasonic Piezoelectric Transducer" [Online]. Available: https://www.pzttransducer.com/sale-12679425-25mmx12mm-pzt-ultrasonic-transducer-112khz-ultrasonic-piezoelectric-transducer.html. [Accessed: 27-Feb-2024].
[28] "Buy Cheap TCT40-16T Ultrasonic Transducer Transmitter Probe 2pcs" [Online]. Available: https://www.uxcell.com/tct4016t-ultrasonic-transducer-transmitter-probe-2pcs-p-1652326.html. [Accessed: 27-Feb-2024].
[29] Rosencwaig, A., and Gersho, A., 1976, "Theory of the Photoacoustic Effect with Solids," J. Appl. Phys., **47**(1), pp. 64–69.
[30] Sherrit, S., and Mukherjee, B. K., 2007, "Characterization of Piezoelectric Materials for Transducers," ArXiv E-Prints.
[31] Cullity, B. D., and Graham, C. D., 2011, *Introduction to Magnetic Materials*, John Wiley & Sons.
[32] Lüscher, E., 2013, *Photoacoustic Effect Principles and Applications: Proceedings of the First International Conference on the Photoacoustic Effect in Germany*, Springer Science & Business Media.

[33] Uchino, K., 2017, *Advanced Piezoelectric Materials: Science and Technology*, Woodhead Publishing.
[34] Tressler, J. F., Alkoy, S., and Newnham, R. E., 1998, "Piezoelectric Sensors and Sensor Materials," J. Electroceramics, **2**(4), pp. 257–272.
[35] Gallego-Juarez, J. A., 1989, "Piezoelectric Ceramics and Ultrasonic Transducers," J. Phys. [E], **22**(10), p. 804.
[36] Ceramics, S. P., "Steminc Piezoelectric Ceramic Supplier" [Online]. Available: https://www.steminc.com/PZT/en/. [Accessed: 28-Feb-2024].
[37] L. V. King, 1934, "On the Acoustic Radiation Pressure on Spheres," Proc. R. Soc. Lond. Ser. - Math. Phys. Sci., **147**(861), pp. 212–240.
[38] Faran, J. J., 1951, "Sound Scattering by Solid Cylinders and Spheres," J. Acoust. Soc. Am., **23**(4), pp. 405–418.
[39] Karlsen, J. T., and Bruus, H., 2015, "Forces Acting on a Small Particle in an Acoustical Field in a Thermoviscous Fluid," Phys. Rev. E, **92**(4), p. 043010.
[40] Gurevich, B., Sadovnichaja, A. P., Lopatnikov, S. L., and Shapiro, S. A., 1998, "Scattering of a Compressional Wave in a Poroelastic Medium by an Ellipsoidal Inclusion," Geophys. J. Int., **133**(1), pp. 91–103.
[41] Fahy, F. J., 2000, *Foundations of Engineering Acoustics*, Elsevier.
[42] Silva, G. T., and Bruus, H., 2014, "Acoustic Interaction Forces between Small Particles in an Ideal Fluid," Phys. Rev. E, **90**(6), p. 063007.
[43] Settnes, M., and Bruus, H., 2012, "Forces Acting on a Small Particle in an Acoustical Field in a Viscous Fluid," Phys. Rev. E - Stat. Nonlinear Soft Matter Phys., **85**(1), pp. 1–12.
[44] "DLMF: §10.49 Explicit Formulas ‣ Spherical Bessel Functions ‣ Chapter 10 Bessel Functions" [Online]. Available: https://dlmf.nist.gov/10.49. [Accessed: 12-Dec-2022].
[45] Gor'kov, L. P., 1962, "On the Forces Acting on a Small Particle in an Acoustical Field in an Ideal Fluid," Sov. Phys. Dokl., **6**, p. 773.
[46] King, L. V., 1934, "On the Acoustic Radiation Pressure on Spheres," Proc. R. Soc. Lond. Ser. - Math. Phys. Sci., **147**(861), pp. 212–240.
[47] Yosioka, K., and Kawasima, Y., 1955, "Acoustic Radiation Pressure on a Compressible Sphere," Acta Acust. United Acust., **5**(3), pp. 167–173.
[48] Gorkov, L. P., 1962, "On the Force Acting on a Small Particle in an Acoustical Field in an Ideal Fluid," Sov PhysDokl, **6**, pp. 773–775.
[49] Doinikov, A. A., 1997, "Acoustic Radiation Force on a Spherical Particle in a Viscous Heat-Conducting Fluid. I. General Formula," J. Acoust. Soc. Am., **101**(2), pp. 713–721.
[50] Dyke, M. D. V., 1975, *Perturbation Methods in Fluid Mechanics*, Parabolic Pr, Stanford, Calif.
[51] Crum, L. A., 1975, "Bjerknes Forces on Bubbles in a Stationary Sound Field," J. Acoust. Soc. Am., **57**(6), pp. 1363–1370.
[52] König, W., 1891, "Hydrodynamisch-Akustische Untersuchungen," Ann. Phys., **278**(4), pp. 549–563.
[53] Embleton, T. F. W., 1962, "Mutual Interaction between Two Spheres in a Plane Sound Field," J. Acoust. Soc. Am., **34**(11), pp. 1714–1720.
[54] Nyborg, W. L., 1989, "Theoretical Criterion for Acoustic Aggregation," Ultrasound Med. Biol., **15**(2), pp. 93–99.
[55] Doinikov, A. A., and Zavtrak, S. T., 1995, "On the Mutual Interaction of Two Gas Bubbles in a Sound Field," Phys. Fluids, **7**(8), pp. 1923–1930.

[56] Doinikov, A. A., and Zavtrak, S. T., 1996, “Interaction Force between a Bubble and a Solid Particle in a Sound Field,” Ultrasonics, **34**(8), pp. 807–815.
[57] Doinikov, A. A., 1996, “Mutual Interaction between a Bubble and a Drop in a Sound Field,” J. Acoust. Soc. Am., **99**(6), pp. 3373–3379.
[58] Zhuk, A. P., 1985, “Hydrodynamic Interaction of Two Spherical Particles Due to Sound Waves Propagating Perpendicularly to the Center Line,” Sov. Appl. Mech., **21**(3), pp. 307–312.
[59] Doinikov, A. A., 1999, “Bjerknes Forces between Two Bubbles in a Viscous Fluid,” J. Acoust. Soc. Am., **106**(6), pp. 3305–3312.
[60] Doinikov, A. A., 2002, “Viscous Effects on the Interaction Force between Two Small Gas Bubbles in a Weak Acoustic Field,” J. Acoust. Soc. Am., **111**(4), pp. 1602–1609.
[61] Zheng, X., and Apfel, R. E., 1995, “Acoustic Interaction Forces between Two Fluid Spheres in an Acoustic Field,” J. Acoust. Soc. Am., **97**(4), pp. 2218–2226.
[62] Sepehrirahnama, S., Lim, K.-M., and Chau, F. S., 2015, “Numerical Study of Interparticle Radiation Force Acting on Rigid Spheres in a Standing Wave,” J. Acoust. Soc. Am., **137**(5), pp. 2614–2622.
[63] Baasch, T., Leibacher, I., and Dual, J., 2017, “Multibody Dynamics in Acoustophoresis,” J. Acoust. Soc. Am., **141**(3), pp. 1664–1674.
[64] Zhang, S., Qiu, C., Wang, M., Ke, M., and Liu, Z., 2016, “Acoustically Mediated Long-Range Interaction among Multiple Spherical Particles Exposed to a Plane Standing Wave,” New J. Phys., **18**(11), p. 113034.
[65] Sepehrirhnama, S., and Lim, K.-M., 2020, “Generalized Potential Theory for Close-Range Acoustic Interactions in the Rayleigh Limit,” Phys. Rev. E, **102**(4), p. 043307.
[66] Azarpeyvand, M., Alibakhshi, M., and Self, R., 2012, “Effects of Multi-Scattering on the Performance of a Single-Beam Acoustic Manipulation Device,” IEEE Trans. Ultrason. Ferroelectr. Freq. Control, **59**(8), pp. 1741–1749.
[67] Doinikov, A. A., 2001, “Acoustic Radiation Interparticle Forces in a Compressible Fluid,” J. Fluid Mech., **444**, pp. 1–21.
[68] Lopes, J. H., Azarpeyvand, M., and Silva, G. T., 2016, “Acoustic Interaction Forces and Torques Acting on Suspended Spheres in an Ideal Fluid,” IEEE Trans. Ultrason. Ferroelectr. Freq. Control, **63**(1), pp. 186–197.
[69] Sepehrirahnama, S., Chau, F. S., and Lim, K.-M., 2016, “Effects of Viscosity and Acoustic Streaming on the Interparticle Radiation Force between Rigid Spheres in a Standing Wave,” Phys. Rev. E, **93**(2), p. 023307.
[70] Barmatz, M., and Collas, P., 1985, “Acoustic Radiation Potential on a Sphere in Plane, Cylindrical, and Spherical Standing Wave Fields,” J. Acoust. Soc. Am., **77**(3), pp. 928–945.
[71] Greenhall, J., Guevara Vasquez, F., and Raeymaekers, B., 2013, “Continuous and Unconstrained Manipulation of Micro-Particles Using Phase-Control of Bulk Acoustic Waves,” Appl. Phys. Lett., **103**(7), p. 074103.
[72] Grinenko, A., Ong, C. K., Courtney, C. R. P., Wilcox, P. D., and Drinkwater, B. W., 2012, “Efficient Counter-Propagating Wave Acoustic Micro-Particle Manipulation,” Appl. Phys. Lett., **101**(23), p. 233501.
[73] Hoshi, T., Ochiai, Y., and Rekimoto, J., 2014, “Three-Dimensional Noncontact Manipulation by Opposite Ultrasonic Phased Arrays,” Jpn. J. Appl. Phys., **53**(7S), p. 07KE07.

[74] Courtney, C. R. P., Ong, C.-K., Drinkwater, B. W., Bernassau, A. L., Wilcox, P. D., and Cumming, D. R. S., 2011, "Manipulation of Particles in Two Dimensions Using Phase Controllable Ultrasonic Standing Waves," Proc. R. Soc. Math. Phys. Eng. Sci., **468**(2138), pp. 337–360.
[75] Courtney, C. R. P., Drinkwater, B. W., Demore, C. E. M., Cochran, S., Grinenko, A., and Wilcox, P. D., 2013, "Dexterous Manipulation of Microparticles Using Bessel-Function Acoustic Pressure Fields," Appl. Phys. Lett., **102**(12), p. 123508.
[76] Prisbrey, M., Greenhall, J., Guevara Vasquez, F., and Raeymaekers, B., 2017, "Ultrasound Directed Self-Assembly of Three-Dimensional User-Specified Patterns of Particles in a Fluid Medium," J. Appl. Phys., **121**(1), p. 014302.
[77] Ochiai, Y., Hoshi, T., and Rekimoto, J., 2014, "Pixie Dust: Graphics Generated by Levitated and Animated Objects in Computational Acoustic-Potential Field," ACM Trans. Graph., **33**(4), pp. 1–13.
[78] Prisbrey, M., and Raeymaekers, B., 2019, "Aligning High-Aspect-Ratio Particles in User-Specified Orientations with Ultrasound-Directed Self-Assembly," Phys. Rev. Appl., **12**(1), p. 014014.
[79] Prisbrey, M., Guevara Vasquez, F., and Raeymaekers, B., 2020, "Arranging Ellipsoidal Particles in Three-Dimensional User-Specified Orientations with Ultrasound-Directed Self-Assembly," Phys. Rev. Appl., **14**(2), p. 024026.
[80] Schwarz, T., Petit-Pierre, G., and Dual, J., 2013, "Rotation of Non-Spherical Micro-Particles by Amplitude Modulation of Superimposed Orthogonal Ultrasonic Modes," J. Acoust. Soc. Am., **133**(3), pp. 1260–1268.
[81] Scholz, M.-S., Drinkwater, B. W., Llewellyn-Jones, T. M., and Trask, R. S., 2015, "Counterpropagating Wave Acoustic Particle Manipulation Device for the Effective Manufacture of Composite Materials," IEEE Trans. Ultrason. Ferroelectr. Freq. Control, **62**(10), pp. 1845–1855.
[82] Marzo, A., Seah, S. A., Drinkwater, B. W., Sahoo, D. R., Long, B., and Subramanian, S., 2015, "Holographic Acoustic Elements for Manipulation of Levitated Objects," Nat. Commun., **6**(1), p. 8661.
[83] Greenhall, J., Guevara Vasquez, F., and Raeymaekers, B., 2014, "Dynamic Behavior of Microscale Particles Controlled by Standing Bulk Acoustic Waves," Appl. Phys. Lett., **105**(14), p. 144105.
[84] Grinenko, A., Wilcox, P. D., Courtney, C. R. P., and Drinkwater, B. W., 2012, "Proof of Principle Study of Ultrasonic Particle Manipulation by a Circular Array Device," Proc. R. Soc. Math. Phys. Eng. Sci., **468**(2147), pp. 3571–3586.
[85] Courtney, C. R. P., Demore, C. E. M., Wu, H., Grinenko, A., Wilcox, P. D., Cochran, S., and Drinkwater, B. W., 2014, "Independent Trapping and Manipulation of Microparticles Using Dexterous Acoustic Tweezers," Appl. Phys. Lett., **104**(15), p. 154103.
[86] Prisbrey, M., and Raeymaekers, B., 2018, "Ultrasound Noncontact Particle Manipulation of Three-Dimensional Dynamic User-Specified Patterns of Particles in Air," Phys. Rev. Appl., **10**(3), p. 034066.
[87] Mohanty, S., Khalil, I. S. M., and Misra, S., 2020, "Contactless Acoustic Micro/Nano Manipulation: A Paradigm for next Generation Applications in Life Sciences," Proc. R. Soc. Math. Phys. Eng. Sci., **476**(2243), p. 20200621.

[88] Guex, A. G., Di Marzio, N., Eglin, D., Alini, M., and Serra, T., 2021, "The Waves That Make the Pattern: A Review on Acoustic Manipulation in Biomedical Research," Mater. Today Bio, **10**, p. 100110.
[89] Hirayama, R., Martinez Plasencia, D., Masuda, N., and Subramanian, S., 2019, "A Volumetric Display for Visual, Tactile and Audio Presentation Using Acoustic Trapping," Nature, **575**(7782), pp. 320–323.
[90] Fushimi, T., Marzo, A., Drinkwater, B. W., and Hill, T. L., 2019, "Acoustophoretic Volumetric Displays Using a Fast-Moving Levitated Particle," Appl. Phys. Lett., **115**(6), p. 064101.
[91] Tian, L., Martin, N., Bassindale, P. G., Patil, A. J., Li, M., Barnes, A., Drinkwater, B. W., and Mann, S., 2016, "Spontaneous Assembly of Chemically Encoded Two-Dimensional Coacervate Droplet Arrays by Acoustic Wave Patterning," Nat. Commun., **7**(1), p. 13068.
[92] Wyatt Shields IV, C., Reyes, C. D., and López, G. P., 2015, "Microfluidic Cell Sorting: A Review of the Advances in the Separation of Cells from Debulking to Rare Cell Isolation," Lab. Chip, **15**(5), pp. 1230–1249.
[93] Kawasaki, S., Yeh, J.-J., Saccher, M., Li, J., and Dekker, R., 2022, "Bulk Acoustic Wave Based Mocrfluidic Particle Sorting with Capacitive Micromachined Ultrasonic Transducers," *2022 IEEE 35th International Conference on Micro Electro Mechanical Systems Conference (MEMS)*, IEEE, Tokyo, Japan, pp. 908–911.
[94] Juliano, P., Augustin, M. A., Xu, X.-Q., Mawson, R., and Knoerzer, K., 2017, "Advances in High Frequency Ultrasound Separation of Particulates from Biomass," Ultrason. Sonochem., **35**, pp. 577–590.
[95] Mettu, S., Yao, S., Sun, Q., Lawson, S. R., Scales, P. J., Martin, G. J. O., and Ashokkumar, M., 2020, "Effect of Bulk Viscosity and Emulsion Droplet Size on the Separation Efficiency of Model Mineral Oil-in-Water (O/W) Emulsions under Ultrasonic Standing Wave Fields: A Theoretical and Experimental Investigation," Ind. Eng. Chem. Res., **59**(16), pp. 7901–7912.
[96] Zhang, Y., and Chen, X., 2021, "Particle Separation in Microfluidics Using Different Modal Ultrasonic Standing Waves," Ultrason. Sonochem., **75**, p. 105603.
[97] Harris, N. R., Hill, M., Beeby, S., Shen, Y., White, N. M., Hawkes, J. J., and Coakley, W. T., 2003, "A Silicon Microfluidic Ultrasonic Separator," Sens. Actuators B Chem., **95**(1), pp. 425–434.
[98] Karpul, D., Tapson, J., Rapson, M., Jongens, A., and Cohen, G., 2010, "Limiting Factors in Acoustic Separation of Carbon Particles in Air," J. Acoust. Soc. Am., **127**(4), pp. 2153–2158.
[99] Thomas, S., Joseph, K., Malhotra, S. K., Goda, K., and Sreekala, M. S., 2012, *Polymer Composites, Macro- and Microcomposites*, John Wiley & Sons.
[100] Yunus, D. E., Sohrabi, S., He, R., Shi, W., and Liu, Y., 2017, "Acoustic Patterning for 3D Embedded Electrically Conductive Wire in Stereolithography," J. Micromechanics Microengineering, **27**(4), p. 045016.
[101] Xue, Y., Wang, H., Li, X., and Chen, Y., 2021, "Exceptionally Thermally Conductive and Electrical Insulating Multilaminar Aligned Silicone Rubber Flexible Composites with Highly Oriented and Dispersed Filler Network by Mechanical Shearing," Compos. Part Appl. Sci. Manuf., **144**, p. 106336.

[102] Sugiyama, K., Matsuzaki, R., Malakhov, A. V., Polilov, A. N., Ueda, M., Todoroki, A., and Hirano, Y., 2020, "3D Printing of Optimized Composites with Variable Fiber Volume Fraction and Stiffness Using Continuous Fiber," Compos. Sci. Technol., **186**, p. 107905.
[103] Nicolaou, Z. G., and Motter, A. E., 2012, "Mechanical Metamaterials with Negative Compressibility Transitions," Nat. Mater., **11**(7), pp. 608–613.
[104] Al-Saleh, M. H., and Sundararaj, U., 2009, "A Review of Vapor Grown Carbon Nanofiber/Polymer Conductive Composites," Carbon, **47**(1), pp. 2–22.
[105] Corbitt, S. J., Francoeur, M., and Raeymaekers, B., 2015, "Implementation of Optical Dielectric Metamaterials: A Review," J. Quant. Spectrosc. Radiat. Transf., **158**, pp. 3–16.
[106] Cummer, S. A., Christensen, J., and Alù, A., 2016, "Controlling Sound with Acoustic Metamaterials," Nat. Rev. Mater., **1**, p. 16001.
[107] Shalaev, V. M., 2007, "Optical Negative-Index Metamaterials," Nat. Photonics, **1**(1), pp. 41–48.
[108] Scholz, M. S., Drinkwater, B. W., and Trask, R. S., 2014, "Ultrasonic Assembly of Anisotropic Short Fibre Reinforced Composites," Ultrasonics, **54**(4), pp. 1015–1019.
[109] Haslam, M. D., and Raeymaekers, B., 2014, "Aligning Carbon Nanotubes Using Bulk Acoustic Waves to Reinforce Polymer Composites," Compos. Part B Eng., **60**, pp. 91–97.
[110] Greenhall, J., Homel, L., and Raeymaekers, B., 2019, "Ultrasound Directed Self-Assembly Processing of Nanocomposite Materials with Ultra-High Carbon Nanotube Weight Fraction," J. Compos. Mater., **53**(10), pp. 1329–1336.
[111] Gibson, I., Rosen, D., Stucker, B., and Khorasani, M., 2021, *Additive Manufacturing Technologies*, Springer, Cham, Switzerland.
[112] Friedrich, L., Collino, R., Ray, T., and Begley, M., 2017, "Acoustic Control of Microstructures during Direct Ink Writing of Two-Phase Materials," Sens. Actuators Phys., **268**, pp. 213–221.
[113] Collino, R. R., Ray, T. R., Fleming, R. C., Cornell, J. D., Compton, B. G., and Begley, M. R., 2016, "Deposition of Ordered Two-Phase Materials Using Microfluidic Print Nozzles with Acoustic Focusing," Extreme Mech. Lett., **8**, pp. 96–106.
[114] Felt, A., and Raeymaekers, B., 2023, "Ultrasound Directed Self-Assembly of Filler in Continuous Flow of a Viscous Medium through an Extruder Nozzle for Additive Manufacturing," Addit. Manuf. Lett., **5**, p. 100120.
[115] "3D Printing of Polymer Nanocomposites via Stereolithography - Manapat - 2017 - Macromolecular Materials and Engineering - Wiley Online Library" [Online]. Available: https://onlinelibrary.wiley.com/doi/full/10.1002/mame.201600553. [Accessed: 06-Mar-2024].
[116] Melchert, D. S., Collino, R. R., Ray, T. R., Dolinski, N. D., Friedrich, L., Begley, M. R., and Gianola, D. S., 2019, "Flexible Conductive Composites with Programmed Electrical Anisotropy Using Acoustophoresis," Adv. Mater. Technol., **4**(12), p. 1900586.
[117] Greenhall, J., and Raeymaekers, B., 2017, "3D Printing Macroscale Engineered Materials Using Ultrasound Directed Self-Assembly and Stereolithography," Adv. Mater. Technol., **2**(9), p. 1700122.

CHAPTER 2

THE EFFECT OF MEDIUM VISCOSITY AND PARTICLE VOLUME FRACTION ON ULTRASOUND DIRECTED SELF-ASSEMBLY OF SPHERICAL MICROPARTICLES

Adapted with permission from Noparast, S., Guevara Vasquez, F., and Raeymaekers, B., 2022, “The Effect of Medium Viscosity and Particle Volume Fraction on Ultrasound Directed Self-Assembly of Spherical Microparticles,” J. Appl. Phys., **131**(13), p. 134901.

2.1. Introduction

Using ultrasound DSA to fabricate composite materials requires the assembly of particles in a viscous rather than an inviscid medium, such as a thermoset resin or a (photo)polymer resin when integrating ultrasound DSA with, e.g. mold casting [1] and additive manufacturing [2], respectively. The locations where particles assemble, i.e., the nodes or antinodes of the standing ultrasound wave field, depend on the sound propagation velocity of the mixture of particles and viscous medium, which is a function of the frequency of the ultrasound wave, the compressibility and density of the medium and particles, the medium viscosity, and the particle volume fraction [3]. Thus, accurately assembling user-specified patterns of particles in a viscous medium requires accounting for medium viscosity and particle volume fraction rather than relying on inviscid theory only.

Several approaches exist to calculate these parameters. Phenomenological theory defines the sound propagation velocity based on an effective density and compressibility of the mixture [4,5]. However, this approach is only valid when particles are sufficiently far apart from each other so that interactions between them are negligible, which is not satisfied when, e.g. assembling patterns of closely-packed particles, and when the sound propagation velocity and density of the particles and medium are similar [6]. Alternatively, multiple-scattering theory predicts the sound propagation velocity based on scattering of an ultrasound wave in a mixture of particles and a viscous medium [7,8], but it only shows good agreement with experiments for dilute mixtures because it accounts for the acoustic interaction between particles but neglects hydrodynamic interactions that are important in concentrated mixtures [9]. Finally, coupled-phase theory provides an alternative to multiple-scattering theory and considers the hydrodynamic interaction between particles and medium resulting from viscous, inertial, and buoyancy forces [10]. It shows better

agreement with experiments than multiple-scattering theory, especially when the sound propagation velocity and density of the particles and medium are dissimilar [6].

Calculating the primary acoustic radiation force that acts on spherical particles dispersed in a viscous medium also requires accounting for the medium viscosity [11]. Settnes and Bruus [12] included viscosity in the primary acoustic radiation force theory for compressible particles, and demonstrated that the primary acoustic radiation force can deviate by orders of magnitude between the viscous and inviscid theory when a large density contrast exists between the particles and the medium, thus emphasizing the importance of accounting for medium viscosity and particle volume fraction when calculating the primary acoustic radiation force. However, they do not evaluate how the locations where particles assemble change with viscosity, which is critical to using ultrasound DSA as a fabrication method for engineered composite materials with user-specified patterns of particles embedded in the matrix material.

Thus, in Chapter 2, we experimentally measure the locations where particles assemble during ultrasound DSA as a function of medium viscosity and particle volume fraction. Second, we derive an ultrasound DSA theory that accounts for the effect of medium viscosity and particle volume fraction on the location where particles assemble. To solve this problem, we integrate the complex wavenumber from the coupled-phase theory into the Helmholtz equation and use the boundary element method to calculate the ultrasound incident velocity potential in a 2D solution domain, from which we derive the time-averaged primary acoustic radiation potential and primary acoustic radiation force. The particles assemble at the local minima of the time-averaged primary acoustic radiation potential, where the primary acoustic radiation force approaches zero. We determine the deviation between locations where particles assemble using viscous and inviscid

theory and compare experimental measurements to simulation results, and clarify the underlying physical phenomena.

2.2. Methods and materials

2.2.1. Experimental demonstration

Figure 2.1 shows a schematic of the experimental setup, which consists of an acrylic reservoir with two ultrasound transducers (piezoelectric ceramic plate, SM111, center frequency $f_{c,i}$, Steminc, FL, USA) affixed to two opposing reservoir walls. The reservoir is filled with a mixture of viscous oil (dimethyl silicone oils 350 cS and 1000 cS with dynamic viscosity $\eta_{m,1}$ = 0.34 Pa.s and $\eta_{m,2}$ = 0.97 Pa.s, GT Products, TX, USA) and borosilicate particles (GL0179B/-74 borosilicate glass spheres, average radius a = 20 µm, Mo-Sci Corporation, MO, USA). We energize both ultrasound transducers using a function generator (Tektronix AFG 3102) and a radio frequency (RF) power amplifier (E&I 2100L) with the same operating frequency f close to their center frequency $f_{c,i}$ to establish a standing ultrasound wave between both transducers that organizes the particles into a pattern of N = 20 parallel lines that coincide with the nodes of the standing ultrasound wave. To accomplish this, we use three different reservoirs with lengths L_1 = 17.33 mm, L_2 = 14.40 mm, L_3 = 10.23 mm, in tandem with ultrasound transducers with $f_{c,1}$ = 590 kHz, $f_{c,2}$ = 710 kHz, and $f_{c,3}$ = 1 MHz, respectively. The inset image of Fig. 2.1 shows a typical pattern of borosilicate particles (particle volume fraction Φ = 0.05) organized in parallel lines in dimethyl silicone oil 350 cS inside the reservoir with length L_1.

We experimentally determine the distance between adjacent lines where particles assemble d_{vis} as a function of the medium viscosity η_m and particle volume fraction Φ. However, instead of measuring d_{vis}, which is prone to error, we maintain $d_{vis} = L_i/(N+1)$ constant but measure the

operating frequency $f = f_{exp}$ required to establish a standing ultrasound wave that arranges the particles in $N = 20$ parallel lines within the reservoir, for each L_i and corresponding $f_{c,i}$. Specifically, $d_{vis,1} = 0.82$ mm for $L_1 = 17.33$ mm and $f_{c,1} = 590$ kHz, $d_{vis,2} = 0.68$ mm for $L_2 = 14.40$ mm and $f_{c,2} = 710$ kHz, and $d_{vis,3} = 0.49$ mm for $L_3 = 10.23$ mm and $f_{c,3} = 1$ MHz.

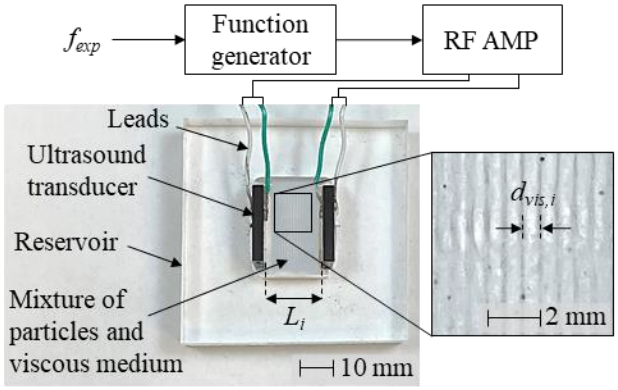

Figure 2.1: Schematic of the experimental setup, showing a typical experiment with dimethyl silicone oil 350 cS and borosilicate particles ($\Phi = 0.05$), with $L_2 = 14.40$ mm, $f_{c,2} = 710$ kHz, $N = 20$, and $d_{vis,2} = 0.68$ mm)

Table 2.1 shows the material properties of the viscous media and particles we have used in our experiments. Throughout this paper, the subscripts p and m refer to the particle and medium, respectively, when referring to the sound propagation velocity c, density ρ, dynamic viscosity η, and compressibility $\beta = 1/\rho c^2$. We measure the sound propagation velocity in both virgin viscous media c_m (i.e., without particles) using a pulse-echo time-of-flight experiment. We consider a constant sound propagation velocity c_m in each viscous medium, based on the center frequency $f_{c,i}$ of each ultrasound transducer, for all operating frequencies f, because they deviate only slightly from $f_{c,i}$.

Table 2.1: Material properties and experimental parameters.

Material	Sound propagation velocity, c [m/s]	Density, ρ [kg/m^3]	Dynamic viscosity, η_m [Pa.s]	Radius, a [µm]	Particle volume fraction, Φ
Dimethyl silicone oil, 350 cS	974	970	0.34	-	0 - 0.250
Dimethyl silicone oil, 1000 cS	983	970	0.97	-	0 - 0.125
Borosilicate glass spheres	5500	2600	-	20	-

We determine f_{exp} for each possible combination of parameters, i.e., a mixture of two viscous media and six different particle volume fractions for three different values of d_{vis} and corresponding L_i and $f_{c,i}$. Prior to each experiment, we disperse the specific particle volume fraction in the viscous medium with sonication (25 Watt, 2 minutes, UP200Ht, Hielscher, Teltow, Germany) to minimize particle agglomeration. We initiate each experiment with $f = f_{c,i}$, and we sequentially adjust f in 0.5 kHz intervals until we visually observe the best defined pattern of N = 20 parallel lines of particles, when $f = f_{exp}$. For each possible combination of parameters, we perform three repetitions and report the average and minimum and maximum values. We calculate the distance between adjacent lines where particles assemble in an inviscid medium as $d_{inv} = c_m/(2f_{exp})$ and quantify the deviation E_{exp} between adjacent lines where particles assemble in a viscous d_{vis} and an inviscid d_{inv} medium as $E_{exp} = |d_{vis}\text{-}d_{inv}|/d_{inv} = |2f_{exp}d_{vis}\text{-}c_m|/c_m$. Note that the factor of 2 in d_{inv} accounts for two parallel lines of particles per wavelength.

Furthermore, for each wavelength $\lambda = 2d_{vis}$ and particle volume fraction Φ, we experimentally determine the sound propagation velocity in the mixture of particles and viscous medium $c_{exp} = \lambda f_{exp}$.

2.2.2. Theoretical model

We derive a theoretical forward model of ultrasound DSA to predict the locations where particles with radius a (volume fraction Φ) assemble in a viscous medium. Figure 2.2 displays a schematic of a rectangular reservoir with a mixture of spherical particles and a viscous medium. We use the boundary element method (BEM) to simulate the ultrasound wave field within the reservoir and apply the primary acoustic radiation force theory for viscous media derived by Settnes and Bruus [12] to calculate the time-averaged primary acoustic radiation potential U_{inc}, from which we determine where particles assemble, i.e., at the local minima of U_{inc}.

Figure 2.2 shows a simple-closed boundary B with N_b boundary elements that enclose the solution domain D with N_d domain points. The width of the j^{th} boundary element with center point q_j is ε_j. A boundary element represents either a part of the reservoir wall (with velocity $v_j = 0$) or a part of an ultrasound transducer that acts as a piston source with velocity $v_j = v_0 e^{i\omega t - \theta}$ along its normal direction $\mathbf{n}_j$, with v_0 the velocity amplitude and ω and θ the operating frequency and phase. We maintain the acoustic impedance Z_b constant along the entire boundary B, whereas the acoustic impedance of the fluid medium is $Z_m = \rho_m c_m$.

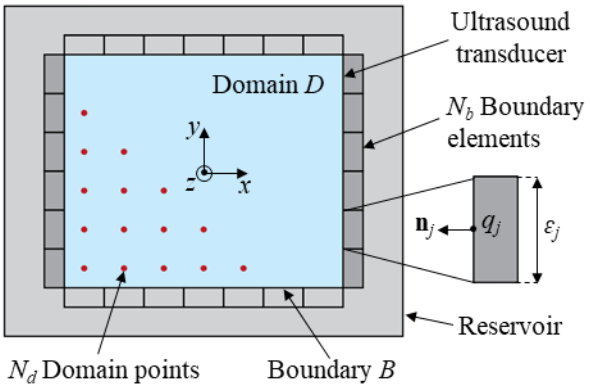

Figure 2.2: Rectangular reservoir with a mixture of particles and a viscous medium.

We neglect boundary effects confined to the immediate vicinity (~3λ) of the boundary *B* and, thus, only simulate the far-field [13]. The time-independent incident velocity potential φ_{inc} satisfies the Helmholtz equation throughout the solution domain *D*, i.e., $\nabla^2\varphi + \tilde{k}^2\varphi_{inc} = 0$. Here, k is the complex wavenumber that accounts for the effect of the medium viscosity η_m and particle volume fraction Φ on the sound propagation velocity (real part) and wave attenuation (imaginary part) of the mixture, given in the coupled-phase theory as [6]

$$k^2 = \omega^2\left[(1-\Phi)\beta_m + \Phi\beta_p\right] \times \frac{\rho_m\left[\rho_p(1-\Phi+\Phi S) + \rho_m S(1-\Phi)\right]}{\rho_p(1-\Phi)^2 + \rho_m\left[S+\Phi(1-\Phi)\right]}, \tag{2.1}$$

with $\omega = 2\pi f$, f is the operating frequency of the ultrasound wave field and $S = Q+iR$. $Q = 1/2[(1+2\Phi)/(1-\Phi)+9/4(\delta/a)$, $R = 9/4(\delta/a+\delta^2/a^2)$, $\delta = (2\eta_{eff}/\omega\rho_m)^{1/2}$ is the viscous boundary layer thickness around a particle, and $i = (-1)^{1/2}$. We calculate the effective viscosity of the mixture as $\eta_{eff} = (1+2.5\Phi+7.349\Phi^2)$ [6]. Additionally, the impedance boundary condition $\partial\varphi_{inc}/\partial n + ikZ\varphi_{inc} = 0$ exists along boundary *B*, with $Z = Z_m / Z_b$, which accounts for absorption and reflection of the ultrasound wave at the boundary *B*. We use the BEM based on Green's theorem to calculate the incident velocity potential φ_{inc} in all domain points [14].

The time-averaged primary acoustic radiation potential U_{inc} in a viscous medium is given as [12]

$$U_{inc} = \frac{4\pi}{3}a^3\left(f_1\frac{\beta_m}{2}\left\langle p_{inc}{}^2\right\rangle - f_2\frac{3\rho_m}{4}\left\langle v_{inc}{}^2\right\rangle\right), \tag{2.2}$$

where the ⟨•⟩ operator represents the time-average over one wave period, and the incident velocity and pressure fields in the solution domain *D* derive from the incident velocity potential φ_{inc} as $v_{inc} = -\nabla\varphi_{inc}$ and $p_{inc} = i\rho_m\omega\varphi_{inc}$ [12]. $f_1 = 1-\beta_p/\beta_m$ is the monopole scattering coefficient, and $f_2 = \Re\{[2(1-\gamma)(\rho_p/\rho_m-1)]/[2\rho_p/\rho_m+1-3\gamma]\}$ is the dipole scattering coefficient, with γ = -

$3/2[1+i(1+\delta/a)]\delta/a$. $\Re\{\bullet\}$ indicates the real part of the expression. The primary acoustic radiation force $\mathbf{F}_{inc} = -\nabla U_{inc}$ drives particles to locations where $||\mathbf{F}_{inc}|| = 0$ and $\mathbf{F}_{inc}$ points towards these locations in their immediate vicinity, which coincides with locations where U_{inc} is locally minimum.

We simulate a 2D solution domain D that replicates our experiments, including the dimensions of the reservoir L_i, medium viscosity η_m, and particle volume fraction Φ, and we also simulate the methodology of the experiments. For each parameter combination, we determine the operating frequency $f = f_{sim}$ that minimizes the average of the local minima of the time-averaged primary acoustic radiation potential U_{inc} in the $N = 20$ locations where particles assemble, by simulating U_{inc} for each $0.975f_{exp} \leq f \leq 1.025f_{exp}$, with 0.5 kHz intervals. Here, f_{exp} is the operating frequency for each experiment we performed (d_{vis}, η_m, Φ) that assembles the pattern of $N = 20$ parallel lines of particles. Hence, the simulations match the experimental methodology. Correspondingly, locations where particles assemble are identical in the simulations and experiments because we maintain $N = 20$ and, thus, the distance between adjacent local minima of U_{inc} is d_{vis}. We calculate the distance between adjacent local minima of U_{inc} in an inviscid medium as $d_{inv} = c_m/(2f_{sim})$. The simulated deviation of the distance between locations where particles assemble with viscous and inviscid ultrasound DSA theory is $E_{sim} = |d_{vis}\text{-}d_{inv}|/d_{inv} = |2f_{sim}d_{vis}\text{-}c_m|/c_m$.

Furthermore, for each wavelength $\lambda = 2d_{vis} = 2\pi / \Re\left\{\tilde{k}\right\}$ and particle volume fraction Φ, we solve Eq. (2.1) for ω and determine the sound propagation velocity in the mixture of particles and viscous medium $c_{th} = \lambda\omega/2\pi$.

2.3. Results and discussion

Figures 2.3(a) and 2.3(b) show the percent deviation of the distance between adjacent locations where particles assemble in a viscous and inviscid medium as a function of particle volume fraction Φ, and for different values of d_{vis} ($d_{vis,1}$ = 0.82 mm (black dot), $d_{vis,2}$ = 0.68 mm (blue square), $d_{vis,3}$ = 0.49 mm (red triangle), which correspond to different sizes of the reservoir L_i and ultrasound transducers with different $f_{c,i}$. We show both experimental results E_{exp} (solid markers) and simulation results E_{sim} (hollow markers) for medium viscosity η_m = 0.34 Pa.s in Fig. 2.3(a) and η_m = 0.94 Pa.s in Fig. 2.3(b). The solid markers show the arithmetic mean of three E_{exp} measurements and the error bars show the minimum and maximum values, whereas the hollow markers show a single simulation. In Fig. 2.3(b), we limit the particle volume fraction $\Phi \leq 0.125$ for the experimental results (solid markers) for practical reasons; medium viscosity η_m = 0.94 Pa.s in combination with $\Phi > 0.125$ causes high viscosity and attenuation of the ultrasound waves that prevent reliable assembly of particles in parallel lines. We derive 3rd order polynomial best-fit equations of the E_{sim} data points, which predict the deviation between locations where particles assemble when using viscous versus inviscid theory for ultrasound DSA. Conversely, it also allows an ultrasound DSA-user to determine whether to use viscous or inviscid theory to predict the locations where particles will assemble, based on the deviation for specific operating parameters (d_{vis}, η_m, Φ) and the required accuracy.

Additionally, Figs. 2.3(c) and 3(d) show the sound propagation velocity c in a mixture of spherical particles and viscous medium as a function of the particle volume fraction Φ, for different values of d_{vis} and for medium viscosity η_m = 0.34 Pa.s in Fig. 2.3(c) and η_m = 0.94 Pa.s in Fig. 2.3(d). We show experimental results c_{exp} with different markers and the theoretical solution c_{th} from Eq. (2.1) with different line types.

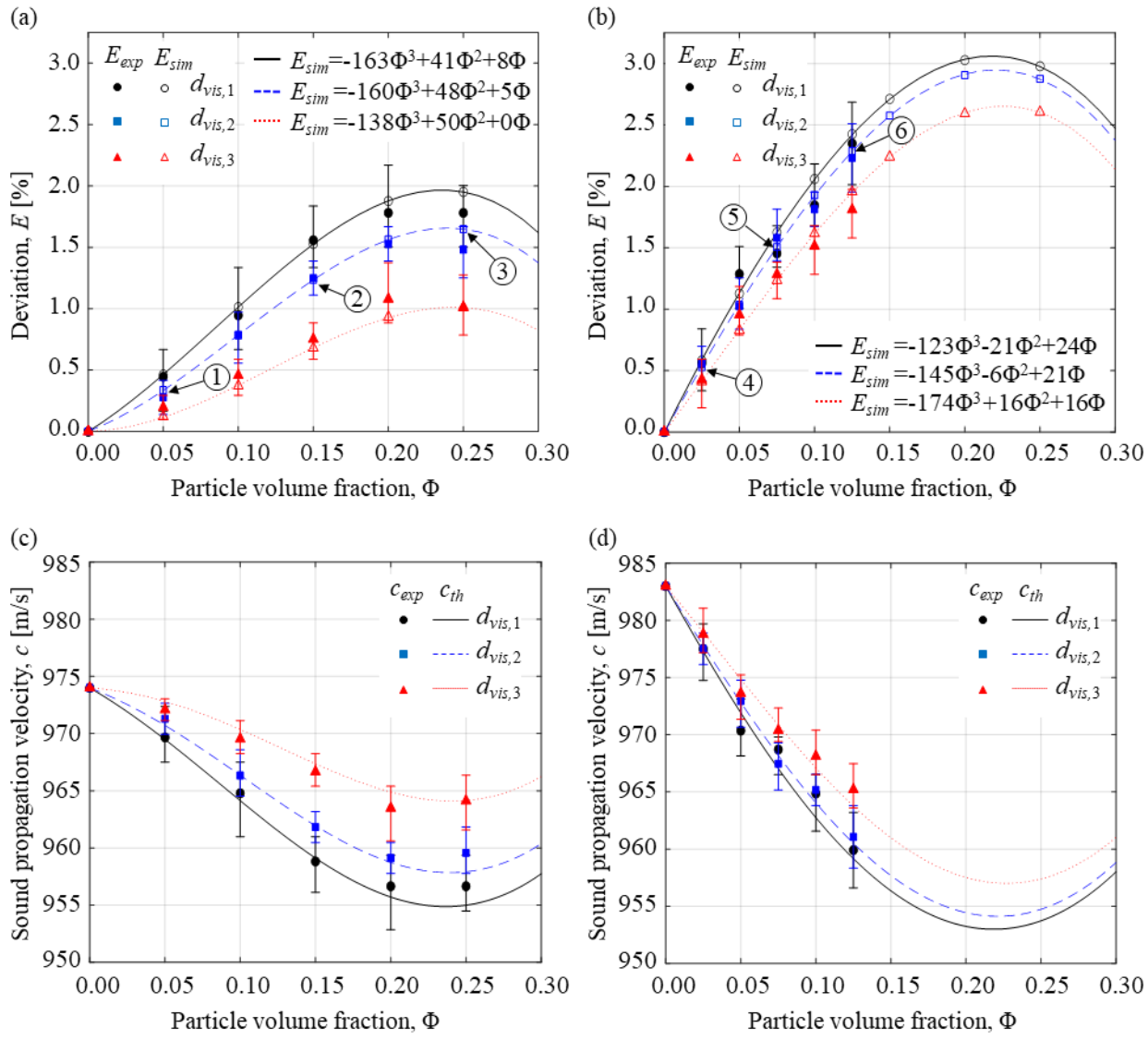

Figure 2.3: Percent deviation E_{exp} (solid markers) and E_{sim} (hollow markers) of the distance between adjacent locations where particles assemble in a viscous and inviscid medium as a function of particle volume fraction Φ, for $d_{vis,1}$ = 0.82 mm (black dot), $d_{vis,2}$ = 0.68 mm (blue square), $d_{vis,3}$ = 0.49 mm (red triangle), and for medium viscosity (a) η_m = 0.34 Pa.s and (b) η_m = 0.94 Pa.s. The lines represent best-fit equations of the simulated data (hollow markers). The sound propagation velocity in the mixture of viscous medium and spherical particles based on experiments c_{exp} (markers) and theory c_{th} (lines) as a function of particle volume fraction Φ, for $d_{vis,1}$ (black dot/solid line), $d_{vis,2}$ (blue square/dashed line), $d_{vis,3}$ (red triangle/dotted line), and for medium viscosity (c) η_m = 0.34 Pa.s and (d) η_m = 0.94 Pa.s.

From Fig. 2.3, we observe that E first increases and then decreases with increasing particle volume fraction Φ, independent of η_m and d_{vis}, which results from competing mechanisms. First, the effective viscosity η_{eff} of the mixture increases with increasing Φ, which increases the viscous

layer thickness δ around each particle and, thus, increases the drag force it experiences when moving in the viscous medium during ultrasound DSA [6]. Increasing Φ also increases the number of particles in a specific control volume within the mixture. Together, these two phenomena decrease the rate of momentum transfer in the mixture [6], which decreases the sound propagation velocity of the mixture $c \leq c_m$ and, thus, increases $E = |d_{vis}\text{-}d_{inv}|/d_{inv} = |2fd_{vis}\text{-}c_m|/c_m = |c\text{-}c_m|/c_m$, considering that the distance between adjacent lines of particles $d_{vis} = c/(2f)$. E and f may either have the *exp* or *sim* subscript as it is valid for both the experimental and simulation results. On the other hand, the density and compressibility of the mixture increases and decreases, respectively, with increasing Φ [6], which increase the sound propagation velocity of the mixture $c \leq c_m$ and, thus, decrease E. We verify that the particle volume fraction Φ for which E is maximum (see Figs. 2.3(a) and 3(b)) corresponds to Φ for which the sound propagation velocity of the mixture is minimum (see Figs. 2.3(c) and 3(d)), independent of $d_{vis,i}$ and η_m.

Furthermore, we observe from Fig. 2.3 that E increases with increasing d_{vis} and, correspondingly, decreasing operating frequency f. The viscous layer thickness $\delta = (2\eta_{eff}/\omega\rho_m)^{1/2}$ around a particle increases with decreasing operating frequency $f = \omega/2\pi$, which increases the drag force on a particle driven through the mixture by the primary acoustic radiation force and, in turn, decreases the rate of momentum transfer in the mixture, which decreases the sound propagation velocity $c \leq c_m$ and increases E.

Comparing Figs. 2.3(a) and 3(b), we observe that E_{sim} increases with increasing η_m (and η_{eff}), which increases the viscous layer thickness δ around a particle and, thus increases the drag force on particles. Consequently, it decreases the rate of momentum transfer in the mixture, which decreases the sound propagation velocity c and increases E.

We note that the percent deviation between adjacent locations where particles assemble using viscous and inviscid theory is small (< 3%). However, it multiplies over the entire scale of the experiment and, thus, increases in importance when using ultrasound DSA to manufacture macroscale material specimens. Furthermore, we note that we calculate the percent deviation between locations where particles assemble using viscous and inviscid theory, but we use the viscosity of the dimethyl silicon oil in the inviscid theory. However, when determining the deviation between adjacent locations where particles assemble with viscous theory for a viscous medium and inviscid theory using an inviscid medium such as water at STP (η = 0.001 Pa.s), we observe the same trends as those depicted in Fig. 2.3, but the maximum deviation reaches 35%. Evidently, using inviscid theory with an inviscid medium is not a good predictor for locations where particles assemble in a viscous medium because the sound propagation velocity in water (c_m = 1490 m/s) is substantially higher than that in the viscous medium (see Table. I), which affects the wavelength of the standing ultrasound wave and, thus, the locations of its nodes.

Finally, we mark six numbered labels in Figs. 2.3(a) and 2.3(b) to illustrate both the experimental and simulation results of selected individual data points. Figure 2.4(a) illustrates the experimental results for each numbered label (solid markers in Fig. 2.3), showing lines of aligned particles (dark) in viscous medium (bright), whereas Fig. 2.4(b) shows the corresponding simulation results (hollow markers in Fig. 2.3) of the time-averaged primary acoustic radiation potential *U*, with blue contour lines indicating local minima. Figure 2.3 shows good quantitative agreement between E_{exp} and E_{sim}, which the images of individual data points in Fig. 2.4 illustrate. For each numbered label, we observe good agreement between the simulated primary acoustic radiation potential and the corresponding experimental results that show where particles assemble, including details of the standing ultrasound wave field, which is remarkable. Quantitatively, we

determine a maximum difference between experiments E_{exp} and simulations E_{sim} of 0.21 (for $d_{vis,1}$ = 0.82 mm, η_m = 0.97 Pa.s, Φ = 0.10).

Differences in the experimental and simulation results are likely due to imperfections in fabricating the experimental setup, including the imperfect rectangular shape of the reservoir and the alignment of the ultrasound transducers. Furthermore, the spherical particles are denser than the viscous medium in our experiment, which causes them to sink while subject to the ultrasound wave field. This may create a non-uniform spatial distribution of the particles orthogonal to the wave propagation direction (*z*-direction in Fig. 2.2) and increases the particle volume fraction at the bottom of the reservoir, thus affecting the sound propagation velocity. We also use a constant average particle radius a = 20 μm in our simulations. However, 90% of the particles have radius $a \leq 37$ μm and 50% of particles have radius 18 μm $\leq a \leq$ 22 μm. Hence, this may affect the sound propagation velocity of the mixture c. Finally, imperfect dispersion of particles in the viscous medium prior to the start of each experiment may also cause inaccuracy. Increasing particle volume fraction increases particle agglomeration, thus changing the effective particle size, and it also increases ultrasound attenuation, which decreases the primary acoustic radiation force that acts on the particles in the mixture. Each of these effects potentially distorts and fades the pattern of particles.

We also emphasize that the viscous DSA theory we have implemented in our simulations determines the locations where particles assemble in a viscous medium, accounting for both medium viscosity η_m and particle volume fraction Φ, which are different than where they assemble in an inviscid medium. This builds on Settnes and Bruus's [12] theory, which describes the primary acoustic radiation force that acts on spherical particles in a viscous medium as a function of medium viscosity, but did not determine or discuss the locations where particles assemble.

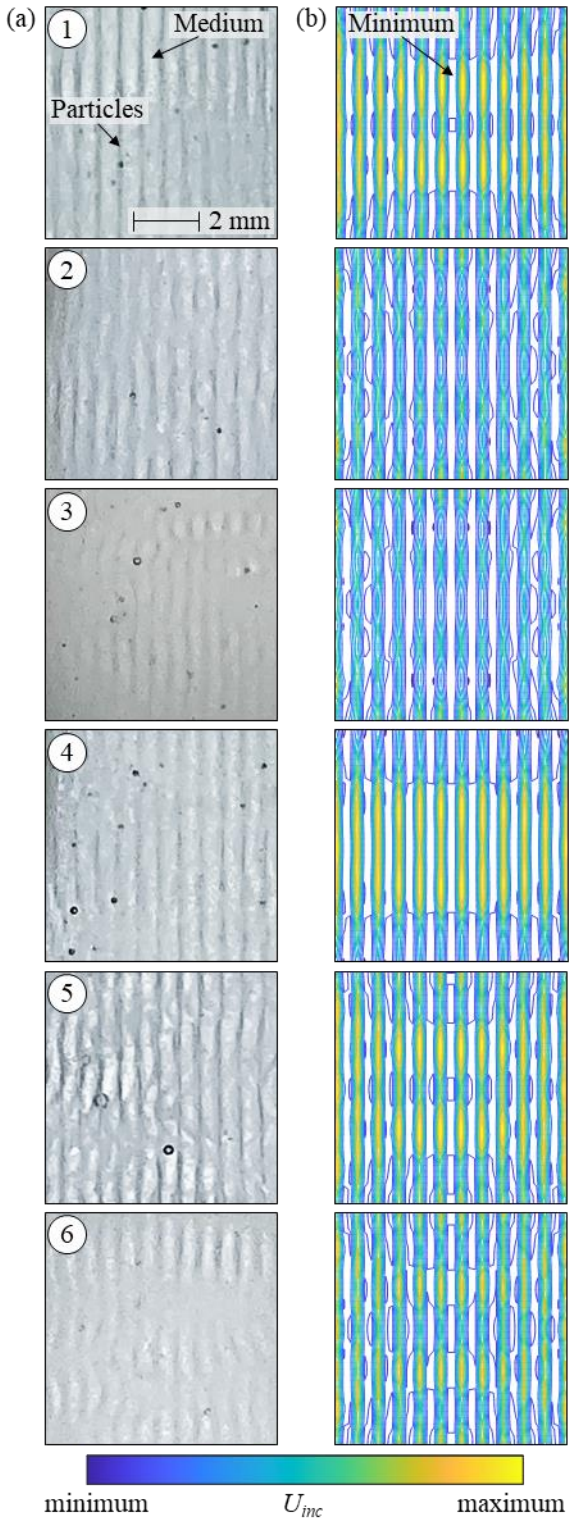

Figure 2.4: (a) Experimental results for each numbered label in Fig. 2.3, showing lines of aligned particles (dark) in viscous medium (bright), and (b) the corresponding simulation results of the time-averaged primary acoustic radiation potential U_{inc}.

2.4. Conclusion

In conclusion, the steady-state locations where spherical particles organize during ultrasound DSA are different in a viscous and inviscid medium and depend on particle volume fraction Φ and medium viscosity η_m. We experimentally measure the deviation between locations where particles assemble as a function of particle volume fraction Φ, medium viscosity η_m, and operating frequency *f*. Furthermore, we simulate the experiments by implementing an ultrasound DSA simulation that integrates the Helmholtz equation with a complex wave number k to account for particle volume fraction Φ, in combination with the primary acoustic radiation potential theory that accounts for medium viscosity η_m [31]. The maximum difference between experiments and simulations is 10%. We provide best-fit equations to predict the deviation between locations where particles accumulate during ultrasound DSA in viscous and inviscid media. The deviation increases with increasing particle volume fraction and medium viscosity because the sound propagation velocity of the mixture of particles and viscous medium changes compared to that of the inviscid medium. When considering ultrasound DSA of a periodic pattern of lines of particles, we determine a 3% maximum deviation between adjacent particle locations but note that this deviation scales with the dimensions of the experiment/simulation. These results have implications for using ultrasound DSA as a fabrication process for, e.g. engineered polymer matrix composite materials whose properties depend on the spatial organization of patterns of particles in the matrix material.

2.5. Acknowledgments

This research was supported by the National Science Foundation under award no. 2017588.

2.6. References

[1] Greenhall, J., Homel, L., and Raeymaekers, B., 2019, "Ultrasound Directed Self-Assembly Processing of Nanocomposite Materials with Ultra-High Carbon Nanotube Weight Fraction," J. Compos. Mater., **53**(10), pp. 1329–1336.

[2] Niendorf, K., and Raeymaekers, B., 2021, "Additive Manufacturing of Polymer Matrix Composite Materials with Aligned or Organized Filler Material: A Review," Adv. Eng. Mater., **2001002**, pp. 1–18.

[3] Evans, J. M., and Attenborough, K., 1997, "Coupled Phase Theory for Sound Propagation in Emulsions," J. Acoust. Soc. Am., **102**(1), pp. 278–282.

[4] Urick, R. J., 1947, "A Sound Velocity Method for Determining the Compressibility of Finely Divided Substances," J. Appl. Phys., **18**(11), pp. 983–987.

[5] Ament, W. S., 1953, "Sound Propagation in Gross Mixtures," J. Acoust. Soc. Am., **25**(4), pp. 638–641.

[6] Harker, A. H., and Temple, J. A. G., 1988, "Velocity and Attenuation of Ultrasound in Suspensions of Particles in Fluids," J. Phys. Appl. Phys., **21**(11), pp. 1576–1588.

[7] Epstein, P. S., and Carhart, R. R., 1953, "The Absorption of Sound in Suspensions and Emulsions. I. Water Fog in Air," J. Acoust. Soc. Am., **25**(3), pp. 553–565.

[8] Allegra, J. R., and Hawley, S. A., 1972, "Attenuation of Sound in Suspensions and Emulsions: Theory and Experiments," J. Acoust. Soc. Am., **51**(5B), pp. 1545–1564.

[9] McClements, D. J., 1992, "Comparison of Multiple Scattering Theories with Experimental Measurements in Emulsions," J. Acoust. Soc. Am., **91**(2), pp. 849–853.

[10] Schwarz, W. H., 1994, "A Multiphase Continuum Theory for Sound Wave Propagation through Dilute Suspensions of Particles," J. Acoust. Soc. Am., **96**(1), pp. 319–331.

[11] Doinikov, A. A., 1997, "Acoustic Radiation Force on a Spherical Particle in a Viscous Heat-Conducting Fluid. I. General Formula," J. Acoust. Soc. Am., **101**(2), pp. 713–721.

[12] Settnes, M., and Bruus, H., 2012, "Forces Acting on a Small Particle in an Acoustical Field in a Viscous Fluid," Phys. Rev. E - Stat. Nonlinear Soft Matter Phys., **85**(1), pp. 1–12.

[13] Kinsler, L. E., Frey, A. R., Coppens, A. B., and Sanders, J. V., 2000, *Fundamental of Acoustic*, John Wiley & Sons, Inc, New York.

[14] Greenhall, J., Guevara Vasquez, F., and Raeymaekers, B., 2016, "Ultrasound Directed Self-Assembly of User-Specified Patterns of Nanoparticles Dispersed in a Fluid Medium," Appl. Phys. Lett., **108**(10), pp. 1–5.

CHAPTER 3

MEASURING AND SIMULATING THE LOCAL PACKING DENSITY RESULTING FROM ULTRASOUND DIRECTED SELF-ASSEMBLY OF SPHERICAL MICROPARTICLES INTO SPECIFIC PATTERNS

Adapted with permission from Noparast, S., Guevara Vasquez, F., Francoeur, M., and Raeymaekers, B., 2023, "Measuring and Simulating the Local Packing Density Resulting From Ultrasound-Directed Self-Assembly of Spherical Microparticles into Specific Patterns," Phys. Rev. Appl., **19**(6), p. 064087.

3.1. Introduction

The acoustic radiation force results from scattering, and drives particles to the locations where the acoustic radiation force approaches zero, and the time-averaged acoustic radiation potential is locally minimum. Thus, the particle packing density is higher where particles assemble than outside of those locations, or compared to when particles are randomly dispersed in the fluid medium.

In this Chapter, we quantify the local particle packing density within the pattern features that result from ultrasound DSA, as a function of particle volume fraction, particle size, and medium viscosity. This knowledge is particularly important when using ultrasound DSA to manufacture materials where high particle packing density is required, e.g. to increase mechanical [1] or electrical [2] properties, or to tailor the combustion of energetic particles [3–5], among other applications.

The literature defines the particle packing density as the volume fraction of a control volume occupied by solid material [6]. Theoretical work documents the maximum packing density of spherical particles in different configurations, including body-centered cubic (BCC) = 0.68 and face-centered cubic (FCC) = 0.74 [7]. Additionally, the maximum packing density of randomly organized spherical particles is between 0.55-0.63 [8–10]. Others document that the particle packing density increases with particle volume fraction [6], independent of particle size [10]. Additionally, the literature documents comparisons between experiments and theoretical results of particle packing density measurements [11,12]. Mixing two (binary distribution) and three (ternary distribution) particle sizes increases the packing density compared to that of a single particle size, because small particles fit in cavities between large particles [13]. Furthermore, for a binary

distribution, the particle packing density increases with increasing particle size ratio but also depends on the particle volume fraction of small and large particle sizes [10,13–15].

Specifically related to particle packing density resulting from ultrasound DSA, Niendorf et al. [16] determined the microscale and macroscale alignment of microfibers using ultrasound DSA as a function of particle volume fraction. They concluded that microscale and macroscale microfiber alignment decrease and increase, respectively, with increasing volume fraction as a result of increasing microscale entanglement and increasing number of fibers. Additionally, Greenhall et al. [1] documented that the mechanical properties of the engineered polymer matrix composite materials increase with increasing volume fraction of carbon nanotubes, and they quantified the local particle volume fraction after ultrasound DSA. Similarly, Scholtz et al. [17] reported increasing mechanical properties with increasing volume fraction of glass fibers. Thus, changing the local packing density of particles allows tuning the properties of the engineered polymer matrix composite material.

To our knowledge, no other work relates the ultrasound DSA process parameters to the local particle packing density within the pattern features that result from ultrasound DSA, despite its importance in manufacturing engineered polymer matrix composite materials with tailored properties. Thus, the objective of this paper is to theoretically derive and experimentally validate a three-dimensional (3D) model to simulate, quantify, and predict the local packing density of spherical particles at the pattern features that result from ultrasound DSA. We quantify the 3D particle packing density using numerical simulations of the ultrasound DSA process. Additionally, we experimentally measure the local particle packing density within the pattern features that result from ultrasound DSA, fixated in place using a vat polymerization setup.

3.2. Methods and materials

3.2.1. Theoretical model and simulation

We simulate the 3D assembly of spherical particles dispersed in a viscous medium contained in a reservoir, during the ultrasound DSA process, as a function of particle volume fraction, particle size, and medium viscosity. Figure 3.1 (a) schematically illustrates a spherical particle in a viscous medium exposed to an ultrasound wave field, showing the forces acting on the particle, in addition to the local normalized acoustic pressure and the acoustic radiation potential. A particle with radius a experiences the acoustic radiation force **F** that drives it to the local minimum of the time-averaged acoustic radiation potential, in addition to the Stokes' drag force with Oseen's correction $\mathbf{F}_d$ that resists the motion of the particle in the viscous medium. Also, each particle experiences both gravity $\mathbf{F}_g$ and buoyancy forces $\mathbf{F}_b$, which depend on the mass of the particle and the density of the viscous medium, respectively. In our model, when particles collide with each other or the wall of the reservoir that contains the mixture of particles and viscous medium, we use a truncated Lennard-Jones-like potential to create a repulsive force $\mathbf{F}_{LJ}$ that accounts for the collisions. Figure 3.1 (b) schematically shows a reservoir with two ultrasound transducers affixed to opposing walls, which contains a mixture of spherical particles dispersed in a viscous medium. Energizing the ultrasound transducers establishes a standing ultrasound wave in the reservoir, which we simulate at the N_d domain points in the 3D solution domain that covers the entire reservoir (red dots in Fig. 3.1 (b)) using the boundary element method (BEM) based on the Helmholtz equation $\nabla^2\varphi_{inc} + \tilde{k}^2\varphi_{inc} = 0$. Here, $k = (\omega / c_m) / (1 - i\omega\tau_s)^{1/2}$ is the complex wave number that accounts for acoustic attenuation in a viscous medium [18] and φ_{inc} is the incident velocity potential. $\omega = 2\pi f$ and f are the angular and temporal frequency of the ultrasound wave field, c_m is the sound propagation velocity within the viscous medium, $\tau_s = 4\eta_m/3\rho_m c_m^2$ is the relaxation time

(i.e., viscous dissipation time to dampen the acoustic pressure to 1/e of its original value), with η_m and ρ_m the viscosity and density of the viscous medium, and $i = (-1)^{1/2}$ [18].

We represent the reservoir as a simply-closed boundary with N_b boundary elements that enclose the 3D solution domain with N_d domain points. A boundary element j represents either a part of the reservoir wall with velocity $v_j = 0$, or a part of an ultrasound transducer that acts as a piston source with velocity $v_j = v_0 e^{i(\omega t - \theta)}$ along its normal direction $\mathbf{n}_j$, with v_0 the real velocity amplitude and ω and θ the angular frequency and phase of the ultrasound wave, respectively. We impose the impedance boundary condition $\partial \varphi_{inc} / \partial \mathbf{n}_j + ikZ\varphi_{inc} = v_j$ at each boundary element, with $k = \omega/c_m = 2\pi/\lambda$ and λ is the wavelength of the standing ultrasound wave. $Z = Z_m / Z_b$ accounts for the absorption and reflection of the ultrasound wave at the boundary of the reservoir; we maintain the acoustic impedance Z_b constant along the entire boundary, and the acoustic impedance of the medium is $Z_m = \rho_m c_m$.

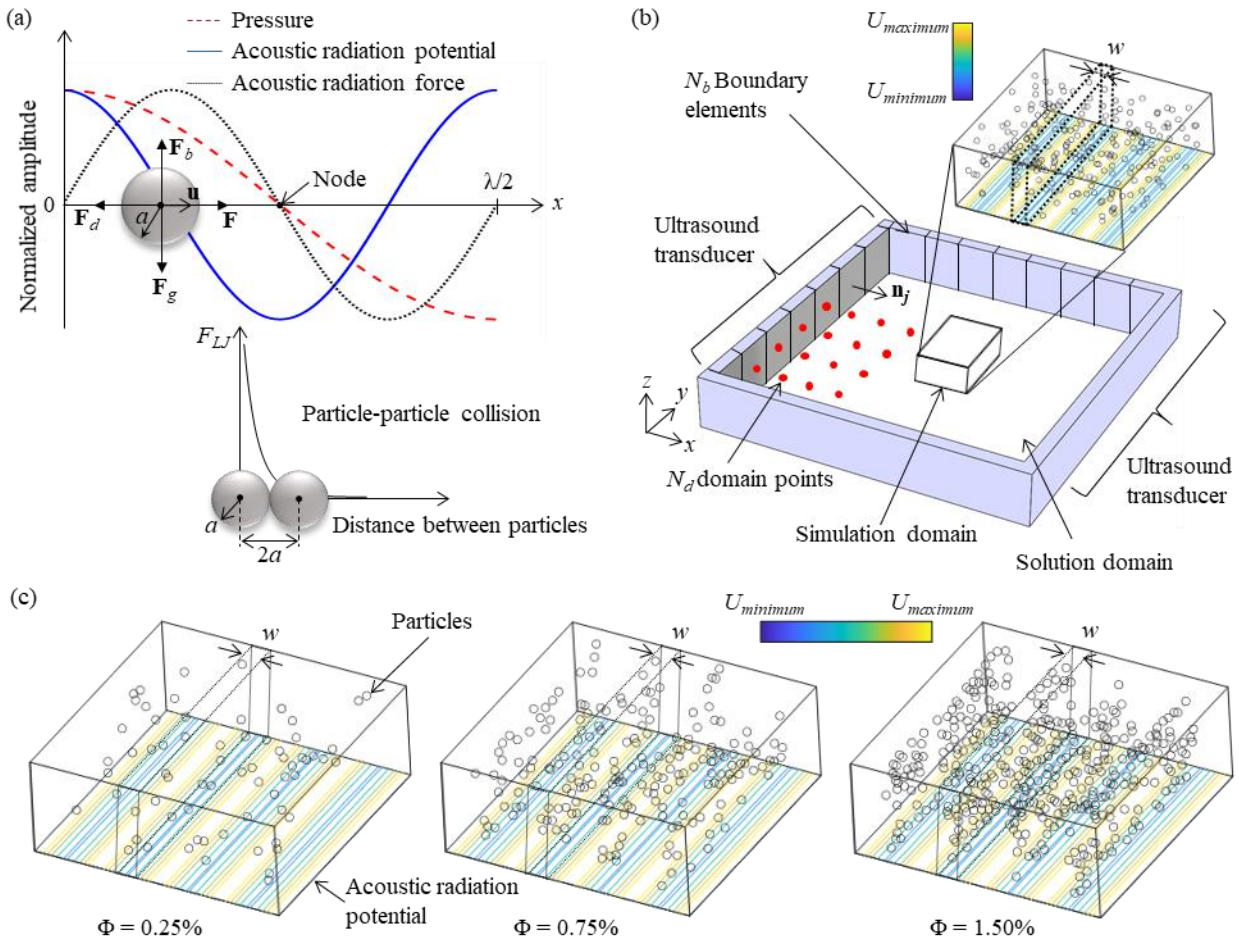

Figure 3.1: (a) Schematic of a spherical particle in a viscous medium, and in a standing ultrasound wave field during ultrasound DSA, indicating the different forces acting on the particle. (b) Schematic of the 3D theoretical model of the reservoir with two ultrasound transducers affixed to opposing walls that contains the mixture of spherical particles dispersed in the viscous medium, showing the solution domain within a simply-closed boundary. (c) Simulated 3D particle location for different particle volume fractions.

We simulate the 3D motion of N non-overlapping particles, randomly dispersed in the fluid medium as a function of time, resulting from the forces acting on the particles (see Fig. 3.1 (a)). The N particles are located in the particle simulation domain, which is the center section of the solution domain (see Fig. 3.1 (b)), because it is too computationally expensive to track particles in the entire solution domain. We calculate the velocity potential φ resulting from single scattering of all spherical particles in the 3D particle simulation domain, and we assume they behave like monopole and dipole scatterers, with $ka << 1$. $k = \Re\{\tilde{k}\} = 2\pi/\lambda$ is the wave number and λ is the

wavelength of the standing ultrasound wave. The velocity potential at location $\mathbf{r}_i$ of the i^{th} particle is given as [19]

$$\varphi(\mathbf{r}_i) = \varphi_{inc}(\mathbf{r}_i) + \sum_{\substack{j=1 \\ j\neq i}}^{N} \varphi_{sc}(\mathbf{r}_i \mid \mathbf{r}_j)\,, \tag{3.1}$$

which is the superposition of the incident velocity potential φ_{inc} at $\mathbf{r}_i$ calculated using the BEM method, and the sum of velocity potentials resulting from single scattering off all N particles j at $\mathbf{r}_j$. The scattered velocity potential from the j^{th} particle at the location of the i^{th} particle $\mathbf{r}_i$ is [19]

$$\varphi_{sc}(\mathbf{r}_i \mid \mathbf{r}_j) = -i\left(ka\right)^3 \left[\frac{f_1}{3} h_0^{(1)}(k\left\|\mathbf{r}_i - \mathbf{r}_j\right\|)\varphi_{inc}(\mathbf{r}_j) - \frac{f_2}{2} h_1^{(1)}(k\left\|\mathbf{r}_i - \mathbf{r}_j\right\|) \frac{\partial \varphi_{inc}(\mathbf{r}_j)}{\partial(k\left\|\mathbf{r}_i - \mathbf{r}_j\right\|)} \right] \tag{3.2}$$

with $f_1 = 1\text{-}\beta_p/\beta_m$ and $f_2 = \Re\{[2(1\text{-}\gamma)(\rho_p/\rho_m\text{-}1)]/[2\rho_p/\rho_m\text{+}1\text{-}3\gamma]\}$. Here, $\gamma = -3/2[1+i(1+\delta/a)]\delta/a$, with $\delta = (2\eta_m/\omega\rho_m)^{1/2}$ the viscous boundary layer thickness around a particle [20]. $\beta_p = 1/[\rho_p(c_{p,c}^2 - 4c_{p,s}^2/3)]$, ρ_p, $\beta_m = 1/(\rho_m c_m^2)$, and ρ_m are the compressibility and the density of the spherical particle and medium, respectively [21]. $c_{p,c}$ and $c_{p,s}$ represent the compressional and shear wave propagation velocities. $h_0^{(1)}(z) = -ie^{iz}/z$ and $h_1^{(1)}(z) = -e^{iz}(z+i)/z^2$ are 0^{th} and 1^{st} order spherical Hankel functions of the first kind [22]. $\|\mathbf{r}_i\text{-}\mathbf{r}_j\|$ is the Euclidean distance between locations $\mathbf{r}_i$ and $\mathbf{r}_j$, and $\partial\varphi_{inc}(\mathbf{r}_j) / \partial\left\|\mathbf{r}_i - \mathbf{r}_j\right\|$ is the derivative of the incident velocity potential at location $\mathbf{r}_j$ in the direction of $\mathbf{r}_i$ - $\mathbf{r}_j$. We emphasize that in our model, the particle simulation domain is several wavelengths removed from the boundaries of the solution domain and, thus, we assume that the interaction between the scattered wave field and the boundary elements is negligible. Note that the monopole scattering coefficient f_1 involves the compressibility contrast of the particles and the medium, whereas the dipole scattering coefficient f_2 involves the mass density contrast and it also accounts for the effect of medium viscosity on dipole scattering. Doinikov [23] also emphasized that the thermal effects can cause imperfect behavior of the medium surrounding the particle in a

standing ultrasound wave, which affects the monopole scattering coefficient f_1 when the depth of penetration of the thermal wave $\delta_t = [2\kappa_m/(\rho_m c_{p,m}\omega)]^{1/2}$ is comparable to the particle radius a. κ_m and $c_{p,m}$ are the thermal conductivity and specific heat of the medium, respectively. For the range of parameters in this work $0.005 \leq \delta_t/a \leq 0.02$ and, thus, we neglect the thermal effects in our 3D simulation model.

The ultrasound wave velocity $v = \nabla\varphi$ and the pressure $p = i\rho_m\omega\varphi$. Hence, the time-averaged acoustic radiation potential U in the viscous medium is [20]

$$U = \frac{4\pi}{3}a^3\left(f_1\frac{\beta_m}{2}\left\langle p^2\right\rangle - f_2\frac{3\rho_m}{4}\left\langle v^2\right\rangle\right). \tag{3.3}$$

Operators $\langle\bullet\rangle$ and $\Re\{\bullet\}$ represent the time average over a wave period and the real part of the expression, respectively. The acoustic radiation force $\mathbf{F} = -\nabla U$. Thus, we first calculate the incident velocity potential φ_{inc} in all domain points of the solution domain using a complex wave number in the Helmholtz equation to account for the acoustic wave attenuation. Second, we calculate the velocity potential φ in all domain points of the particle simulation domain as the summation of the incident velocity potential φ_{inc} and single monopole and dipole scattering from other particles in the simulation domain. Finally, we calculate the acoustic radiation potential and force on all particles in the particle simulation domain.

Additionally, the Stokes drag force with Oseen's correction that acts on each particle is $\mathbf{F}_d = 12\pi a^2\rho_m||\mathbf{u}||^2(1+3/16Re)/Re$, which orients in the same direction and opposite sense of the particle velocity $\mathbf{u}$. $Re = 2\,a\rho_m||\mathbf{u}||/\eta_m$ is the Reynolds number [24]. Furthermore, we account for particle-particle and particle-wall collisions using the repulsive portion of a Lennard-Jones-like potential $V_{LJ} = 4\varepsilon_{LJ}(2a/r)^{12}$. The force acting on two particles within a distance r of each other is $\mathbf{F}_{LJ} = -\nabla V_{LJ}$ [25]. We tune ε_{LJ} following an iterative procedure in which we average the smallest

distance between neighboring particles over a finite time until the average minimum distance between colliding particles equals $2a$ (+/-2%) and between particles and a wall equals a (+/-2%).

We simulate the ultrasound DSA process over a duration $0 \leq t \leq T$ with time step Δt. When $t = 0$, the particles are stationary $\|\mathbf{u}\| = 0$ and dispersed at randomly chosen, non-overlapping locations in the 3D particle simulation domain. When $t > 0$, $\|\mathbf{u}\| \neq 0$ because the sum of all forces acting on the particle (see Fig. 3.1 (a)) accelerates the particle towards a local minimum of the time-averaged acoustic radiation potential, where the particles assemble. In each time step Δt, we calculate the location and velocity of each particle $\mathbf{u}$ after accounting for particle-particle collisions.

Finally, when all particles have assembled at $t = T$, we determine the 3D particle packing density as the volume of particles within a cuboid of width w around the local minimum of the time-averaged acoustic radiation potential (node of the standing ultrasound wave) divided by the volume of the cuboid. Figure 3.1 (c) illustrates this concept, showing a cuboid of width w (dashed line) around the node of the standing ultrasound wave, highlighting the particles that are partially or fully enclosed by it. The color map shows the time-averaged acoustic radiation potential in arbitrary units. We determine w based on the experiments (see Section 2.2).

We define three non-dimensional parameters based on dimensional analysis using the Buckingham π theorem, which characterizes the local particle packing density at the pattern features that result from ultrasound DSA. We consider the following parameters in the simulations: the particle volume fraction $0 \leq \Phi \leq 27.5\%$ to show the maximum reachable local packing density, the non-dimensional particle size $0.05 \leq K_1 = ka \leq 0.20$ to not violate the Rayleigh regime assumption ($ka << 1$), and the non-dimensional viscosity of the medium $3.3 \cdot 10^3 \leq K_2 = \rho_m \lambda c_m / \eta_m$

$\leq 9.8 \cdot 10^3$. The range of K_2 derives from the medium viscosity $150 \leq \eta_m \leq 450$ mPa.s to span the viscosity of commercial photopolymer resins.

3.2.2. Experimental setup and parameter study

Figure 3.2 (a) schematically shows the experimental setup we use to manufacture material specimens for a full-factorial study of the local particle packing density as a function of Φ and K_1. Parameter K_2 does not affect the steady-state local packing density after ultrasound DSA; it only determines the speed by which particles assemble, which we do not consider in this work. The setup is based on a VP digital light processing (DLP) printer (mUVe 1.1 DLP, Grand Rapids, MI, USA), augmented with an acrylic, square reservoir with two ultrasound transducers (piezoelectric ceramic plate, center frequency f_c = 1.5 MHz, Steminc, FL, USA) affixed to opposing walls, to perform ultrasound DSA of particles dispersed in the photopolymer resin. A function generator (Tektronix AFG 3102, Beaverton, OR, USA) and radio frequency (RF) power amplifier (E&I 2100L, Rochester, NY, USA) energize the ultrasound transducers. The operating frequency f of the ultrasound wave field is close to the center frequency f_c of the ultrasound transducers. We use standard photopolymer resin (3DRS standard V2 gray resin, c_m = 1,420 m/s, ρ_m = 1,100 kg/m^3, η_m = 218 mPa.s, 3D Resin Solutions, IL, USA) and spherical aluminum microparticles (a = 15 μm and 22 μm, $c_{p,c}$ = 6,420 m/s, $c_{p,s}$ = 3,040 m/s, ρ_p = 2,710 kg/m^3 [26], US5005 solid aluminum spherical powder, US Research Nanomaterials, Inc., TX, USA). Based on these materials, the values of non-dimensional parameters are $0 \leq \Phi \leq 1.50\%$, K_1 = 0.1 and 0.15, and $K_2 = 6.8 \cdot 10^{-3}$. The ranges of parameter values are driven by the feasibility of the experiments and relevance to manufacturing of engineered polymer matrix composite materials. Increasing the particle volume fraction increases acoustic wave attenuation, which decreases the magnitude of the acoustic

radiation force and, thus, the ability to assemble particles at the nodes of the standing ultrasound wave. Furthermore, it increases the viscosity of the mixture of particles and medium, which requires increasing the acoustic radiation force to overcome the drag force exerted on the particles. Finally, it also increases the curing time required to fabricate a composite material specimen in the VP setup, which potentially leads to distortion of the pattern features. Thus, we choose particle sizes (a = 15 μm and 22 μm) that satisfy the Rayleigh regime assumption (ka = 0.10 and 0.15 << 1) and are observable under an optical microscope. In addition, increasing the particle size increases their mass, which could cause them to precipitate to the bottom of the reservoir prior to assembly into pattern features. The choice of the medium viscosity (η_m = 218 mPa.s) results from the availability of commercial photopolymer resins.

We disperse a volume fraction Φ of particles in the photopolymer resin using sonication to minimize particle aggregation (80 Watt, 2 minutes, UP200Ht, Hielscher, Teltow, Germany), after which we energize the ultrasound transducers for T = 10 s. The acoustic radiation force drives the particles to the nodes of the standing ultrasound wave, where they assemble and agglomerate. We fixate them in place by curing a 12 x 12 mm specimen using the DLP light source in the VP printer for 8 s. We post-cure the specimen outside the DLP printer for 120 s, to eliminate any liquid resin. Figure 3.2 (a) shows a typical material specimen after curing (Φ = 1.00 %, K_1 = 0.10).

We experimentally measure the local particle packing density as the volume of particles within a cuboid of width w around the location where particles assemble (node of the standing ultrasound wave) divided by the volume of the cuboid, as a function of the non-dimensional parameters Φ and K_1. The measurement is based on the notion that particle area fraction (the fraction of a surface covered by particles) is a good approximation to the 3D particle packing density, as originally documented by Underwood [27], and verified for accuracy using our 3D

simulation model (maximum 4% error at Φ = 1.5%). Thus, the particle area fraction within a rectangle of width w around where particles assemble represents the particle packing density within a cuboid of width w around where particles assemble. Figure 3.2 (b) schematically illustrates the measurement. We obtain optical micrographs (1.5 μm spatial resolution, 180X magnification, AmScope, CA, USA) of locations where we qualitatively observe good organization of the microparticles at the nodes of the standing ultrasound wave. The photopolymer matrix appears dark and the aluminum microparticles appear bright-colored in a typical optical microscopy image (see Fig. 3.2 (b)). To accurately determine the surface area covered by aluminum particles, we binarize the image using a threshold that equates the particle area fraction of the entire image to the particle volume fraction Φ used to manufacture the material specimens (see Fig. 3.2 (b)). Thus, we focus the optical microscope on the top surface of the specimen and ensure to only consider particles on the surface of the specimen and not in the bulk, while simultaneously controlling for external influences, such as lighting conditions and glare. For each microscopy image, we determine the particle area fraction and, thus, the particle packing density, within a domain $w = Na$ centered around a node of the standing ultrasound wave, and we compare the experimental and simulation results (see Fig. 3.2 (b)). We select $N = 6$, i.e., $w = 6a$ to encompass most particles that assemble at the node of a standing ultrasound wave, based on experiments with Φ = 1.00%. We repeat each measurement three times for different material specimens and report the average, minimum, and maximum.

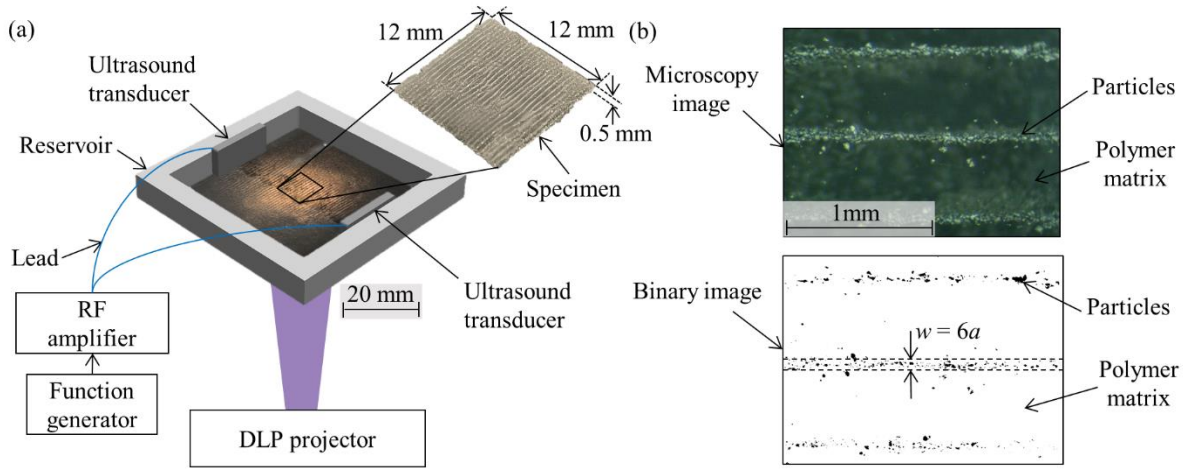

Figure 3.2: (a) Schematic of the experimental setup, showing the VP DLP printer augmented with ultrasound DSA, and illustrating a typical material specimen that consists of photopolymer and aluminum particles. (b) Schematic of the measurement methodology, showing an optical micrograph with the corresponding binary image, and indicating the domain $w = 6a$ over which we determine the particle packing density.

3.3. Results and discussion

Figure 3.3 shows the results of the full-factorial parameter study of the local particle packing density as a function of ultrasound DSA operating parameters. Figure 3.3 (a) shows the local particle packing density at the location where particles assemble (node of the standing ultrasound wave) as a function of the particle volume fraction Φ and the non-dimensional particle size K_1. We show the particle packing density obtained from simulations PD_{sim} (hollow markers) and experiments PD_{exp} (solid markers) for $K_1 = 0.10$ (black dot) and $K_1 = 0.15$ (blue square). The solid markers represent the average of three experiments, whereas the error bars show the minimum and maximum values. Furthermore, we label the data points in Fig. 3.3 (a) and provide the corresponding optical microscopy images and binary images (white = resin, black = particles) in Fig. 3.3 (b) to illustrate the results. Figure 3.3 (c) shows magnified binary images.

From Fig. 3.3 we observe that the particle packing density increases with increasing volume fraction Φ and with decreasing K_1, as expected. Increasing Φ increases the number of particles at the node of the standing ultrasound wave because when $\Phi < 1.5\%$, the maximum local

packing density is less than 10% (see Fig. 3.3 (a)), which is much smaller than the maximum theoretical packing density for spherical particles of approximately 60% [8]. Furthermore, decreasing $K_1 = ka$ either requires reducing k, which increases λ and, thus, increases the number of particles that assemble at a node of the standing ultrasound wave (for constant Φ). Alternatively, it requires reducing a, which increases the number of particles for constant Φ, thus increasing the particle packing density at a node of the standing ultrasound wave. Also, we observe from Fig. 3.3 that the theoretical simulations and experimental results are in excellent agreement for particle volume fractions $\Phi < 1.5\%$, and we determine a maximum 6.5% error ($K_1 = 0.10$, $\Phi = 0.75\%$).

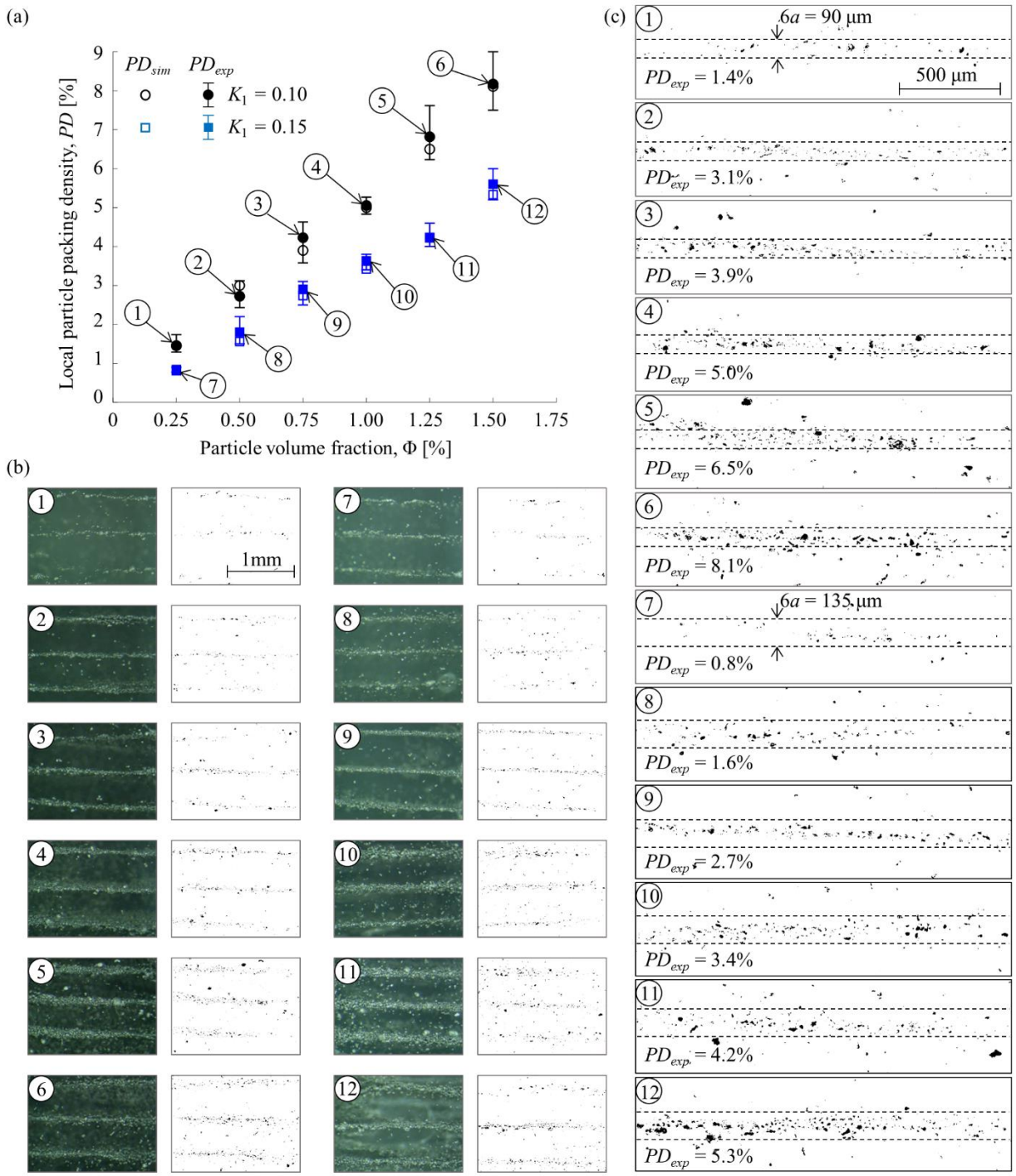

Figure 3.3: (a) Local packing density within the pattern features that result from ultrasound DSA (node of the standing ultrasound wave) as a function of the particle volume fraction Φ, showing simulation PD_{sim} (hollow markers) and experiment PD_{exp} (solid markers) results for K_1 = 0.10 (black dot) and K_1 = 0.15 (blue square). (b) Optical microscopy images and binary images (white = resin, black = particles) for the data points in (a). (c) Magnified binary images that show the particles (black) and the domain over which we quantify PD_{exp}.

Additionally, we use the theoretical model, for which we document experimental validation in Fig. 3.3, to understand the effect of Φ, K_1, and K_2 on the local particle packing density after ultrasound DSA, covering the entire ultrasound DSA process envelope. Figure 3.4 shows the local packing density PD_{sim} at the location where particles assemble (node of the standing ultrasound wave) as a function of the particle volume fraction $0.75\% \leq \Phi \leq 27.5\%$, and as a function of the non-dimensional particle size $0.05 \leq K_1 \leq 0.20$. We derive logistic curve best-fit equations to predict the particle packing density at the pattern features that result from ultrasound DSA (see Fig. 3.4) or, conversely, to determine the particle volume fraction Φ required to obtain a specific particle packing density. From Fig. 3.4, we observe that the particle packing density increases with increasing particle volume fraction Φ and with decreasing K_1, similar to the results of Fig. 3.3. However, we observe that the local particle packing density at the node of the standing ultrasound wave converges to 45%, independent of K_1, which is close to the maximum random particle packing density of spheres in 3D. Finally, we note that Fig. 3.4 includes parameter values that extrapolate beyond the parameter ranges used in the experimental validation and, thus, must be interpreted with caution.

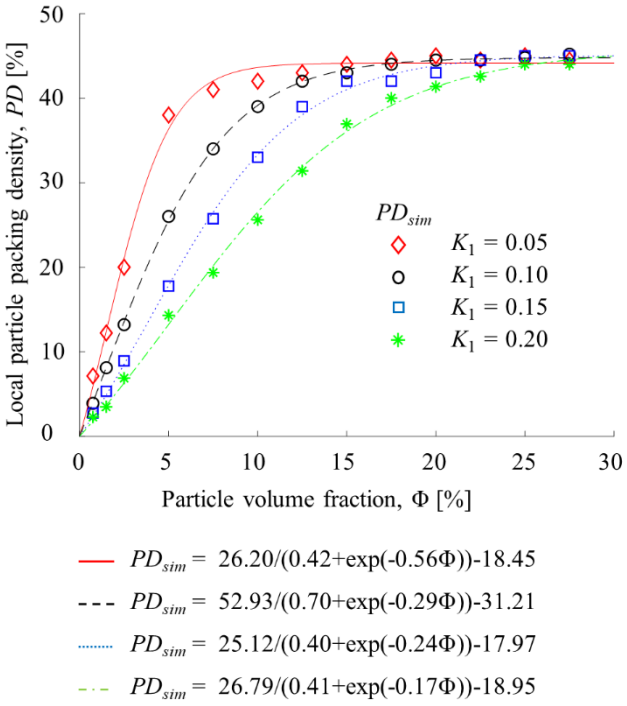

Figure 3.4: Local packing density within the pattern features that result from ultrasound DSA (node of the standing ultrasound wave) as a function of the particle volume fraction Φ, for $0.05 \leq K_1 \leq 0.20$.

Figure 3.5 shows the local packing density PD_{sim} at the location where particles assemble (node of the standing ultrasound wave) for $K_1 = 0.10$ as a function of the particle volume fraction Φ and the non-dimensional viscosity of the mixture of particles and photopolymer $3.3 \times 10^3 \leq K_2 \leq 9.8 \times 10^3$. We derive logistic curve best-fit equations to predict the particle packing density at the pattern features that result from ultrasound DSA or, conversely, to determine the particle volume fraction Φ required to obtain a specific particle packing density. From Fig. 3.5, we observe that the particle packing density increases with increasing particle volume fraction Φ, independent of K_2, similar to the results of Fig. 3.3 and 3.4. We also observe that the local particle packing density at the node of the standing ultrasound wave converges to 45%, independent of K_2, which is close to the maximum random particle packing density of spheres in 3D. Thus, K_2 does not affect the local particle packing density; it only affects the speed by which particles assemble at the

nodes. We account for the effect of medium viscosity on the attenuation of the incident wave, dipole scattering, and the amplitude of the acoustic radiation potential. However, the medium viscosity can also induce nonlinear phenomena such as streaming at the reservoir walls and even microstreaming around particles [28,29]. These phenomena can affect the local packing density for particle volume fractions $\Phi > 1.5\%$.

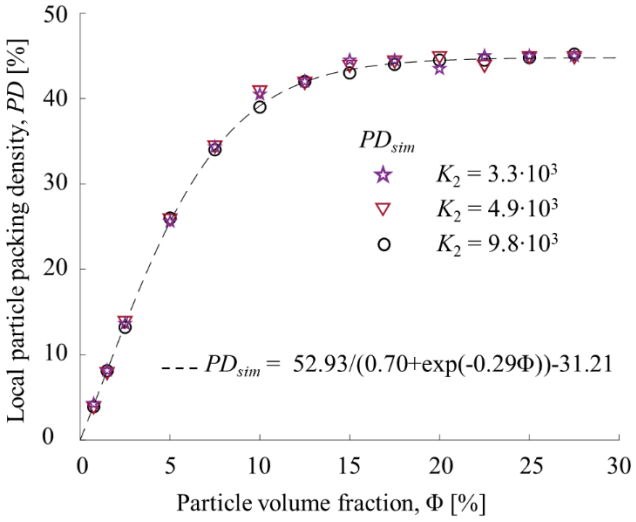

Figure 3.5: Local packing density within the pattern features that result from ultrasound DSA (node of the standing ultrasound wave) as a function of the particle volume fraction Φ, for $3.3 \times 10^3 \leq K_2 \leq 9.8 \times 10^3$, and with $K_1 = 0.10$.

Figure 3.6 shows the local particle packing density PD_{sim} at the location where particles assemble (node of the standing ultrasound wave) for $K_1 = 0.10$ and $K_2 = 3.3 \times 10^3$ as a function of the particle volume fraction Φ with logistic curve best-fit equations, when considering single monopole and dipole scattering (black circle) and when considering single monopole and dipole scattering (black circle) and when only considering scattering resulting from the incident wave (blue triangle). From Fig. 3.6, we observe that the local particle packing density at the node of the standing ultrasound wave converges to 45% and 53% when we consider and neglect single monopole and dipole scattering, respectively. We attribute this difference to a repulsive acoustic particle interaction force that results from scattering, which agrees with results from Pavlic et al.

[29], who report a repulsive acoustic interaction force in the direction of wave propagation between two copper microparticles (a = 5 μm, and ka = 0.01), and Silva and Bruus [19]. We also point out that based on modeling the interactions between particles using monopole and dipole scattering, one can also derive the interaction force between spherical particles [19].

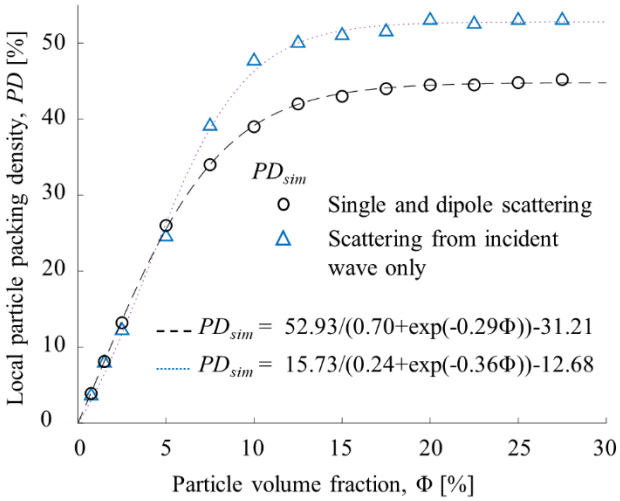

Figure 3.6: Local particle packing density within the pattern features that result from ultrasound DSA (node of the standing ultrasound wave) as a function of the particle volume fraction Φ with $K_1 = 0.10$ and $K_2 = 3.3 \times 10^3$, accounting for single monopole and dipole scattering (black circles) and when only considering scattering resulting from the incident wave (blue triangles).

3.4. Conclusions

This chapter presents a 3D theoretical model of ultrasound DSA in a viscous medium with multiple particles, which allows simulating the locations of spherical particles in an ultrasound wave field as a function of time, and quantifying the local packing density at locations where particles assemble. Based on the results of the experiments and simulations, we conclude that:

1. The local particle packing density at the pattern features that result from ultrasound DSA depends on the particle volume fraction and particle size, because they determine the number of particles that assemble in one location, and how they pack together.

2. The viscosity of the medium in which we organize the particles does not affect the local particle packing density resulting from ultrasound DSA, but it determines the time particles require to assemble in specific pattern because increasing viscosity increases the drag force acting on the particles.
3. The maximum achievable local particle packing density is 45%, independent of particle size and medium viscosity. However, the volume fraction required to achieve the maximum particle packing density decreases with decreasing particle size.

We note that while we provide experimental validation of the model for particle volume fractions $\Phi < 1.5\%$, our simulation results extrapolate beyond $\Phi = 1.5\%$ and, thus, results must be interpreted with caution. The results of this work enable predicting the volume fraction of particles required to obtain a specific local particle packing density at the specific pattern features that result from ultrasound DSA and, thus, contribute to the physical understanding of this process, which is useful in the context of manufacturing engineered polymer matrix composite materials with ultrasound DSA and VP. Specifically, this work has implications for fabricating engineered composite materials with a high or a specific local particle packing density to tailor the properties of the composite material.

3.5. Acknowledgments

This research was supported by the National Science Foundation under awards CMMI-2130083 and DMS-2008610.

3.6. References

[1] Greenhall, J., Homel, L., and Raeymaekers, B., 2019, "Ultrasound Directed Self-Assembly Processing of Nanocomposite Materials with Ultra-High Carbon Nanotube Weight Fraction," J. Compos. Mater., **53**(10), pp. 1329–1336.

[2] Niendorf, K., and Raeymaekers, B., 2021, "Combining Ultrasound Directed Self-Assembly and Stereolithography to Fabricate Engineered Polymer Matrix Composite Materials with Anisotropic Electrical Conductivity," Compos. Part B Eng., **223**, p. 109096.

[3] White, K. J., Stobie, I., Oberle, W., Katulka, G., and Driesen, S., 1997, "Combustion Control Requirements in High Loading Density, Solid Propellant ETC Gun Firings," IEEE Trans. Magn., **33**(1), pp. 350–355.

[4] Yang, W., Hu, R., Zheng, L., Yan, G., and Yan, W., 2020, "Fabrication and Investigation of 3D-Printed Gun Propellants," Mater. Des., **192**, p. 108761.

[5] Driel, C. V., Straathof, M., and Lingen, J. V., 2017, "Developments in Additive Manufacturing of Energetic Materials at TNO," 30th Int. Symp. Ballist., **0**(0).

[6] Sohn, H. Y., and Moreland, C., 1968, "The Effect of Particle Size Distribution on Packing Density," Can. J. Chem. Eng., **46**(3), pp. 162–167.

[7] Conway, J. H., and Sloane, N. J. A., 1999, *Sphere Packings, Lattices and Groups*, Springer New York, New York, NY.

[8] Scott, G. D., and Kilgour, D. M., 1969, "The Density of Random Close Packing of Spheres," J. Phys. Appl. Phys., **2**(6), pp. 863–866.

[9] Song, C., Wang, P., and Makse, H. A., 2008, "A Phase Diagram for Jammed Matter," Nature, **453**(7195), pp. 629–632.

[10] Westman, A. E. R., and Hugill, H. R., 1930, "The Packing of Particles," J. Am. Ceram. Soc., **13**(10), pp. 767–779.

[11] Chan, K. W., and Kwan, A. K. H., 2014, "Evaluation of Particle Packing Models by Comparing with Published Test Results," Particuology, **16**, pp. 108–115.

[12] John Milne, S., Patel, M., and Dickinson, E., 1993, "Experimental Studies of Particle Packing and Sintering Behaviour of Monosize and Bimodal Spherical Silica Powders," J. Eur. Ceram. Soc., **11**(1), pp. 1–7.

[13] Farr, R. S., and Groot, R. D., 2009, "Close Packing Density of Polydisperse Hard Spheres," J. Chem. Phys., **131**(24), p. 244104.

[14] Zheng, J., Carlson, W. B., and Reed, J. S., 1995, "The Packing Density of Binary Powder Mixtures," J. Eur. Ceram. Soc., **15**(5), pp. 479–483.

[15] Zok, F., Lange, F. F., and Porter, J. R., 1991, "Packing Density of Composite Powder Mixtures," J. Am. Ceram. Soc., **74**(8), pp. 1880–1885.

[16] Niendorf, K., and Raeymaekers, B., 2020, "Quantifying Macro- and Microscale Alignment of Carbon Microfibers in Polymer-Matrix Composite Materials Fabricated Using Ultrasound Directed Self-Assembly and 3D-Printing," Compos. Part Appl. Sci. Manuf., **129**, p. 105713.

[17] Scholz, M.-S., Drinkwater, B. W., and Trask, R. S., 2014, "Ultrasonic Assembly of Anisotropic Short Fibre Reinforced Composites," Ultrasonics, **54**(4), pp. 1015–1019.

[18] Kinsler, L. E., Kinsler, L. E., Frey, A. R., Coppens, A. B., and Sanders, J. V., 2000, *Fundamentals of Acoustics*, Wiley.

[19] Silva, G. T., and Bruus, H., 2014, "Acoustic Interaction Forces between Small Particles in an Ideal Fluid," Phys. Rev. E, **90**(6), p. 063007.

[20] Settnes, M., and Bruus, H., 2012, “Forces Acting on a Small Particle in an Acoustical Field in a Viscous Fluid,” Phys. Rev. E - Stat. Nonlinear Soft Matter Phys., **85**(1), pp. 1–12.
[21] Chen, X., and Apfel, R. E., 1996, “Radiation Force on a Spherical Object in an Axisymmetric Wave Field and Its Application to the Calibration of High-frequency Transducers,” J. Acoust. Soc. Am., **99**(2), pp. 713–724.
[22] “DLMF: §10.49 Explicit Formulas ‣ Spherical Bessel Functions ‣ Chapter 10 Bessel Functions” [Online]. Available: https://dlmf.nist.gov/10.49. [Accessed: 12-Dec-2022].
[23] Doinikov, A. A., 1997, “Acoustic Radiation Force on a Spherical Particle in a Viscous Heat-Conducting Fluid. II. Force on a Rigid Sphere,” J. Acoust. Soc. Am., **101**(2), pp. 722–730.
[24] Khan, A. R., and Richardson, J. F., 1987, “The Resistance to Motion of a Solid Sphere in a Fluid,” Chem. Eng. Commun., **62**(1–6), pp. 135–150.
[25] Wang, X., Ramírez-Hinestrosa, S., Dobnikar, J., and Frenkel, D., 2020, “The Lennard-Jones Potential: When (Not) to Use It,” Phys. Chem. Chem. Phys., **22**(19), pp. 10624–10633.
[26] Haynes, W. M., Lide, D. R., and Bruno, T. J., 2014, *CRC Handbook of Chemistry and Physics*, CRC Press, Boca Raton.
[27] Underwood, E. E., 1969, “Stereology, or the Quantitative Evaluation of Microstructures,” J. Microsc., **89**(2), pp. 161–180.
[28] St. Clair, N., Davenport, D., Kim, A. D., and Kleckner, D., 2023, “Dynamics of Acoustically Bound Particles,” Phys. Rev. Res., **5**(1), p. 013051.
[29] Pavlic, A., Ermanni, L., and Dual, J., 2022, “Interparticle Attraction along the Direction of the Pressure Gradient in an Acoustic Standing Wave,” Phys. Rev. E, **105**(5), p. L053101.

CHAPTER 4

MEASURING AND SIMULATING THE TRANSIENT PACKING DENSITY DURING ULTRASOUND DIRECTED SELF-ASSEMBLY AND VAT POLYMERIZATION MANUFACTURING OF ENGINEERED MATERIALS

Adapted with permission from Noparast, S., Guevara Vasquez, F., Francoeur, M., and Raeymaekers, B., 2024, "Measuring and simulating the transient packing density during ultrasound directed self-assembly and vat polymerization manufacturing of engineered materials," Adv. Mater. Technol., p. 2301950.

4.1. Introduction

During ultrasound DSA, the concentration of particles in the fluid medium changes as a function of time and location [1] and, specifically, the local particle packing density increases with time at the locations where particles assemble, as particles agglomerate there. Our group has previously quantified the effect of particle volume fraction, particle size, and fluid medium viscosity on the locations where particles assemble [2] and the steady-state local particle packing density at these locations [3].

However, the transient phenomena that govern the time-dependent motion of particles from their initial dispersed state to their final organized steady-state locations are currently not well-understood. Yet, this knowledge is important to advance engineering applications that rely on ultrasound DSA for the manipulation of particles, such as levitated displays and manipulation of cells or particles in biomedical devices. Furthermore, in the context of manufacturing engineered composite materials with ultrasound DSA and VP, it is paramount to understand the transient phenomena during the ultrasound DSA process, because the layer-by-layer VP process requires that particles reach their steady-state locations before a new layer can be cured.

Few researchers have investigated transient phenomena in ultrasound DSA. Specifically, theoretical and experimental studies document the movement of a single spherical particle in a fluid medium during ultrasound DSA in 1D [4,5], 2D [6–8], and 3D [9]. These studies demonstrate that ultrasound frequency, longitudinal wave propagation velocity, particle radius, and fluid medium viscosity significantly affect the transient motion of a single spherical particle during ultrasound DSA. In addition, Scholz et al. [7] experimentally studied the transient motion of multiple glass particles dispersed in water during ultrasound DSA, and reported different transient phenomena for ultrasound DSA of multiple spherical particles.

Importantly, no experimentally validated theoretical model exists that describes the transient phenomena of spherical particles dispersed in a viscous fluid medium during ultrasound DSA. However, quantifying the transient local particle packing density as a function of material properties and ultrasound DSA process parameters is essential in the context of using ultrasound DSA in, e.g. manufacturing of engineered composite materials with ultrasound DSA and VP, among other applications. Hence, we theoretically derive and experimentally validate a 3D ultrasound DSA model to simulate the trajectories and interactions of spherical particles dispersed in a viscous fluid medium, as they organize into their steady-state locations. Using this 3D model, we simulate the transient local particle packing density and packing rate at locations where particles assemble as a function of the ultrasound DSA process parameters.

4.2. Methods and materials

4.2.1. Theoretical model

Figure 4.1 illustrates the theoretical model we implement to simulate the trajectory of many spherical particles dispersed in a viscous fluid medium during ultrasound DSA, as a function of time t, particle volume fraction Φ, particle size a, and fluid medium viscosity η_m. Figure 4.1 (a) schematically shows a reservoir that contains a mixture of a viscous fluid medium and spherical particles. Two ultrasound transducers attached to opposing walls of the reservoir (orange walls in Fig. 4.1 (a)) establish a standing ultrasound wave field. We simulate the time-averaged acoustic radiation potential U inside the solution domain (see contour lines in color ranging from blue (minima) to yellow (maxima)) using the boundary element method (BEM) based on the Helmholtz equation $\nabla^2\varphi_{inc} + \tilde{k}^2\varphi_{inc} = 0$ and Green's third identity. These equations relate the incident ultrasound velocity potential φ_{inc} within the simply-closed boundary of the solution domain to the

impedance boundary condition, and accounts for the absorption and reflection of the ultrasound wave field at the boundary of the *solution domain*. $\tilde{k}$ is the complex wave number that accounts for acoustic attenuation in the viscous fluid medium [3].

Figure 4.1 (b) shows the forces that act on a spherical particle with radius a in a viscous fluid medium within the standing ultrasound wave field, superimposed on the time-averaged acoustic radiation potential U (see contour lines with same color scale as in Fig. 4.1 (a)). We also identify a node and antinode of the standing ultrasound wave field, separated by a half wavelength λ, and we exaggerate the particle size relative to the wavelength for clarity; in reality, $a << \lambda$. A spherical particle experiences the acoustic radiation force $\mathbf{F}$, which drives the particle to the locations where the time-averaged acoustic radiation potential U is locally minimum and the acoustic radiation force $\mathbf{F} = 0$. Additionally, it is subject to a drag force $\mathbf{F}_d$, which orients in the opposite direction of the particle motion, a gravitational force $\mathbf{F}_g$, and buoyancy force $\mathbf{F}_b$, since the particle is immersed in a viscous fluid medium. We use a repulsive Lennard-Jones-like potential as interaction force $\mathbf{F}_{LJ}$ to model particle-particle and particle-wall interactions within the *simulation domain*, which is a subset of the solution domain in the far field of the ultrasound transducers.

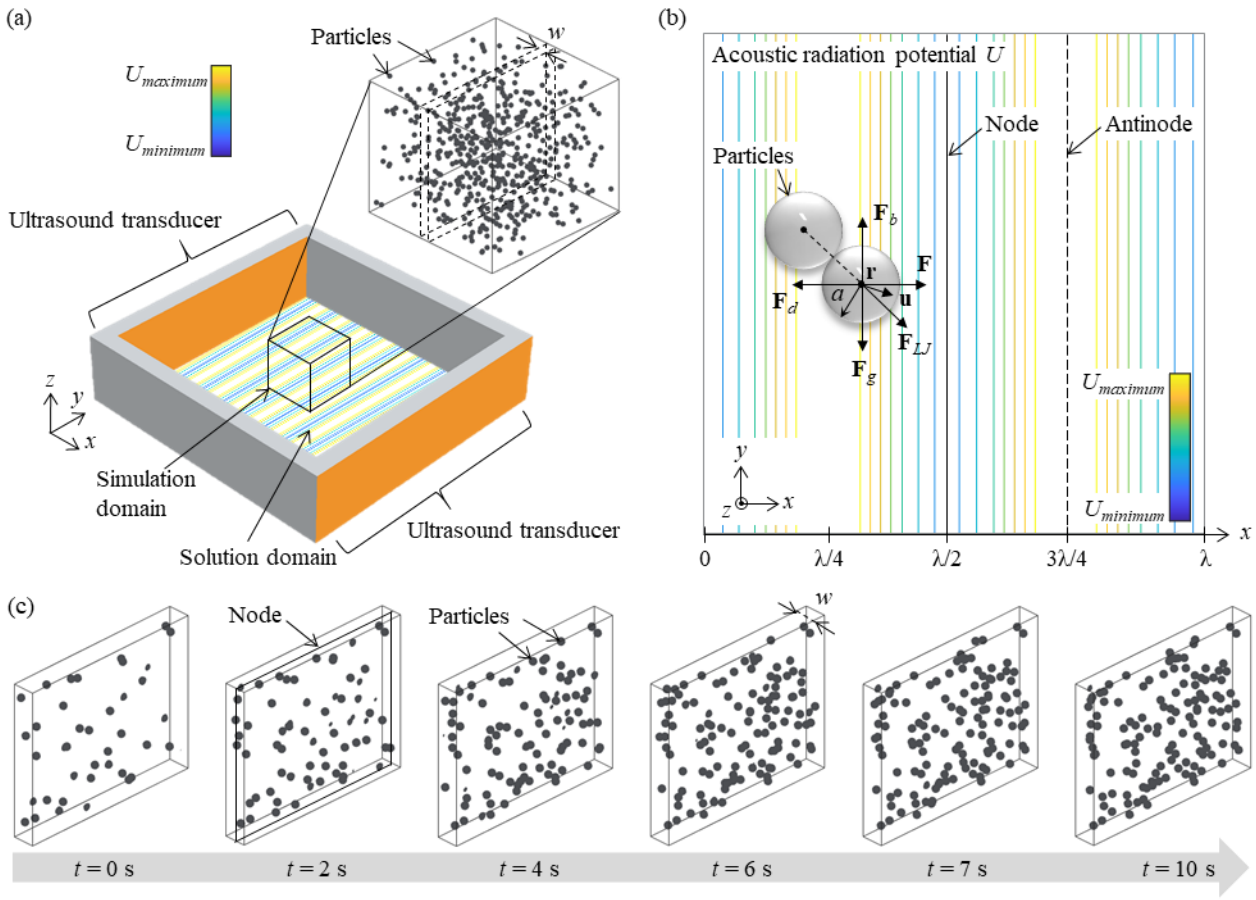

Figure 4.1: (a) Schematic of the 3D ultrasound DSA model, showing a reservoir that contains a mixture of a viscous fluid medium and spherical particles, and with two ultrasound transducers (orange) that establish a standing ultrasound wave field (time-averaged acoustic radiation potential U in color). The reservoir encloses the *solution domain*, but we only simulate the trajectories of the particles within the *simulation domain*, which is a subset of the solution domain in the far field of the ultrasound transducers. (b) Forces that act on a spherical particle in a viscous fluid medium and in a standing ultrasound wave field (time-averaged acoustic radiation potential U in color). The size of the particles is exaggerated for clarity, in reality the particle size a << wavelength λ. (c) Simulated particle assembly in a domain of width w around a node of standing ultrasound wave field as a function of time t during ultrasound DSA.

We define $N \approx 700$ randomly dispersed, non-overlapping particles inside the simulation domain in the center of the solution domain (see Fig. 4.1 (a)), and we uniformly scale the size of the simulation domain to achieve a specific particle volume fraction Φ. The velocity potential φ is the sum of the incident velocity potential φ_{inc}, which we calculate using the BEM, and the velocity potential φ_{sc} that results from single scattering from all other particles in the simulation domain. Thus, the velocity potential φ at the location of i^{th} particle $\mathbf{r}_i$ is [3]

$$\varphi(\mathbf{r}_i) = \varphi_{inc}(\mathbf{r}_i) + \sum_{\substack{j=1 \\ j\neq i}}^{N} \varphi_{sc}(\mathbf{r}_i \mid \mathbf{r}_j), \tag{4.1}$$

where $\varphi_{sc}(\mathbf{r}_i|\mathbf{r}_j)$ is the single monopole and dipole scattering velocity potential of the j^{th} particle at location $\mathbf{r}_j$, measured at the location of i^{th} particle $\mathbf{r}_i$. $\varphi_{sc}(\mathbf{r}_i|\mathbf{r}_j)$ accounts for both monopole and dipole scattering, which depend on the compressibility and density contrast between the particles and the fluid medium, respectively. Dipole scattering also depends on the fluid medium viscosity η_m, and it considers the thickness of the viscous boundary layer around a particle $\delta = (2\eta_m/\omega\rho_m)^{1/2}$, where $\omega = 2\pi f$ and f are the angular and temporal ultrasound wave frequencies, respectively, and ρ_m is the density of the fluid medium. We refer to Noparast et al. [3] for a detailed derivation of $\varphi_{sc}(\mathbf{r}_i|\mathbf{r}_j)$.

The ultrasound wave velocity $v = \nabla\varphi$ is the gradient of the ultrasound velocity potential φ. The ultrasound wave pressure $p = i\rho_m\omega\varphi$, with $i = (-1)^{1/2}$. The time-averaged acoustic radiation potential U in a viscous fluid medium is given as [10]

$$U = \frac{4\pi}{3}a^3\left(f_1\frac{\beta_m}{2}\left\langle p^2\right\rangle - f_2\frac{3\rho_m}{4}\left\langle v^2\right\rangle\right), \tag{4.2}$$

where $f_1 = 1-\beta_p/\beta_m$ and $f_2 = \Re\{[2(1-\gamma)(\rho_p/\rho_m-1)]/[2\rho_p/\rho_m+1-3\gamma]\}$, with $\gamma = -3/2[1+i(1+\delta/a)]\delta/a$. The compressibility of the spherical particle $\beta_p = 1/[\rho_p(c_{p,c}^2-4c_{p,s}^2/3)]$, and the compressibility of the fluid medium $\beta_m = 1/(\rho_m c_m^2)$, with ρ_p the density of the particle, and $c_{p,c}$ (respectively $c_{p,s}$) the propagation velocity of the longitudinal (respectively shear) wave in the particle [11]. Operators $\langle\bullet\rangle$ and $\Re\{\bullet\}$ calculate the time average over one ultrasound wave period and the real part of an expression, respectively. The acoustic radiation force $\mathbf{F} = -\nabla U$ is the negative gradient of the time-averaged acoustic radiation potential U.

The drag force $\mathbf{F}_d$ on each particle inside the simulation domain orients in the opposite direction of the particle velocity $\mathbf{u}$ (see Fig. 4.1 (b)), with $\|\mathbf{F}_d\| = 12\pi a^2 \rho_m ||\boldsymbol{u}||^2(1+3/16Re)/Re$ using Stokes drag force with Oseen's correction. The Reynolds number $Re = 2a\rho_m||\boldsymbol{u}||/\eta_m$ [12].

The interaction force $\mathbf{F}_{LJ} = -\nabla V_{LJ}$ between pairs of particles [13] derives from a repulsive Lennard-Jones-like potential $V_{LJ} = 4\varepsilon_{LJ}(2a/r)^{12}$, and accounts for particle-particle and particle-wall interactions within the simulation domain. We iteratively tune ε_{LJ} to prevent particles from occupying the same space when organized in specific locations, by ensuring that the average distance between two contacting particles is $2a$ (+/-2%), or a (+/-2%) for contact between a particle and a wall. We describe the iterative tuning procedure of ε_{LJ} in the Appendix, but note that for the range of particle volume fractions used in this chapter, ε_{LJ} has limited influence on the results of the transient ultrasound DSA model.

The simulation of the ultrasound DSA process works as follows. First, we calculate the incident velocity potential φ_{inc} within the solution domain using the BEM based on the Helmholtz equation with complex wave number $\tilde{k}$ to account for the attenuation of the ultrasound wave in a viscous fluid medium. Second, we calculate the velocity potential φ at the location of each particle as the superposition of the incident velocity potential φ_{inc} and scattering velocity potential φ_{sc} of all other particles in the simulation domain (Eq. (1)). Then, we calculate the time-averaged acoustic radiation potential U, and the corresponding acoustic radiation force $\mathbf{F}$ that acts on each particle in the simulation domain.

We calculate the trajectory of each spherical particle inside the simulation domain during the transient ultrasound DSA process as a function of time $0 \le t \le T$, with time step $\Delta t = T/3000$. We use a variable time step $\Delta t = T/3000$ to keep the average distance that particles travel in a single time step sufficiently short to avoid that particles overlap and occupy the same space. At $t = 0$,

particles are stationary $\|\mathbf{u}\| = 0$, and at $t = T$, particles have reached their steady-state locations at the nodes of the standing ultrasound wave. However, when $t > 0$ they accelerate as a result of the forces acting on them, and they displace towards the closest local minimum of the time-averaged acoustic radiation potential U (blue contour lines in Fig. 4.1 (a) and (b)). Thus, we determine the location $\mathbf{r}$ and velocity $\mathbf{u}$ of each particle for each time step Δt, accounting for all forces that act on the particle (see Fig. 4.1 (b)) by integrating twice in time the acceleration of each particle.

Furthermore, we calculate the 3D local particle packing density PD_{sim}, for each time step Δt, as the fraction of a cuboid domain of width w around a local minimum of the time-averaged acoustic radiation potential U (where particles assemble) occupied by spherical particles. Figure 4.1 (c) depicts the domain of width w (black solid box) around a node of the standing ultrasound wave field with particles (gray spheres) that assemble inside the domain, visualized for six different time instances t, starting from $t = 0$ s when particles are randomly dispersed in the simulation domain, until $t = 10$ s when particles and PD_{sim} reach steady-state. We choose the width of the domain w to be proportional to the particle radius a (see Section 4.2.2), and compare it later in Fig. 4.8 to choosing w constant and independent of a.

We perform a nondimensional parameter study to quantify the 3D local particle packing density PD_{sim} as a function of ultrasound DSA process parameters, including time t, particle volume fraction Φ, particle size a, and fluid medium viscosity η_m. Using the Buckingham π theorem, we determine that at least four nondimensional parameters are required to describe this system (see Table 4.1); (i) the nondimensional particle size $0.05 \leq K_1 = ka \leq 0.20$, which we select to satisfy the Rayleigh regime assumption ($ka << 1$) where $k = \omega/c_m$ is the real wave number, (ii) the nondimensional fluid medium viscosity $0.07 \leq K_2 = \eta_m/\rho_m \lambda c_m \leq 0.27$, which we define to span the viscosity range of commercial photopolymer resins $100 \leq \eta_m \leq 400$ mPa·s, where $\lambda = c_m/f$, (iii)

the nondimensional time $0 \leq K_3 = ft \leq 150$, which captures the entire transient time-span from initial dispersion to steady-state, for all combinations of parameters, and (iv) the particle volume fraction $0.5 \leq \Phi \leq 22.5\%$, which we select to achieve maximum local particle packing density during steady-state. We note that the units of the fluid medium viscosity η_m in K_2 and the temporal ultrasound frequency f in K_3 are mPa·s and MHz, respectively. The parameter study quantifies the transient local particle packing density PD_{sim} as a function of K_1, K_2, K_3, Φ. To characterize the transient local particle packing density PD_{sim}, we define two additional nondimensional parameters: the nondimensional packing time K_3^*, which is the nondimensional time K_3 when local particle packing density reaches 90% of its steady-state value, and nondimensional packing rate $\delta PD_{sim}/\delta K_3$, which is the nondimensional rate at which transient local particle packing density PD_{sim} changes from 20% to 80% of its steady-state value.

Table 4.1: Nondimensional ultrasound DSA process parameters.

Nondimensional parameter	Definition	Range	Notes
Particle size, K_1	$K_1 = ka$	$0.05 \leq K_1 \leq 0.20$	Satisfies the Rayleigh regime assumption ($ka << 1$).
Fluid medium viscosity, K_2	$K_2 = \eta_m/\rho_m\lambda c_m$	$0.07 \leq K_2 \leq 0.27$	Spans the viscosity range of commercial photopolymer resins $100 \leq \eta_m \leq 400$ mPa·s.
Time, K_3	$K_3 = ft$	$0 \leq K_3 \leq 150$	Covers the entire time-span from initial dispersion to steady-state, for all combinations of parameters.
Particle volume fraction, Φ	Particle volume/control volume	$0.5 \leq \Phi \leq 22.5\%$	Achieves maximum local particle packing density during steady-state.

4.2.2. Experimental validation

Figure 4.2 schematically shows the experimental setup, which integrates a 30 x 30 mm acrylic reservoir with two ultrasound transducers (PZT-4, center frequency f_c = 1.5 MHz, piezoelectric strain constant $d_{33} = 285\times10^{-12}$ [14], Steminc, FL, USA) in a VP digital light

processing (DLP) printer (mUVe 1.1 DLP, Grand Rapids, MI, USA). We use photopolymer resin (3DRS standard V2 gray resin, 3D Resin Solutions, IL, USA) and photopolymer resin diluted with 5 weight percent of isopropyl alcohol, in combination with spherical aluminum microparticles (a = 15 μm and 22 μm, US5005 solid aluminum spherical powder, US Research Nanomaterials Inc., TX, USA). Table 4.2 summarizes the material properties of the particles and the fluid medium. We determine the longitudinal wave propagation velocity of the fluid medium using a pulse-echo time-of-flight measurement [15], and the fluid medium viscosity using a rheometer (Discovery HR 30, TA Instruments, New Castle, DE, USA).

We choose the range of particle volume fraction Φ, particle size a, fluid medium viscosity η_m, and time t based on considerations of practical feasibility of the experiments. We select $0.50 \leq \Phi \leq 1.50\%$ because increasing Φ increases attenuation of the ultrasound wave due to scattering, and it also increases the effective viscosity, which decreases the acoustic radiation force $\|\mathbf{F}\|$ and increases the drag force $\|\mathbf{F}_d\|$ on the particles. Consequently, it reduces the ability to organize particles in the viscous fluid medium. The curing time of the photopolymer resin also increases with increasing Φ [16], which could distort the organization of the particles. We choose particle sizes a = 15 and 22 μm (K_1 = 0.10 and 0.15) to satisfy the Rayleigh regime assumption ($K_1 = ka << 1$). Additionally, the particles are small enough to not precipitate to the floor of the reservoir, yet they are large enough to be observed under an optical microscope. The fluid medium viscosity η_m = 126 and 218 mPa.s (K_2 = 0.09 and 0.15) matches the viscosity of typical commercial photopolymer resins. Finally, we define time $0 \leq t \leq 30$ s ($0 \leq K_3 \leq 45$) to ensure capturing the entire transient behavior of the local particle packing density PD_{exp} during ultrasound DSA, using all combinations of Φ, K_1, and K_2.

We disperse a volume fraction Φ particles in the viscous fluid medium using a magnetic stirrer, and energize the ultrasound transducers with a function generator (Tektronix AFG 3102, Beaverton, OR, USA) and a radio frequency (RF) power amplifier (E&I 2100L, Rochester, NY, USA) to organize the particles into line patterns that correspond to the nodes of the standing ultrasound wave field between both ultrasound transducers. The input peak-to-peak voltage of the ultrasound transducers $V_{p\text{-}p}$ = 21 V. This translates to a velocity amplitude of the ultrasound transducer surface of $|v| = 2.8\times10^{-2}$ m/s, based on the piezoelectric strain constant of the ultrasound transducers, which we require as a boundary condition in the simulations with the BEM method (see Section 4.2.1). After ultrasound DSA, we cure a single layer 12 x 12 mm composite material specimen with a 12 s exposure time, and a 120 s post-cure time outside the VP setup to eliminate any liquid photopolymer. Figure 4.2 shows a typical composite material specimen after curing and post-curing (Φ = 1.00 %, K_1 = 0.10, K_2 = 0.09, and K_3 = 15).

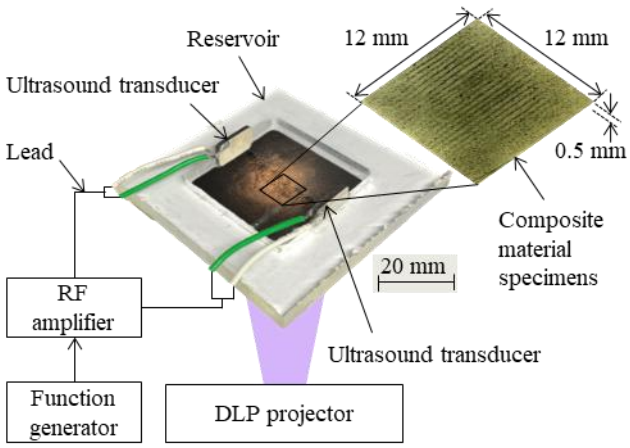

Figure 4.2: Schematic of the experimental setup, which integrates an acrylic reservoir with two ultrasound transducers in a VP digital light processing (DLP) printer. The reservoir contains a mixture of photopolymer and aluminum microparticles, and a function generator and RF amplifier drive the ultrasound transducers to organize the particles into a line pattern that corresponds to the nodes of the standing ultrasound wave field between both ultrasound transducers. Exposure to UV light cures a square single layer composite material specimen.

Table 4.2: Material properties of the particles and viscous fluid media.

Material	Density, ρ [kg/m^3]	Longitudinal wave propagation velocity, c [m/s]	Shear wave propagation velocity, c [m/s]	Viscosity, η_m [mPa·s]
Spherical aluminum microparticles	2,710 [17]	$c_{c,p}$ = 6,420 [17]	$c_{s,p}$ = 3,040 [17]	-
Standard photopolymer resin	1,100	c_m = 1,420	-	218
Diluted standard photopolymer resin	1,079	c_m = 1,409	-	126

To perform a full-factorial study of the local particle packing density PD_{exp} as a function of Φ, K_1, K_2, and K_3, we manufacture 72 composite material specimens (3 (Φ) x 2 (K_1) x 2 (K_2) x 6 (K_3)) using the experimental setup of Fig. 4.2. Additionally, we perform three repeat measurements of each combination of parameters, for a total of 216 composite material specimens.

We experimentally measure the local particle packing density PD_{exp} as the area fraction of a rectangular domain of width w around the location where particles assemble, occupied by the particles. The fraction of an area covered by particles approximates the volumetric particle packing density, as first suggested by Delesse in 1848 [18] and later theoretically and experimentally demonstrated by Underwood [19] and Weibel [18,20]. We also verified the accuracy of this approximation using the 3D theoretical model, and determined a 4% maximum error for Φ = 1.5%.

Figure 4.3 illustrates the measurement methodology, showing optical micrographs (1.5 μm spatial resolution, 180X magnification, AmScope, CA, USA) with the corresponding binary images as a function of time t (K_3) for Φ = 1.00 %, K_1 = 0.10, and K_2 = 0.09, of locations where we qualitatively detect organization of the spherical aluminum microparticles. We focus the optical microscope on the top surface of the composite material specimen to only capture particles (silver) on the surface (green), and not in the bulk of the specimen. We binarize the optical micrographs using a threshold that equates the particle area fraction of the entire field-of-view to the particle volume fraction Φ dispersed in the photopolymer. This minimizes the effect of external influences,

such as lighting conditions and glare, on the binarization of the image. We measure the particle area fraction as the number of black pixels within a domain $w = Ma$ centered around a location where particles assemble divided by the total number of pixels within the domain (see Fig. 4.3). We select $M = 6$, i.e., $w = 6a$ to enclose most particles that assemble at the node of a standing ultrasound wave field, based on experiments with $\Phi = 1.00$ %, $K_1 = 0.10$, and $K_2 = 0.09$. We repeat each measurement three times for composite material specimens and report the average, minimum, and maximum values of the local particle packing density PD_{exp}.

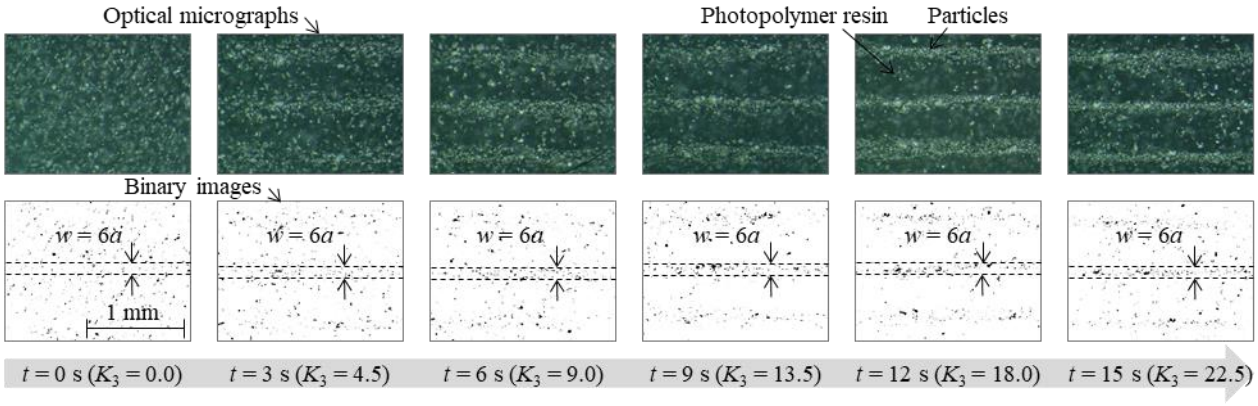

Figure 4.3: Methodology to measure the local particle packing density PD_{exp}, showing optical micrographs with corresponding binary images as a function of time t for $\Phi = 1.00$ %, $K_1 = 0.10$, and $K_2 = 0.09$, covering domain $w = 6a$.

4.3. Results and discussion

4.3.1. Experimental validation

Figure 4.4 shows the simulated PD_{sim} (lines) and experimental PD_{exp} (solid markers) local particle packing density as a function of the nondimensional time K_3, for three particle volume fractions $\Phi = 0.5$, 1.0, 1.5 %, and for (a) $K_1 = 0.10$ and $K_2 = 0.09$, (b) $K_1 = 0.15$ and $K_2 = 0.09$, (c) $K_1 = 0.10$ and $K_2 = 0.15$, (d) $K_1 = 0.15$ and $K_2 = 0.15$, i.e., the rows and columns represent constant K_2 and K_1, respectively. The solid markers represent the average of three measurements, and the error bars show the minimum and maximum. Figure 4.4 illustrates excellent agreement between

the theoretical simulations and experimental results, and we determine a maximum $|PD_{exp} - PD_{sim}|$ = 0.9% error for Φ = 1.5 %, K_1 = 0.05, K_2 = 0.15, and K_3 = 22.5. Additionally, Fig. 4.5 shows optical micrographs (green = resin, silver = particles) and the corresponding binary images (white = resin, black = particles) of the composite material specimens as a function of nondimensional time K_3 for selected data points of Fig. 4.4.

We observe from Fig. 4.4 and Fig. 4.5 that the local particle packing density at locations where particles assemble increases with increasing nondimensional time K_3, because the number of particles that assemble at a specific location increases. The local particle packing density reaches steady-state when almost all particles have assembled into the specific location, and no additional particles are available to assemble at that location. Furthermore, the local particle packing density increases with increasing particle volume fraction Φ because the number of particles dispersed in the photopolymer resin increases, which the comparison of Fig. 4.5 (a) and (b) illustrates. Figure 4.4 (a) and (b), and (c) and (d) show that increasing the nondimensional particle size K_1 decreases the local particle packing density for constant particle volume fraction Φ, because the number of particles to obtain a specific Φ decreases with increasing K_1, which is evident from the comparison of Fig. 4.5 (a) and (c). Figure 4.4 (a) and (c), and (b) and (d), show that increasing the nondimensional fluid medium viscosity K_2 decreases the transient local particle packing density for constant particle volume fraction Φ because increasing the fluid medium viscosity increases the drag force on the particles $||\mathbf{F}_d||$ and decreases their velocity $||\mathbf{u}||$, which delays their assembly at specific locations. However, the steady-state local particle packing density remains unaffected by changing the fluid medium viscosity, because it only depends on the number of particles dispersed in the fluid medium. Figure 4.5 (a) and (d) illustrate the effect of increasing the nondimensional fluid medium viscosity K_2.

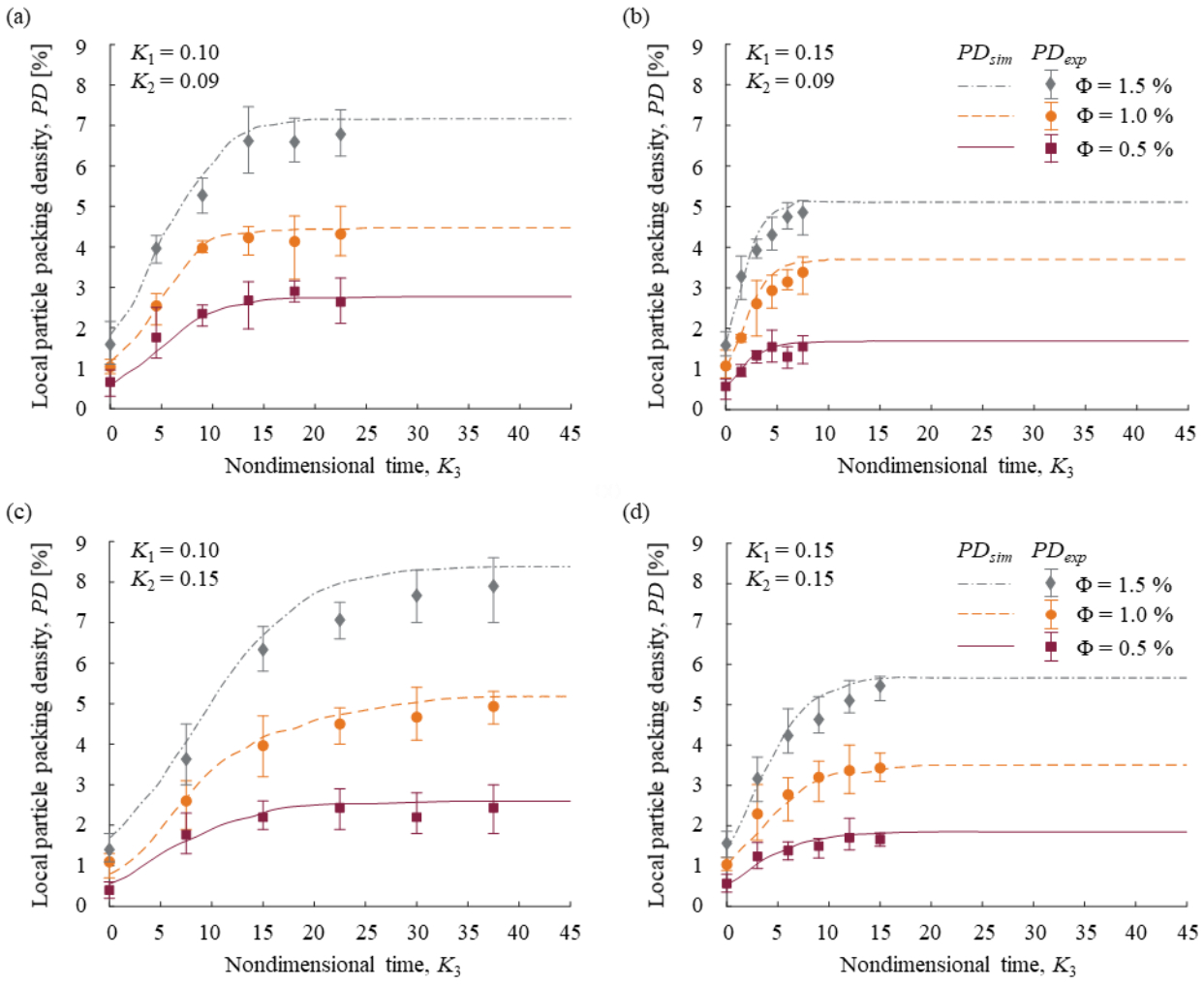

Figure 4.4: Transient and steady-state local particle packing density within the pattern features that result from ultrasound DSA (node of the standing ultrasound wave field) as a function of nondimensional time K_3, showing simulation PD_{sim} (lines) and experiment PD_{exp} (solid markers) results for particle volume fraction $\Phi = 0.5$ % (solid maroon line and maroon square), $\Phi = 1.0$ % (dashed orange line and orange circle), and $\Phi = 1.5$ % (dash-dot gray line and gray diamond), and for (a) $K_1 = 0.10$ and $K_2 = 0.09$ (b) $K_1 = 0.15$ and $K_2 = 0.09$, (c) $K_1 = 0.10$ and $K_2 = 0.15$, (d) $K_1 = 0.15$ and $K_2 = 0.15$.

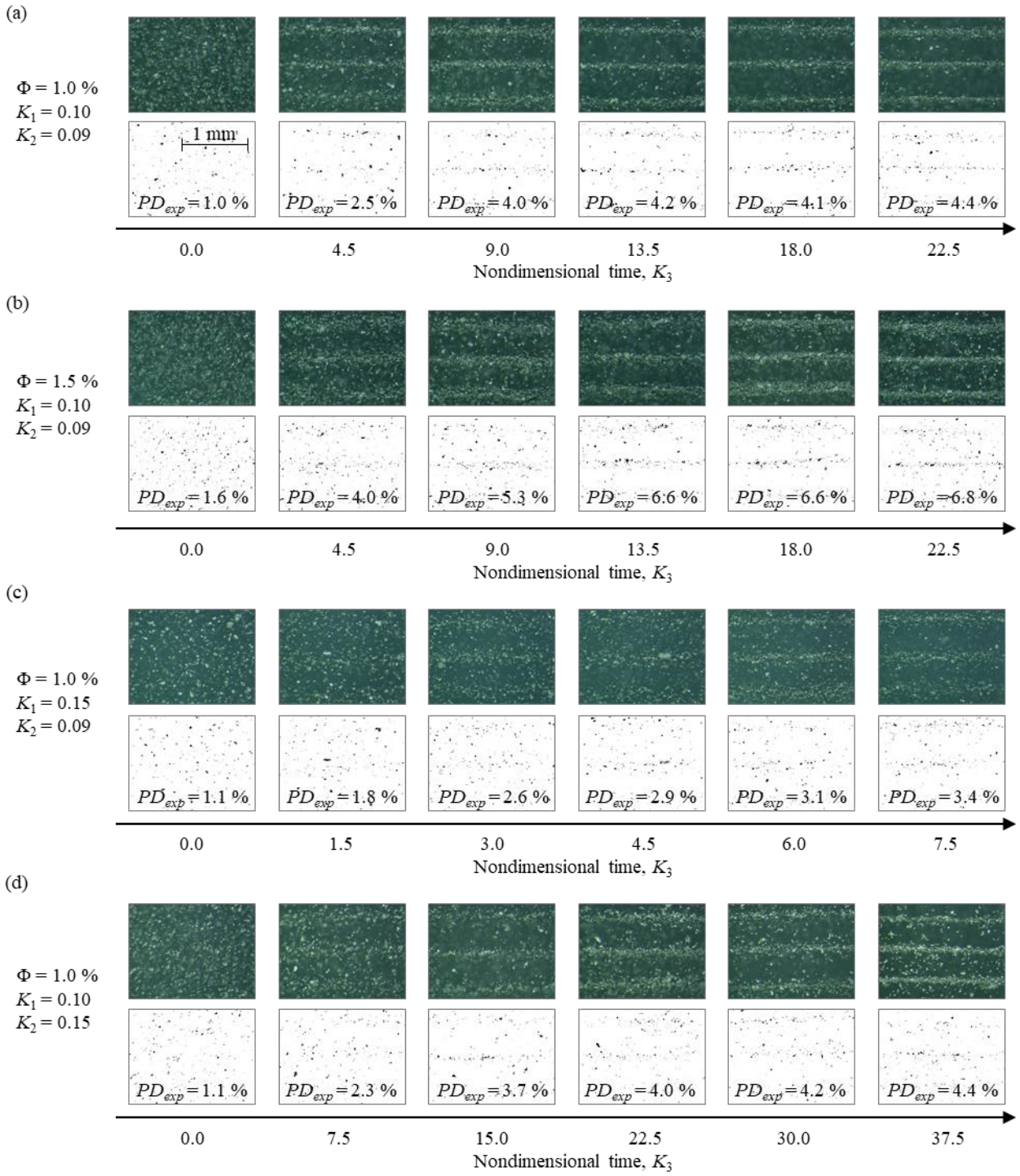

Figure 4.5: Optical micrographs (green = resin, silver = particles) and binary images (white = resin, black = particles) of composite material specimens for selected data points of Fig. 4.4: (a) Φ = 1.0 %, K_1 = 0.10, and K_2 = 0.09, (b) Φ = 1.5 %, K_1 = 0.10, and K_2 = 0.09, (c) Φ = 1.0 %, K_1 = 0.15, and K_2 = 0.09, and (d) Φ = 1.0 %, K_1 = 0.10, and K_2 = 0.15.

4.3.2. Simulation results and parameter study

We also use the 3D theoretical model to illustrate the effect of particle volume fraction Φ, nondimensional particle size K_1, nondimensional fluid medium viscosity K_2, and nondimensional time K_3 on the transient local particle packing density PD_{sim} during ultrasound DSA, covering the entire ultrasound DSA process envelope, i.e., beyond the parameter ranges we have experimentally validated. Figure 4.6 shows the transient local particle packing density PD_{sim} at the location where particles assemble (node of the standing ultrasound wave field) as a function of the nondimensional time K_3 for different particle volume fractions $0.5 \leq \Phi \leq 22.5$ % (Fig. 4.6 (a)), different nondimensional particle sizes $0.05 \leq K_1 \leq 0.20$ (Fig. 4.6 (b)), and different nondimensional fluid medium viscosities $0.07 \leq K_2 \leq 0.27$ (Fig. 4.6 (c)). In addition, Fig. 4.6 shows the nondimensional packing time K_3^* (hollow circles), i.e., the time at which the local particle packing density reaches 90% of its steady-state value. The nondimensional packing time is important, e.g. in the context of VP, where one must be aware of the time required for particles to assemble at their steady-state locations, before curing a layer of photopolymer resin. Consequently, K_3^* also determines the speed of the VP process.

From Fig. 4.6, we observe that the transient local particle packing density PD_{sim} increases and ultimately reaches steady-state with increasing nondimensional time K_3, similar to the results of Fig. 4.4 and Fig. 4.5. Figure 4.6 (a) shows that increasing particle volume fraction Φ increases the transient local particle packing density prior to reaching its maximum value $PD_{sim} = 45$ %. This result agrees with the maximum achievable steady-state local particle packing density within the pattern features after ultrasound DSA [3]. Additionally, from Fig. 4.6 (a) we observe that increasing the particle volume fraction Φ first increases ($\Phi \leq 15\%$) and then decreases ($\Phi > 15\%$) the nondimensional packing time K_3^*, which is the result of two phenomena. First, increasing Φ

increases the number of particles in a control volume within the ultrasound DSA reservoir, which increases the number of collisions between particles and also increases the dissipative acoustic interaction forces due to ultrasound wave scattering. Collisions and dissipative acoustic interaction forces decrease the effective particle velocity $||\mathbf{u}||$ with which particles approach the locations where they assemble and, thus, increase K_3^*. However, increasing $\Phi \geq 15\%$ increases the local particle packing density PD_{sim} when particles are initially randomly dispersed at nondimensional time $K_3 = 0$, such that the steady-state PD_{sim} reaches its theoretical maximum value of approximately 45%. Hence, increasing $\Phi \geq 15\%$ decreases the difference between PD_{sim} at $K_3 = 0$ and its steady-state PD_{sim}, which decreases the nondimensional packing time K_3^* because the maximum local particle packing density at the locations where particles assemble is reached before all particles reach their steady-state location. From Fig. 4.6 (b), we observe that increasing nondimensional particle size K_1 decreases the nondimensional packing time K_3^* because increasing K_1 increases the acoustic radiation force $||\mathbf{F}|| \propto a^3$ (Eq. (2)) more than the drag force $||\mathbf{F}_d|| \propto a$ on particles, which increases the velocity $||\mathbf{u}||$ with which they move towards the locations where they assemble and, consequently, decreases the time to reach that location. Figure 4.6 (c) shows that increasing the nondimensional fluid medium viscosity K_2 increases the nondimensional packing time K_3^*, but it does not affect the steady-state local particle packing density PD_{sim}, as expected. Increasing K_2 increases the magnitude of drag force on particles $||\mathbf{F}_d|| \propto a$ and, thus, decreases the velocity $||\mathbf{u}||$ with which particles move towards the locations where they assemble, which increases the time to reach that location.

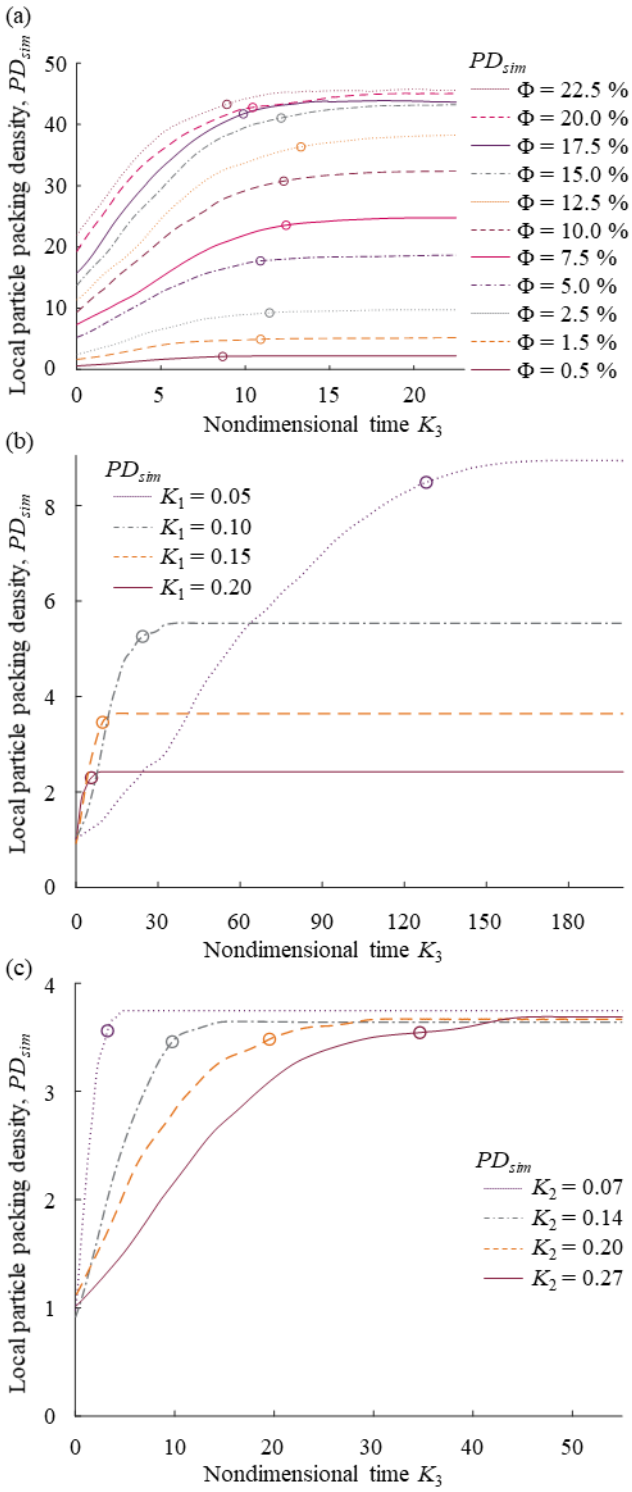

Figure 4.6: Transient local particle packing density PD_{sim} at locations where particles assemble, as a function of nondimensional time K_3, covering the entire ultrasound DSA process envelope, (a) for $K_1 = 0.15$ and $K_2 = 0.14$ and different particle volume fractions $0.5 \leq \Phi \leq 22.5$ %, (b) for $\Phi = 1.0$ % and $K_2 = 0.14$ and different nondimensional particle sizes $0.05 \leq K_1 \leq 0.20$, and (c) for $\Phi = 1.0$ % and $K_1 = 0.15$ and different nondimensional medium viscosities $0.07 \leq K_2 \leq 0.27$, also showing the nondimensional packing time K_3^* (hollow circles) for each transient local particle packing density PD_{sim}.

Using the 3D ultrasound DSA model, we quantify the relationship between nondimensional particle size K_1 and nondimensional fluid medium viscosity K_2, and the nondimensional packing time K_3^* and nondimensional packing rate $\delta PD/\delta K_3$, which both characterize the transient local particle packing density PD_{sim}. Figure 4.7 shows the nondimensional packing time K_3^* and nondimensional packing rate $\delta PD/\delta K_3$ as a function of nondimensional particle size K_1 for different values of the nondimensional fluid medium viscosity $0.07 \leq K_2 \leq 0.27$. We derive power and linear best-fit equations for K_3^* and $\delta PD/\delta K_3$, respectively, to quantify their relationship with the nondimensional ultrasound DSA process parameters K_1 and K_2. These equations provide information, e.g. to tune the VP layer-by-layer curing process, based on the material properties and ultrasound DSA process parameters. From Fig. 4.7, we observe that increasing nondimensional particle size K_1 decreases the nondimensional packing time K_3^* and increases the nondimensional packing rate $\delta PD/\delta K_3$. Increasing nondimensional particle size K_1 requires increasing the particle radius a, which increases the acoustic radiation force on particles $\|\mathbf{F}\| \propto a^3$ (see Eq. (4.2)), increases the velocity $\|\mathbf{u}\|$ with which particles move toward the nodes of standing ultrasound wave field, decreases the time particles require to assemble at the node of standing ultrasound wave field, and thus decrease the nondimensional packing time K_3^*. Also, increasing the velocity $\|\mathbf{u}\|$ with which particles move toward the nodes of the standing ultrasound wave field increases the number of particles that assemble at nodes of the standing ultrasound wave field at each time increment during ultrasound DSA, and, thus, increases the nondimensional packing rate $\delta PD/\delta K_3$.

Additionally, Fig. 4.7 shows that increasing nondimensional fluid medium viscosity K_2 increases the nondimensional packing time K_3^* and decreases the nondimensional packing rate $\delta PD/\delta K_3$. Increasing K_2 increases the magnitude of the drag force on the particles $\|\mathbf{F}_d\| \propto a$ and,

thus, decreases the velocity ||**u**|| with which particles move towards the locations where they assemble, which increases the time to reach that location, increases K_3^*, and decreases $\delta PD/\delta K_3$. We note that Fig. 4.6 and Fig. 4.7 include parameter values that extrapolate beyond those used in the experimental validation and, thus, must be interpreted with caution.

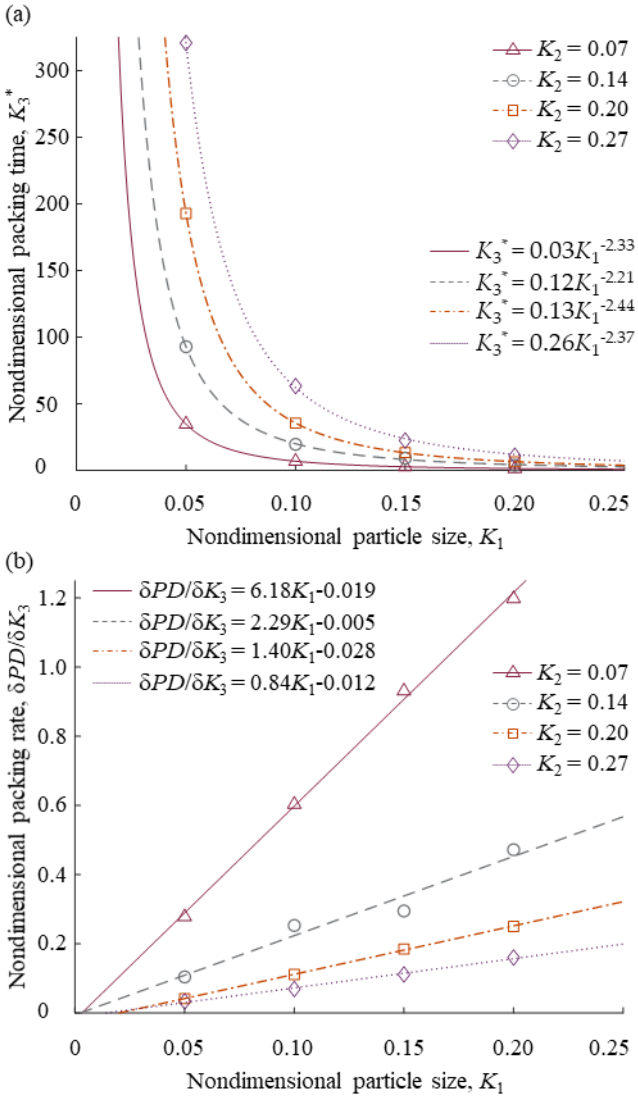

Figure 4.7: (a) Nondimensional packing time K_3^* and (b) nondimensional packing rate $\delta PD/\delta K_3$ as a function of nondimensional particle size K_1 for nondimensional fluid medium viscosity $K_2 = 0.07$ (maroon rectangle), $K_2 = 0.14$ (gray circle), $K_2 = 0.20$ (orange square), and $K_2 = 0.27$ (purple diamond), illustrating (a) power and (b) linear best-fit equations of nondimensional packing time K_3^* and nondimensional packing rate $\delta PD/\delta K_3$ (hollow markers), respectively.

4.3.3. Discussion

The 3D ultrasound DSA model advances existing models through several innovations. First, it is the first model that extends beyond simulating the steady-state locations where particles assemble, which enables quantifying the transient local particle packing density by PD_{sim}, nondimensional packing time K_3^*, and nondimensional packing rate $\delta PD/\delta K_3$ until the particles and the local particle packing density PD_{sim} reach steady-state [2,3]. Second, the model is capable of simultaneously predicting the trajectory of many spherical particles dispersed in a viscous fluid medium during ultrasound DSA, which contrasts existing transient models that theoretically simulate the dynamic behavior of an individual particle in an inviscid medium [1,6–8,21], and existing studies that only experimentally investigate the dynamic behavior of multiple particles in an inviscid medium [7,22]. However, the results of this chapter still agree with previous studies that describe the dynamic behavior of an individual particle in a standing ultrasound wave field, which document the effect of particle size a, fluid medium viscosity η_m, and ultrasound frequency f on the transient behavior of the particle [7]. Third, this model relaxes simplifying assumptions of existing models that consider an inviscid medium [6], neglect the effects of ultrasound wave attenuation and ultrasound wave scattering from neighboring particles [7]. Finally, the model is perhaps the first one to include collisions between particles by means of an LJ-like potential.

The 3D ultrasound DSA model also shows limitations. We define randomly dispersed particles only in a section of the reservoir, i.e., the simulation domain, to manage the computational cost of the simulations. However, this simplification neglects the effect of ultrasound wave scattering by particles outside the simulation domain on the transient local particle packing density PD_{sim}. Thus, the particle packing density at the edges of the simulation domain likely underestimates the true particle packing density. Additionally, one can study the acoustic

interaction between spherical particles in a fluid medium using a single- or multiple scattering. Single scattering considers only one scattering event, whereas multiple scattering considers multiple scattering events of the scattered wave [23]. The 3D ultrasound DSA model only implements single scattering because for the range of particle volume fractions we consider in this chapter, the particles remain far away from each other during the transient portion of the simulation. However, when particles assemble at the nodes of the standing ultrasound wave, multiple scattering would be more appropriate because a particle is surrounded by many other particles and, thus, the scattered wave can reflect off multiple particles. we did not include multiple scattering due to computational cost, and because the literature predicts its effect to be small [23].

Quantifying the transient local particle packing density is not straightforward because the locations where particles assemble is not unambiguously defined. The node of a standing wave theoretically is a line, but in practice, particles assemble and agglomerate at a location of finite width, which necessitates defining a rectangular region of width w around the node to quantify the local particle packing density. Consequently, the transient local particle packing density depends on w, i.e., it increases with decreasing w, as an increasing fraction of the domain is occupied by particles at any given time. We replicate the results of Fig. 4.6 (b) to illustrate the difference between measuring the transient local particle packing density PD_{sim} within a domain width that is a function of the particle radius a, i.e., $w = 6a$, or within a constant domain width w around the node. Figure 4.8 shows the transient local particle packing density PD_{sim} at the location where particles assemble as a function of nondimensional time K_3, for a constant domain width $w = 60$ μm (Fig. 4.8 (a)) and for domain width $w = 6a$ (Fig. 4.8 (b), identical to Fig. 4.6 (b)), for $\Phi = 1.0$ % and $K_2 = 0.14$ and $0.05 \leq K_1 \leq 0.20$. We also show the nondimensional packing time K_3^* (hollow circles). From Fig. 4.8, we observe that increasing nondimensional particle size K_1 decreases the

nondimensional packing time K_3^*, both when w = 60 μm and $w = 6a$. However, the magnitude of this reduction is different between both choices of the domain width. Changing K_1 shows no effect on the steady-state local particle packing density PD_{sim} within the domain of constant width w (Fig. 4.8 (a)), since the volume of the domain and the volume of the particles within the domain remain constant. In contrast, increasing K_1 decreases the steady-state local particle packing density PD_{sim} within the variable domain of width $w = 6a$ (Fig. 4.8 (b)) because the width of the domain increases with the size of the particles, thus adding more empty space.

The experiments also show limitations. We validate the 3D ultrasound DSA model over a limited range of ultrasound DSA process parameters, i.e., particle volume fraction $0.50 \leq \Phi \leq 1.50\%$, particle size a = 15 and 22 μm, and fluid medium viscosity η_m = 126 and 218 mPa.s. Thus, the experimental validation does not cover the entire ultrasound DSA process envelope due to practical limitations of increasing Φ, a, and η_m during the experiments (see Section 4.2.2). In addition, imperfect dispersion of spherical aluminum microparticles in the (diluted) photopolymer resin, imperfect spherical shape and size of the aluminum microparticles, misalignment of the ultrasound transducers on the walls of the acrylic reservoir, and the ultrasound transducers not performing as perfect piston sources, all cause error in the experimental results.

We note that we choose the amplitude of the ultrasound wave in the experiments based on experimental constraints. Increasing the peak-to-peak voltage $V_{p\text{-}p}$ supplied to the ultrasound transducers increases the amplitude of the standing ultrasound wave and, consequently, increases the acoustic radiation force that acts on particles in the reservoir. Thus, increasing $V_{p\text{-}p}$ increases the velocity with which particles move to the nodes of the standing ultrasound wave. However, increasing $V_{p\text{-}p}$ also increases the temperature of the medium, and increases the likelihood of acoustic streaming that distorts the assembly of particles into patterns. Hence, we balance both

effects by selecting $V_{p\text{-}p}$ sufficiently high to organize particles at the nodes of the standing ultrasound wave before they precipitate to the bottom of the reservoir, yet sufficiently low to avoid heating and acoustic steaming that distort the assembly of particles into specific patterns.

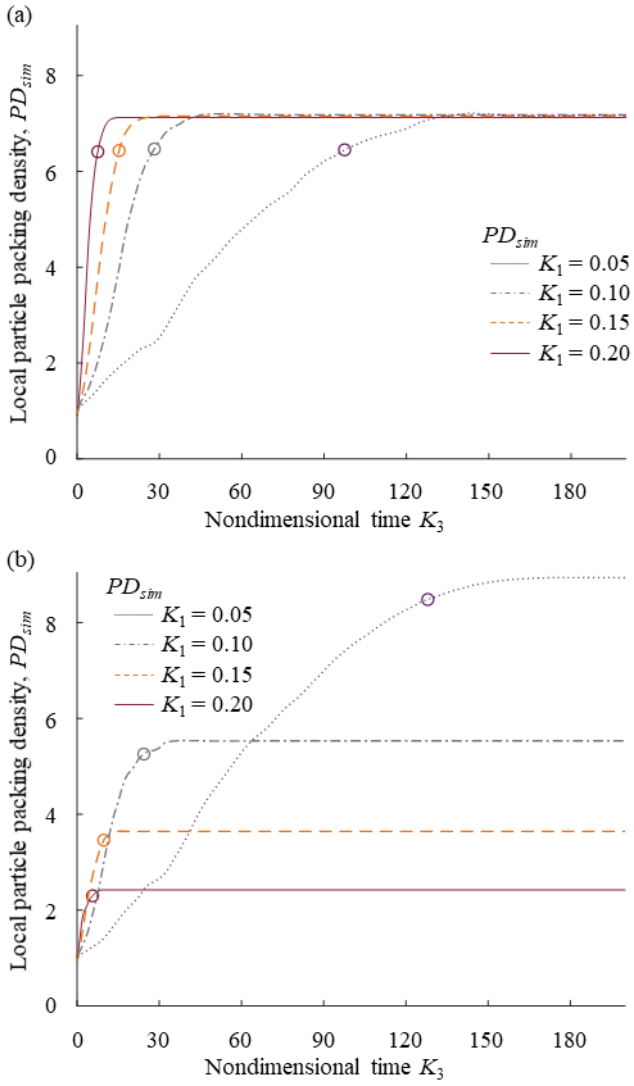

Figure 4.8: Transient local particle packing density PD_{sim} within the pattern features as a function of nondimensional time K_3, using a (a) constant domain of width w = 60 μm and (b) a variable domain of width $w = 6a$, covering the entire ultrasound DSA process envelope, for Φ = 1.0 % and K_2 = 0.14 and different nondimensional particle sizes $0.05 \leq K_1 \leq 0.20$, also illustrating the nondimensional packing time K_3^* (hollow circles) for each transient local particle packing density PD_{sim}.

Finally, we emphasize that even though we manufacture single layer specimens in this chapter, we have previously demonstrated that the integration of ultrasound DSA and VP can

implement multi-layer specimens, by following a two-step curing approach that allows establishing an ultrasound in the photopolymer resin contained in the VP vat [24].

4.4. Conclusions

This chapter presents a 3D model of ultrasound DSA that enables simulating the trajectories of many spherical particles dispersed in a viscous fluid medium, subject to a standing ultrasound wave field, as a function of time and ultrasound DSA process parameters. Such simulations allow quantifying the transient and steady-state local particle packing density at the specific locations where the particles assemble. We demonstrate good agreement between the theoretical model and experiments. We conclude that:

1. The local particle packing density at locations where particles assemble increases with increasing nondimensional time K_3, due to increasing number of particles that assemble at a specific location, then reaches steady-state when almost all particles have assembled into the specific location. Furthermore, the local particle packing density increases with increasing particle volume fraction Φ due to an increasing number of particles dispersed in the photopolymer. It ultimately reaches a steady-state particle packing density that approaches the theoretical random particle packing density for spherical particles of approximately 45%.
2. Increasing the nondimensional particle size K_1 decreases the local particle packing density for constant particle volume fraction Φ, because the number of particles to obtain a specific Φ decreases with increasing K_1. In addition, increasing the nondimensional fluid medium viscosity K_2 decreases the transient local particle packing density for constant particle volume fraction Φ because increasing the fluid

medium viscosity increases the drag force on the particles $\|\mathbf{F}_d\|$ and decreases the velocity $\|\mathbf{u}\|$ with which they approach their steady-state location. However, the steady-state local particle packing density remains unaffected by the nondimensional fluid medium viscosity K_2.

3. Increasing the particle volume fraction Φ first increases and then decreases the nondimensional packing time K_3^* because increasing Φ increases collisions and ultrasound wave scattering between particles that decrease the velocity $\|\mathbf{u}\|$ with which particles move towards locations where they assemble. Increasing $\Phi \geq 15\%$ increases the local particle packing density when particles are initially randomly dispersed in the fluid medium, such that the steady-state local particle packing density reaches its theoretical maximum value of approximately 45%. Hence, K_3^* decreases because the local particle packing density at the locations where particles assemble reaches its maximum value before all particles reach their steady-state location. Increasing the nondimensional particle size K_1 or decreasing nondimensional fluid medium viscosity K_2 both increase the velocity with which particles move towards the locations where they assemble and, thus, decreases K_3^*.

The results of this chapter provide a physical understanding of the transient phenomena that affect the local particle packing density during ultrasound DSA in a viscous fluid medium. This knowledge is relevant to a broad spectrum of engineering applications that involve ultrasound DSA, such as non-contact particle manipulation, lab-on-a-chip applications, acoustic displays, and materials manufacturing. Specifically, with respect to integrating ultrasound DSA and VP to manufacture engineered composite materials, the results of this chapter allow tailoring the layer-by-layer VP process to the ultrasound DSA process parameters, and manufacture composite

materials wherein each layer, ultrasound DSA organizes and orient particles into specific patterns with specific local particle packing density before the VP process cures a new layer.

4.5. Acknowledgements

This research was supported by the National Science Foundation under award CMMI-2130083, DMS-2008610 and DMS-2136198.

4.6. Appendix: Iterative tuning procedure of ε_{LJ} parameter

We consider both particle-particle and particle-wall interactions in the ultrasound DSA simulations, using the LJ-like potentials $V_{LJ,p\text{-}p} = 4\varepsilon_{LJ}(2a/r_{p\text{-}p})^{12}$ and $V_{LJ,p\text{-}w} = 4\varepsilon_{LJ}(a/r_{p\text{-}w})^{12}$, respectively. The parameter ε_{LJ} is the same for particle-particle and particle-wall interactions. $r_{p\text{-}p}$ is the distance between a pair of particles, and $r_{p\text{-}w}$ is the distance between a particle and a simulation domain boundary. Hence, tuning of the LJ-like potential ensures a minimum separation of $2a$ and a between particle-particle and particle-wall, respectively, where a is the radius of a particle. To determine the ε_{LJ} parameter, we perform the following tuning process (see flowchart of Fig. 4.9):

STEP 1: We perform the ultrasound DSA simulation over a duration $0 \leq t \leq T$ with time step Δt and an initial guess of ε_{LJ}, which is based on experience and values that have previously worked. However, we note that the methodology works for any initial guess; it could just require more iterations to reach a converged solution based on the choice of the initial guess. We choose T long enough so the particles assemble at the nodes of the standing ultrasound wave and reach a steady-state local packing density.

STEP 2: After particles assemble at nodes of the standing ultrasound wave, we measure the distance between each particle and its closest neighboring particle d_i where $i = 1, 2, \ldots, M$ (M is the number of particles assembled in a domain $w = 6a$ centered around a node of the standing ultrasound wave.). We calculate the average distance d_{avg} of the 10% smallest distances d_i.

STEP 3: We repeat STEP 2 for the 10 sequential time steps before $t = T$, when the particles have already assembled at the node of the standing ultrasound wave, and the particle packing density remains unchanged. We calculate $d_{avg,j}$ for each time step, with $j = 1, 2, \ldots, 10$. Then, we calculate the average of all $d_{avg,j}$ values as $d_{average}$. Hence, in steps 2 and 3, we average the minimum distance between particles over both space (STEP 2) and time (STEP 3).

STEP 4: We use an automated iterative optimization method by repeating STEPs 1-3, until $d_{average} = 2a$ (+/-2%). Therefore, we tune $\varepsilon_{LJ,new} = \varepsilon_{LJ}(2a/d_{average})^{12}$ in each iteration so particles experience a magnitude of $V_{LJ,p\text{-}p}$ at $r_{p\text{-}p} = 2a$ that equals the magnitude of $V_{LJ,p\text{-}p}$ at $r_{p\text{-}p} = d_{average}$ in the previous iteration. Thus, if $d_{average} > 2a$, we increase the "spring constant" of the LJ-like potential to draw the particles closer, and if $d_{average} < 2a$, we decrease the "spring constant" of the LJ-like potential so that the equilibrium distance between particles increases. We repeat the described iterative optimization method for all simulations in this chapter.

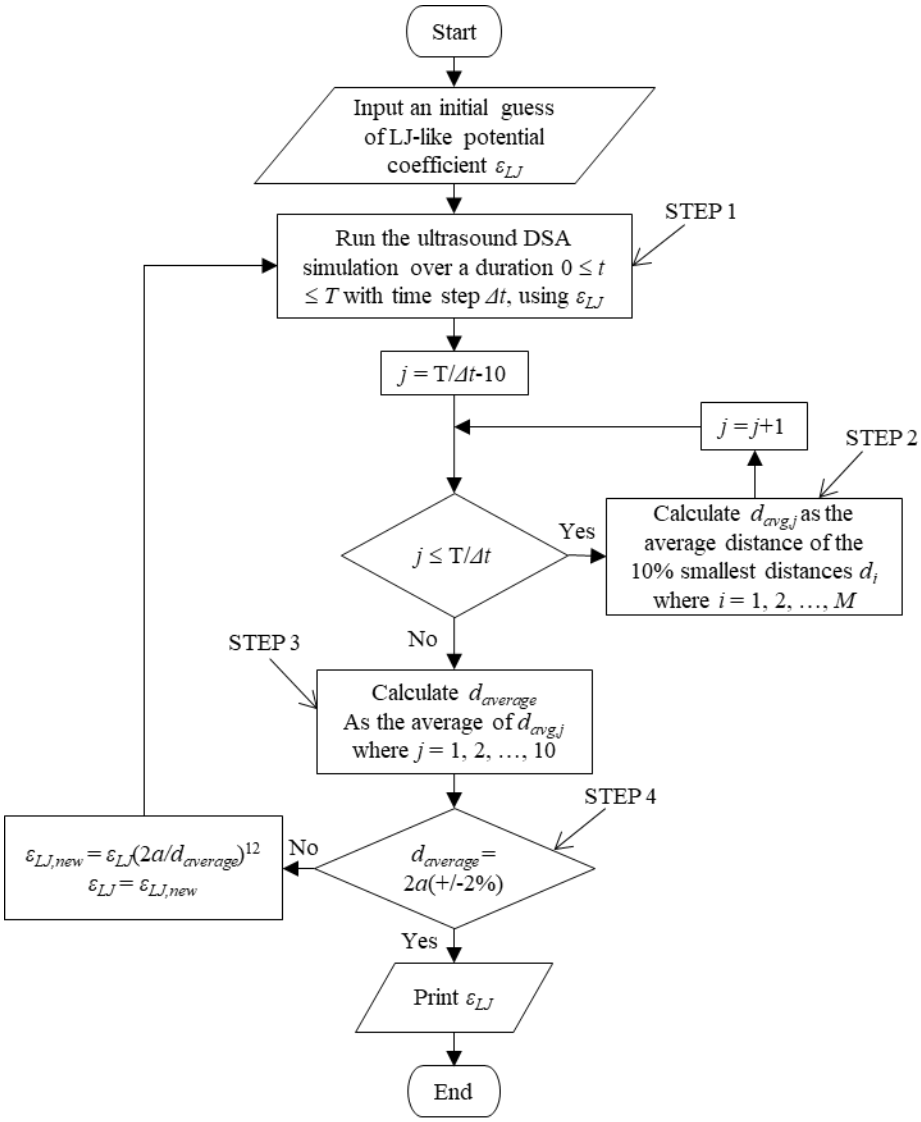

Figure 4.9: Flowchart of the ε_{LJ} parameter tuning procedure.

4.7. References

[1] Greenhall, J., Guevara Vasquez, F., and Raeymaekers, B., 2014, "Dynamic Behavior of Microscale Particles Controlled by Standing Bulk Acoustic Waves," Appl. Phys. Lett., **105**(14), p. 144105.

[2] Noparast, S., Guevara Vasquez, F., and Raeymaekers, B., 2022, "The Effect of Medium Viscosity and Particle Volume Fraction on Ultrasound Directed Self-Assembly of Spherical Microparticles," J. Appl. Phys., **131**(13), p. 134901.

[3] Noparast, S., Guevara Vasquez, F., Francoeur, M., and Raeymaekers, B., 2023, "Measuring and Simulating the Local Packing Density Resulting From Ultrasound-Directed Self-Assembly of Spherical Microparticles into Specific Patterns," Phys. Rev. Appl., **19**(6), p. 064087.

[4] Xie, J.-H., and Vanneste, J., 2014, "Dynamics of a Spherical Particle in an Acoustic Field: A Multiscale Approach," Phys. Fluids, **26**(10), p. 102001.

[5] Guz, A. N., and Zhuk, A. P., 2004, "Motion of Solid Particles in a Liquid under the Action of an Acoustic Field: The Mechanism of Radiation Pressure," Int. Appl. Mech., **40**(3), pp. 246–265.

[6] Haake, A., and Dual, J., 2005, "Contactless Micromanipulation of Small Particles by an Ultrasound Field Excited by a Vibrating Body," J. Acoust. Soc. Am., **117**(5), pp. 2752–2760.

[7] Scholz, M.-S., Drinkwater, B. W., Llewellyn-Jones, T. M., and Trask, R. S., 2015, "Counterpropagating Wave Acoustic Particle Manipulation Device for the Effective Manufacture of Composite Materials," IEEE Trans. Ultrason. Ferroelectr. Freq. Control, **62**(10), pp. 1845–1855.

[8] Aboobaker, N., Blackmore, D., and Meegoda, J., 2005, "Mathematical Modeling of the Movement of Suspended Particles Subjected to Acoustic and Flow Fields," Appl. Math. Model., **29**(6), pp. 515–532.

[9] Weser, R., Deng, Z., V. Kondalkar, V., N. Darinskii, A., Cierpka, C., Schmidt, H., and König, J., 2022, "Three-Dimensional Heating and Patterning Dynamics of Particles in Microscale Acoustic Tweezers," Lab. Chip, **22**(15), pp. 2886–2901.

[10] Settnes, M., and Bruus, H., 2012, "Forces Acting on a Small Particle in an Acoustical Field in a Viscous Fluid," Phys. Rev. E, **85**(1), p. 016327.

[11] Chen, X., and Apfel, R. E., 1996, "Radiation Force on a Spherical Object in an Axisymmetric Wave Field and Its Application to the Calibration of High-frequency Transducers," J. Acoust. Soc. Am., **99**(2), pp. 713–724.

[12] Khan, A. R., and Richardson, J. F., 1987, "The Resistance to Motion of a Solid Sphere in a Fluid," Chem. Eng. Commun., **62**(1–6), pp. 135–150.

[13] Wang, X., Ramírez-Hinestrosa, S., Dobnikar, J., and Frenkel, D., 2020, "The Lennard-Jones Potential: When (Not) to Use It," Phys. Chem. Chem. Phys., **22**(19), pp. 10624–10633.

[14] Uchino, K., 2017, *Advanced Piezoelectric Materials: Science and Technology*, Woodhead Publishing.

[15] Kinsler, L. E., Kinsler, L. E., Frey, A. R., Coppens, A. B., and Sanders, J. V., 2000, *Fundamentals of Acoustics*, Wiley.

[16] Liang, J., Francoeur, M., Williams, C. B., and Raeymaekers, B., 2023, “Curing Characteristics of a Photopolymer Resin with Dispersed Glass Microspheres in Vat Polymerization 3D Printing,” ACS Appl. Polym. Mater.
[17] Haynes, W. M., Lide, D. R., and Bruno, T. J., 2014, *CRC Handbook of Chemistry and Physics*, CRC Press, Boca Raton.
[18] Weibel, E. R., 1963, *Morphometry of the Human Lung*, Springer Berlin Heidelberg, Berlin, Heidelberg.
[19] Underwood, E. E., 1969, “Stereology, or the Quantitative Evaluation of Microstructures,” J. Microsc., **89**(2), pp. 161–180.
[20] Weibel, E. R., and Gomez, D. M., 1962, “A Principle for Counting Tissue Structures on Random Sections,” J. Appl. Physiol., **17**(2), pp. 343–348.
[21] Courtney, C. R. P., Ong, C.-K., Drinkwater, B. W., Bernassau, A. L., Wilcox, P. D., and Cumming, D. R. S., 2011, “Manipulation of Particles in Two Dimensions Using Phase Controllable Ultrasonic Standing Waves,” Proc. R. Soc. Math. Phys. Eng. Sci., **468**(2138), pp. 337–360.
[22] Franklin, A., Marzo, A., Malkin, R., and Drinkwater, B. W., 2017, “Three-Dimensional Ultrasonic Trapping of Micro-Particles in Water with a Simple and Compact Two-Element Transducer,” Appl. Phys. Lett., **111**(9), p. 094101.
[23] Silva, G. T., and Bruus, H., 2014, “Acoustic Interaction Forces between Small Particles in an Ideal Fluid,” Phys. Rev. E, **90**(6), p. 063007.
[24] Greenhall, J., and Raeymaekers, B., 2017, “3D Printing Macroscale Engineered Materials Using Ultrasound Directed Self-Assembly and Stereolithography,” Adv. Mater. Technol., **2**(9), p. 1700122.

CHAPTER 5

CALCULATING THE ACOUSTIC RADIATION FORCE ON SPHERICAL PARTICLES IN A STANDING ULTRASOUND WAVE FIELD CONSIDERING SINGLE AND MULTIPLE SCATTERING

Adapted with permission from Noparast, S., Guevara Vasquez, F., Francoeur, M., and Raeymaekers, B., 2024, "Calculating the acoustic radiation force on spherical particles in a standing ultrasound wave field considering single and multiple scattering," Appl. Phys. Lett., **124**(19), p. 192204. Copyright 2024 AIP Publishing.

5.1. Introduction

The acoustic radiation force is the superposition of the primary acoustic radiation force, which results from the incident standing ultrasound wave, and the acoustic interaction force, which originates from the acoustic interactions between neighboring particles [1]. Researchers have studied the acoustic interactions between spherical particles using single scattering (see, e.g. [1–6]) and multiple scattering (see, e.g. [7–11]), and several publications argue that the effect of multiple scattering on the acoustic radiation force is small, and can be neglected in favor of single scattering [1,3,5,6]. However, physically, it appears that multiple scattering becomes increasingly important with increasing particle volume fraction and local particle packing density, when particles are in close proximity and the acoustic interactions between them increase [12].

Accurately calculating the acoustic radiation force is essential when using ultrasound DSA in engineering applications. For instance, when manufacturing engineered composite materials using ultrasound DSA, the organization and orientation of the filler in the matrix is crucial to implement tailored mechanical, electrical, or thermal properties, or even create embedded electrical wiring and electromagnetic shielding. Consequently, several researchers have studied the effect of using different scattering approaches in ultrasound DSA simulations. Many research groups, including ours, have studied the effect of ultrasound DSA process parameters on the organization and orientation of particles in multiple dimensions in both inviscid and viscous media based only on the primary acoustic radiation force, i.e., neglecting the acoustic interaction force (e.g. spherical particles in 1D [13,14], 2D [15–17], and 3D [18–20], high aspect ratio particles in 2D [21–23] and 3D [24,25]). On the other hand, several researchers have also accounted for both the primary acoustic radiation force and acoustic interaction force using single scattering (e.g. [1–6]) and multiple scattering (e.g. [7–11]). These works demonstrate that scattering of a plane

ultrasound wave between spherical particles can either strengthen or weaken the acoustic radiation force depending on their size and location relative to each other. Furthermore, they show that single scattering dominates multiple scattering.

Specifically, Silva and Bruus [1] theoretically described the acoustic interaction force between spherical particles in an inviscid medium subject to a plane ultrasound wave, accounting for single scattering only. They showed that the acoustic interaction force can be attractive or repulsive in the plane parallel to wave propagation direction. Sepehrirahnama and Lim [6] expanded this work to include non-plane (Bessel) standing ultrasound waves, and illustrated that single scattering is the dominant contribution to the acoustic interaction force. Additionally, and similar to Silva and Bruus [1], Lopes et al. [9] analyzed the acoustic interaction force between spherical particles in an inviscid medium subject to a plane ultrasound wave, but accounted for multiple scattering. They determined that the effect of multiple scattering on the acoustic interaction force depends on the position of the particles relative to each other and to the wave propagation direction.

The literature does not provide a comparison between the acoustic radiation force that acts on spherical particles in a viscous medium when accounting for single or multiple scattering. However, this information is important to accurately simulate the locations where particles organize during ultrasound DSA. Hence, the objective of this chapter is to quantify the relative contributions of single and multiple scattering in the calculation of the acoustic radiation force for spherical particle in a viscous medium, as a function of the ultrasound DSA process parameters, including particle size, material properties, and medium viscosity.

We first consider a theoretical case with three spherical particles in a viscous medium, and derive operating maps that quantify the deviation between the acoustic radiation force based on

single and multiple scattering as a function of the ultrasound DSA process parameters. Then, we consider a realistic system with hundreds of particles dispersed in a viscous medium relevant to e.g. manufacturing engineered materials, and we relate the fundamental knowledge of the three-particle system to the large-scale system.

5.2. Methods

5.2.1. Three-particle system

Figure 5.1 illustrates the theoretical model of a three-particle system to methodically simulate the acoustic radiation force, accounting for single F_{single} and multiple scattering $F_{multiple}$. Figure 5.1 (a) shows an isometric view of a rectangular reservoir (gray) with two ultrasound transducers affixed to opposing walls (orange) that establish a standing ultrasound wave within the viscous medium contained in the reservoir.

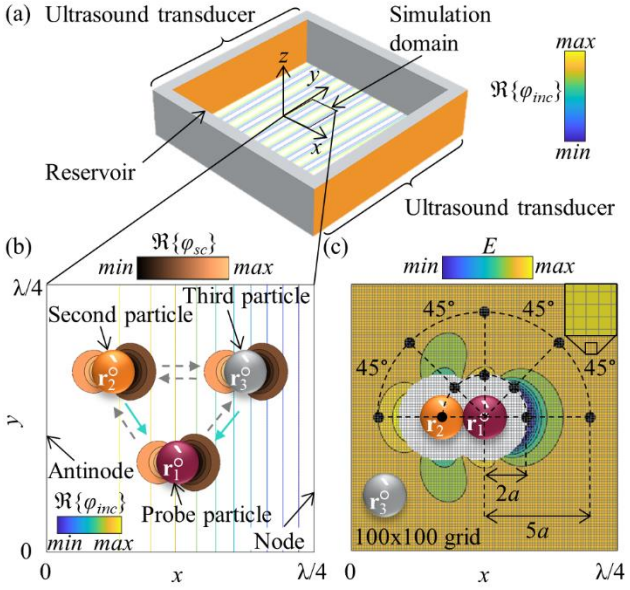

Figure 5.1: Three-particle system, showing (a) schematic of a reservoir (gray) with two ultrasound transducers (orange) and the magnitude of the incident velocity potential φ_{inc} (color contours) that result from the incident standing ultrasound wave, (b) schematic illustration of single (teal arrows) and multiple (teal and gray arrows) scattering in the three-particle system, superimposed on the incident velocity potential φ_{inc} (color contours) that result from the incident standing ultrasound wave between a single node and antinode, and (c) locations of the probe (first) particle, as well as the second and third particle, to methodically study the effect of single and multiple scattering on the acoustic radiation force at the probe particle, showing the exclusion area for the third particle centers (white area).

We simulate the incident velocity potential of a plane standing ultrasound wave as $\varphi_{inc}(\mathbf{r}) = e^{i\tilde{k}(x-L/2)} + e^{i\tilde{k}(-x+L/2)}$ inside the reservoir [26]. The color contours in Fig. 5.1 (a) show the magnitude of the incident velocity potential $\Re\{\varphi_{inc}\}$. The distance between both ultrasound transducers $L = 20\lambda$, $\tilde{k} = (\omega/c_m)/(1-i\omega\tau_s)^{1/2}$ is the complex wave number that accounts for acoustic attenuation in the viscous medium with τ_s is the viscous dissipation time to dampen the acoustic pressure to $1/e$ of its original value [27], c_m is the sound propagation velocity of the medium, ω is the angular frequency, and λ is the wavelength. The incident wave velocity $\boldsymbol{v}_{inc}(\mathbf{r}) = \nabla\varphi_{inc}(\mathbf{r})$.

Figure 5.1 (b) schematically illustrates single (teal arrows) and multiple (teal and gray arrows) scattering between three particles. We calculate the acoustic radiation force at the location of the first particle, which we refer to as the probe particle (maroon). We methodically position the second (orange) and third (gray) particles at all possible locations between a single node and an antinode of the standing ultrasound wave, and calculate the acoustic radiation force at the probe particle for each combination of particle locations. Vectors $\mathbf{r}_1$, $\mathbf{r}_2$, and $\mathbf{r}_3$ describe the locations of the three particles with respect to the origin of the coordinate system in the simulation domain. Using single scattering, the incident wave scatters off the second and third particles once, and these scattered waves superimpose on the incident wave at the probe particle (teal arrows in Fig. 5.1 (b)). In contrast, when considering multiple scattering, the incident wave scatters multiple times between the three particles, and multiple scattered waves superimpose on the incident wave at the probe particle (both teal and gray arrows in Fig. 5.1 (b)).

We express the velocity potential of the ultrasound wave φ_{sc} that scatters off the j^{th} particle located at $\mathbf{r}_j$ and measured at the i^{th} particle located at $\mathbf{r}_i$, accounting for both monopole (first term in Eq. (5.1)) and dipole (second term in Eq. (5.1)) scattering as follows [28,29],

$$\varphi_{sc}(\mathbf{r}_i,\mathbf{r}_j) = \sigma\varphi(\mathbf{r}_j)G(\mathbf{r}_i,\mathbf{r}_j) + (\mathbf{P}\mathbf{v}(\mathbf{r}_j)).\frac{1}{k^2}\nabla G(\mathbf{r}_i,\mathbf{r}_j). \tag{5.1}$$

Here, $\varphi(\mathbf{r}_j)$ and $\mathbf{v}(\mathbf{r}_j) = \nabla\varphi(\mathbf{r}_j)$ are the velocity potential and wave velocity at location $\mathbf{r}_j$, which both derive from the Helmholtz equation that describes the ultrasound wave within the simulation domain. $G(\mathbf{r}_i, \mathbf{r}_j) = e^{ik|\mathbf{r}_i-\mathbf{r}_j|}/(4\pi|\mathbf{r}_i-\mathbf{r}_j|)$ is the Green's function for the Helmholtz equation in 3D [30], which relates the ultrasound wave at the particles and the rest of the simulation domain. $\nabla G(\mathbf{r}_i, \mathbf{r}_j)$ is the gradient of the Green's function, and $k = \Re\{\tilde{k}\}$ because viscous attenuation of the ultrasound wave is small over the short distance between a single node and antinode considered in this paper ($\approx 0.08\%$). $\sigma = 4\pi f_1 k^2 a^3/3$ and $\mathbf{P} = -2\pi f_2 k^2 a^3 \mathbf{I}_{3\times3}$ are functions of the monopole f_1 and dipole f_2 scattering coefficients [31], respectively, where a is the particle radius, and $\mathbf{I}_{3\times3}$ is a three-by-three identity matrix. The monopole scattering coefficient f_1 is a function of the compressibility ratio β_p/β_m, and the dipole scattering coefficient f_2 is a function of the density ratio ρ_p/ρ_m and medium viscosity η_m, where β and ρ are compressibilty and density, and subscripts p and m refer to the particle and the fluid medium, respectively [31]. Figure 5.1 (b) visualizes the magnitude of the monopole and dipole scattering velocity potentials $\Re\{\varphi_{sc}\}$ for all particles (solid copper-color contour plots).

Thus, when considering multiple scattering, the total velocity potential $\varphi(\mathbf{r}_i)$ at location $\mathbf{r}_i$ is the superposition of the incident velocity potential $\varphi_{inc}(\mathbf{r}_i)$ and the sum of the velocity potentials φ_{sc} that result from the ultrasound wave scattering off all other particles, also evaluated at $\mathbf{r}_i$, i.e.,

$$\varphi(\mathbf{r}_i) = \varphi_{inc}(\mathbf{r}_i) + \sum_{\substack{j=1 \\ j\neq i}}^{N} \varphi_{sc}(\mathbf{r}_i, \mathbf{r}_j)\,. \tag{5.2}$$

$N = 3$ is the number of particles. Combining Eqs. (5.1) and (5.2) yields

$$\varphi(\mathbf{r}_i) = \varphi_{inc}(\mathbf{r}_i) + \sum_{\substack{j=1 \\ j\neq i}}^{N} \left[\sigma\varphi(\mathbf{r}_j) G(\mathbf{r}_i, \mathbf{r}_j) + (\mathbf{P}\mathbf{v}(\mathbf{r}_j)).\frac{1}{k^2}\nabla G(\mathbf{r}_i, \mathbf{r}_j) \right]. \tag{5.3}$$

Furthermore, $\mathbf{v}(\mathbf{r}_i) = \nabla\varphi(\mathbf{r}_i)$, i.e.,

$$\mathbf{v}(\mathbf{r}_i) = \mathbf{v}_{inc}(\mathbf{r}_i) + \sum_{\substack{j=1 \\ j \neq i}}^{N} \left[\sigma\varphi(\mathbf{r}_j)\nabla G(\mathbf{r}_i, \mathbf{r}_j) + \frac{1}{k^2}\nabla^2 G(\mathbf{r}_i, \mathbf{r}_j)\mathbf{P}\mathbf{v}(\mathbf{r}_j) \right], \tag{5.4}$$

where $\nabla^2 G(\mathbf{r}_i,\mathbf{r}_j)$ is the Hessian of the Green's function [32]. We show the linear systems to calculate $\varphi(\mathbf{r}_i)$ (Eq. (5.3)) and $\mathbf{v}(\mathbf{r}_i)$ (Eq. (5.4)) in the Appendix. The ARP at the location of the probe particle $\mathbf{r}_1$ is [31]

$$U(\mathbf{r}_1) = \frac{4\pi}{3}a^3 \left(f_1 \frac{\beta_m}{2} \left\langle (i\rho_m \omega \varphi(\mathbf{r}_1))^2 \right\rangle - f_2 \frac{3\rho_m}{4} \left\langle v_x(\mathbf{r}_1)^2 \right\rangle \right), \tag{5.5}$$

where $v_x(\mathbf{r}_1)$ is the x-component of $\mathbf{v}(\mathbf{r}_1)$, and operator $\langle \bullet \rangle$ averages over a single wave period. The acoustic radiation force with multiple scattering $F_{multiple} = -\partial U(\mathbf{r}_1)/\partial x$, using $\varphi(\mathbf{r}_1)$ and $\mathbf{v}(\mathbf{r}_1)$ from Eq. (5.6), and the acoustic radiation force with single scattering $F_{single} = -\partial U(\mathbf{r}_1)/\partial x$, using $\varphi(\mathbf{r}_1)$ and $\mathbf{v}(\mathbf{r}_1)$ from Eq. (5.10). In addition, the primary acoustic radiation force $F_{inc} = -\partial U(\mathbf{r}_1)/\partial x$, using $\varphi_{inc}(\mathbf{r}_1)$ and $v_{inc,x}(\mathbf{r}_1)$ in Eq. (5.5), where $v_{inc,x}(\mathbf{r}_1)$ is the x-component of the incident velocity vector $\mathbf{v}_{inc}(\mathbf{r}_1)$. Note that $v_{inc,y}(\mathbf{r}_1) = v_{inc,z}(\mathbf{r}_1) = 0$ for a plane standing ultrasound wave. We compute the percent deviation between the acoustic radiation force from single and multiple scattering, relative to the primary acoustic radiation force as $E = |F_{multiple} - F_{single}/F_{inc}|$.

Figure 5.1 (c) illustrates the possible configurations of the probe, second, and third particles for which we evaluate E. We fix the probe particle at $x = \lambda/8$, i.e., the middle between a node and antinode (white hollow marker), select ten locations for the second particle (black solid marker), and 100 × 100 locations of the third particle (silver grid, see magnified inset image) in the simulation domain. We select the locations of the second particle based on symmetry, and we limit it to ten locations to manage computational cost. Five of these locations involve contact between the probe and the second particle, whereas the other five locations allow for the third particle to be between the probe and the second particles. Figure 5.1 (c) illustrates a typical result of E (solid color contour plot) for a single configuration of probe and second particles, and for 100 × 100

locations of the third particle. The white area around the probe and second particles in Fig. 5.1 (c) is the exclusion area that the third particle centers cannot occupy to prevent overlap.

We determine the maximum deviation E_{max} = max(E) as a function of ultrasound DSA process parameters and material properties, including the particle size a, the medium viscosity η_m, medium and particle density ρ_m and ρ_p, and medium and particle compressibility β_m and β_p. The Buckingham π theorem [33] determines that four nondimensional parameters are required to describe this system: (i) the nondimensional particle size $0.05 \leq K_1 = ka \leq 0.20$, which we select to satisfy the Rayleigh regime assumption ($ka << 1$), (ii) the nondimensional medium viscosity $0.00 < K_2 = \eta_m/\rho_m\lambda c_m \leq 0.27$ that spans the viscosity range of different fluid media previously used with ultrasound DSA in the context of manufacturing engineered materials (e.g. water, photopolymer, thermoset resin) $0 < \eta_m \leq 400$ mPa·s [12], (iii) the density ratio $0 \leq \rho_p/\rho_m \leq 2.5$, and (iv) the compressibility ratio $0 \leq \beta_p/\beta_m \leq 2.5$ that span the density and compressibility ratios of relevant combinations of particles and media for manufacturing of engineered materials [31].

5.2.2. Large-scale system

Figure 5.2 illustrates the theoretical model of a large-scale system to simulate the acoustic radiation force accounting for both single F_{single} and multiple scattering $F_{multiple}$, considering hundreds of randomly dispersed particles in a viscous medium. Figure 5.2 shows the same reservoir (gray) of Fig. 5.1 with two ultrasound transducers (orange) that establish a standing ultrasound wave within the viscous medium contained in the reservoir. We fixate the probe particle at $x = \lambda/8$ (maroon particle), and randomly disperse $N = 320$ particles in the solution domain, which scales to satisfy a specific particle volume fraction $5\% \leq \Phi \leq 20\%$. We compute the percent deviation E between the acoustic radiation force for single and multiple scattering, and we measure

the distance d between the probe particle and its closest neighbor. For each value of Φ, we perform 250 repeat simulations to quantify the variability of E as a result of the random positions of the particles that affects d.

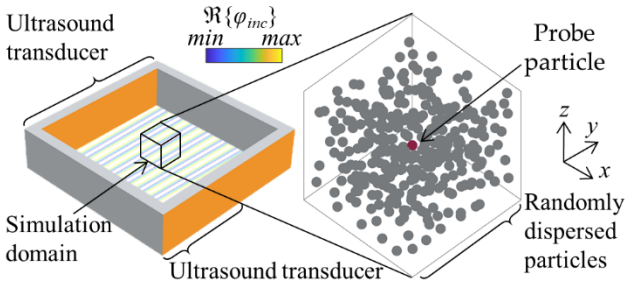

Figure 5.2: Schematic of a reservoir (gray) with two ultrasound transducers (orange) and the magnitude of the incident velocity potential φ_{inc} (color contours) that result from the incident standing ultrasound wave. We highlight the probe particle (maroon) at the center of the simulation domain, in addition to several hundred randomly dispersed particles (gray).

5.3. Results and discussion

5.3.1. Three particle system

Figure 5.3 shows the ratio of the acoustic radiation forces that account for scattering and the incident ultrasound wave for (a) single $F_{single,x} / F_{inc,x}$ and (b) multiple scattering $F_{multiple,x} / F_{inc,x}$ in the three-particle system. Figure 5.3 (c) shows the deviation E between single and multiple scattering. Figure 5.3 shows results for ten different locations of the second particle relative to the probe particle, and with the third particle at each of the 100 × 100 grid points. The results are for a single combination of nondimensional parameters: $K_1 = 0.12$, $K_2 = 0.14$, $\rho_p/\rho_m = 2.4$, and $\beta_p/\beta_m = 0.029$, which represent ultrasound DSA of aluminum spherical particles (a = 19 μm, ρ_p = 2,700 kg/m^3, and $\beta_p = 1.3 \cdot 10^{-11}$ Pa^{-1})[30] in photopolymer resin (η_m = 200 mPa.s, ρ_m = 1,110 kg/m^3, and $\beta_m = 4.5 \cdot 10^{-10}$ Pa^{-1})[12] with $k = 6.64 \cdot 10^3$.

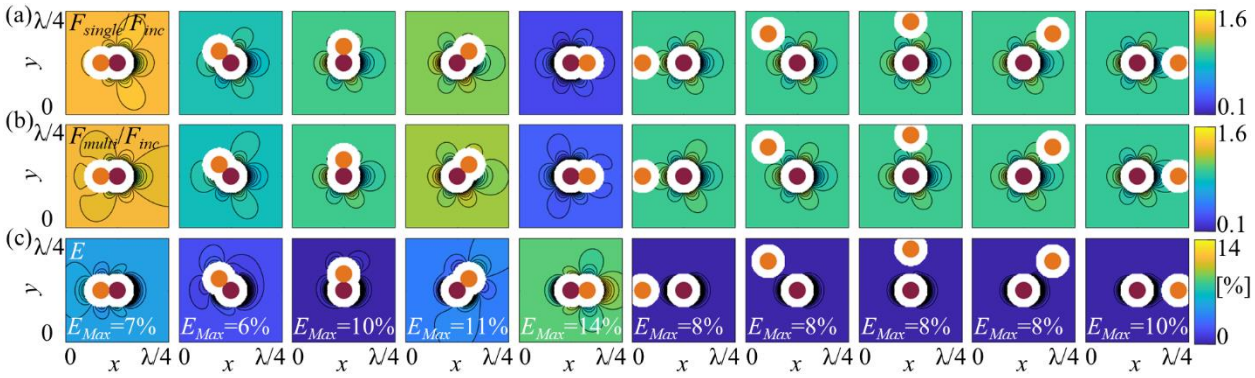

Figure 5.3: (a) Single scattering ratio $F_{single,x}/F_{inc,x}$, (b) multiple scattering ratio $F_{multiple,x}/F_{inc,x}$, and (c) the deviation E and E_{Max} for ten locations of the second particle (orange) with respect to the probe particle (maroon), and 100 x 100 locations of the third particle (not shown), and a single combination of nondimensional ultrasound DSA parameters and material properties: $K_1 = 1.2$, $K_2 = 0.14$, $\rho_p / \rho_m = 2.4$, and $\beta_p / \beta_m = 0.029$.

We observe from Fig. 5.3 that $F_{single,x} / F_{inc,x}$, $F_{multiple,x} / F_{inc,x}$, and E depend on the relative locations of the three particles, which affects both monopole and dipole scattering ($G(\mathbf{r}_n,\mathbf{r}_j)$ and $\nabla G(\mathbf{r}_n,\mathbf{r}_j)$ in Eq. (5.3)). Furthermore, the angle between their lines of centers and the wave propagation direction (x-direction) affects the dipole scattering coefficient ($\nabla G(\mathbf{r}_n,\mathbf{r}_j)$ in Eq. (5.3)). Generally, maximum values of $F_{single,x}/F_{inc,x}$, $F_{multiple,x}/F_{inc,x}$, and E_{max} occur where particles contact each other in the wave propagation direction.

Figure 5.4 shows the maximum percent deviation E_{max} between the acoustic radiation force based on single and multiple scattering, (a) as a function of nondimensional particle size K_1 and nondimensional medium viscosity K_2 for $\rho_p/\rho_m = 2.4$ and $\beta_p/\beta_m = 0.029$, (b) as a function of density ratio ρ_p/ρ_m and compressibility ratio β_p/β_m for $K_1 = 1.2$, and $K_2 = 0.14$, where the particle is denser and less compressible than the fluid medium ($\rho_p/\rho_m \geq 1$ and $\beta_p/\beta_m \leq 1$), and (c) as a function of density ratio ρ_p/ρ_m and compressibility ratio β_p/β_m for $K_1 = 1.2$, and $K_2 = 0.14$, where the particle is less dense and more compressible than the fluid medium ($\rho_p/\rho_m \leq 1$ and $\beta_p/\beta_m \geq 1$).

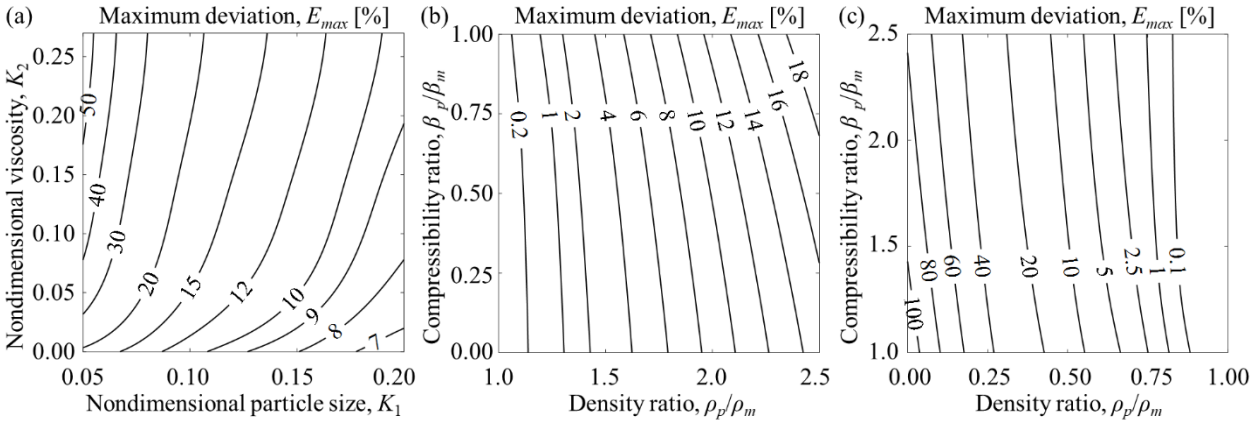

Figure 5.4: Percent deviation E_{max} between the acoustic radiation force based on single and multiple scattering (a) as a function of K_1 and K_2 for $\rho_p/\rho_m = 2.4$ and $\beta_p/\beta_m = 0.029$, (b) as a function of ρ_p/ρ_m and β_p/β_m for $\rho_p/\rho_m \geq 1$, $\beta_p/\beta_m \leq 1$, $K_1 = 1.2$, and $K_2 = 0.14$, and (c) as a function of ρ_p/ρ_m and β_p/β_m for $\rho_p/\rho_m \leq 1$, $\beta_p/\beta_m \geq 1$, $K_1 = 1.2$, and $K_2 = 0.14$.

From Fig. 5.4 (a), we observe that E_{max} increases with K_1 and increasing K_2. Decreasing K_1 decreases the distance between neighboring particles, which increases the dipole scattering term (second term) in Eq. (5.1) that affects both single and multiple scattering and, thus, increases E_{max}. Furthermore, we observe from Fig. 5.4 (b) and (c) that E_{max} increases with increasing ρ_p/ρ_m and increasing β_p/β_m. First, in the Rayleigh regime ($ka << 1$), dipole dominates monopole scattering because the gradient of the Green's function $k^{-1}\nabla G(\mathbf{r}_i,\mathbf{r}_j)$ in the x-direction is larger than the Green's function $G(\mathbf{r}_i,\mathbf{r}_j)$ itself (see Eq. (5.1)). Second, maximum scattering between particles occurs when their line of centers is parallel to the wave propagation direction where the Green's function gradient $k^{-1}\nabla G(\mathbf{r}_i,\mathbf{r}_j)$ is maximum. Under these circumstances, dipole scattering causes particles to repel each other, whereas monopole scattering causes particles to attract each other. Thus, monopole scattering and dipole scattering counteract each other in the x-direction, where the effect of dipole scattering is dominant. As a result, increasing ρ_p/ρ_m and β_p/β_m increases the dipole scattering coefficient f_2 and decreases the monopole scattering coefficient f_1, respectively. Since the scattering coefficients affect both single and multiple scattering, it increases $F_{single,x}/F_{inc,x}$ and $F_{multiple,x}/F_{inc,x}$ and, thus, E_{max}.

Finally, E_{max} can reach up to 100%, which contrasts the prevailing conclusion in the literature that the effect of multiple scattering is negligible compared to single scattering in the calculation of the acoustic interaction force and acoustic radiation force (e.g. [1,3,5,6]). These previous works have focused on systems with two rather than three (or many) particles, which cannot entirely describe the effect of multiple scattering, and explains the difference with the results of this chapter.

5.3.2. Large-scale system

Figure 5.5 (a) shows the percent deviation E versus the shortest distance between neighboring particles d for 250 different configurations of 320 randomly dispersed particles around the probe particle, for four different particle volume fractions Φ = 5, 10, 15, and 20%, and for a single combination of nondimensional parameters: K_1 = 0.05, K_2 = 0.27, ρ_p/ρ_m = 2.4, and β_p/β_m = 0.029. We use transparent solid data points so that increasing darkness signifies an increasing number of overlapping data points. Decreasing the distance d between the probe particle and its nearest neighbor increases the deviation E, independent of Φ, because the distance between particles is one of the main parameters that drives the relative importance between monopole and dipole scattering (see Fig. 5.3). Additionally, the likelihood of a small distance $d \approx 2a$ increases with increasing Φ because it increases the number of non-overlapping particles in the solution domain, which necessarily decreases d.

Figure 5.5 (b) shows the probability density function of E, and its mean value for 250 configurations of 320 randomly dispersed particles around the probe particle, for the results of Fig. 5.5 (a). The likelihood of high E values increases with increasing Φ because of decreasing d.

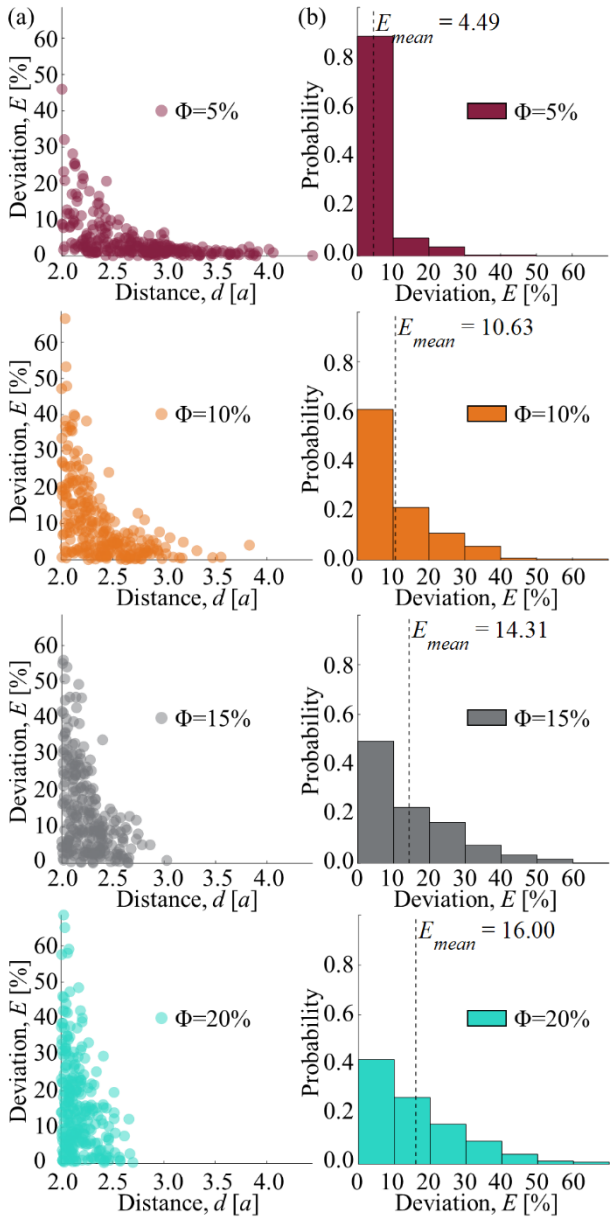

Figure 5.5: (a) Percent deviation E versus d for 250 different configurations of 320 randomly dispersed particles around the probe particle and (b) probability density function of E and the mean value for the results of (a), for four different particle volume fractions Φ = 5, 10, 15, and 20%, and for a single combination of nondimensional parameters and material properties: K_1 = 0.05, K_2 = 0.27, ρ_p/ρ_m = 2.4, and β_p/β_m = 0.029.

This methodical study of the deviation between the acoustic radiation force on a spherical particle in a viscous medium based on single and multiple scattering highlights the importance of considering multiple scattering effects in ultrasound DSA simulations under certain conditions. The operating maps guide the choice between using single and multiple scattering in ultrasound

DSA simulations. However, the results show limitations. We simulate the incident wave as a perfect plane standing wave. Realistic transducers cannot generate a perfect wave, and reflections from the near-field will interfere with the reservoir walls and potentially affect the results slightly. Furthermore, the medium viscosity may induce nonlinear phenomena such as streaming at the reservoir walls and microstreaming around the particles, which could affect the acoustic radiation force calculation [34,35]. In practice, imperfect dispersion, shape, and size of the spherical particles as well as thermal fluctuations in the viscous medium [36] also affect the acoustic radiation force.

5.4. Conclusions

We conclude that the deviation E between the acoustic radiation force derived from single and multiple scattering may reach up to 100%, depending on the ultrasound DSA process parameters and material properties. Thus, neglecting multiple scattering in favor of computationally efficient single scattering is not always correct. Furthermore, the maximum deviation E_{max} increases with decreasing nondimensional particle size K_1 and increasing nondimensional medium viscosity K_2, and with increasing density ratio ρ_p/ρ_m and increasing compressibility ratio β_p/β_m, largely driven by increasing dipole scattering that affects both single and multiple scattering, and thus amplifies the difference between the acoustic radiation force calculated based on both approaches. Comparing a fundamental three-particle system to a large-scale system of particles demonstrates that increasing the particle volume fraction Φ increases the need to account for multiple scattering because the acoustic interactions between particles increase when the distance between them decreases.

5.5. Acknowledgments

This research was supported by the National Science Foundation under award CMMI-2130083, DMS-2008610, and DMS-2136198.

5.6. Appendix: Linear system of single and multiple scattering

Eqs. (5.3) and (5.4) form a linear system [29]

$$\mathbf{V} = \left(\mathbf{I}_{4N\times 4N} - \boldsymbol{\Gamma}\mathbf{A}\right)^{-1} \times \mathbf{V}_{inc}, \tag{5.6}$$

Where $\boldsymbol{\Gamma}$ is a 4N×4N matrix specified by 4×4 blocks of $\boldsymbol{\Gamma}_{i,j}$ [29]. For $i = j$, $\boldsymbol{\Gamma}_{i,j} = \mathbf{0}_{4\times 4}$, and for $i \neq j$,

$$\boldsymbol{\Gamma}_{i,j} = \begin{bmatrix} G(\mathbf{r}_i, \mathbf{r}_j) & k^{-1}\nabla G(\mathbf{r}_i, \mathbf{r}_j)^T \\ k^{-1}\nabla G(\mathbf{r}_i, \mathbf{r}_j) & k^{-2}\nabla^2 G(\mathbf{r}_i, \mathbf{r}_j) \end{bmatrix}, \tag{5.7}$$

where the superscript T indicates the transpose of the vector. The matrices $\mathbf{A} = (\sigma, \mathbf{P}, \ldots, \sigma, \mathbf{P})_{4N\times 4N}$,

$$\mathbf{V} = \begin{bmatrix} \varphi(\mathbf{r}_i) \\ k^{-1}\mathbf{v}(\mathbf{r}_i) \end{bmatrix}_{i=1,\ldots,N}, \text{ and} \tag{5.8}$$

$$\mathbf{V}_{inc} = \begin{bmatrix} \varphi_{inc}(\mathbf{r}_j) \\ k^{-1}\mathbf{v}_{inc}(\mathbf{r}_j) \end{bmatrix}_{j=1,\ldots,N}. \tag{5.9}$$

On the other hand, when considering single scattering, we only consider $\varphi(\mathbf{r}_j) = \varphi_{inc}(\mathbf{r}_j)$, i.e., the right-hand side of Eqs. (5.1), (5.3), and (5.4), to reflect that the incident ultrasound wave only scatters once off each particle in the system. Correspondingly, for single scattering $\varphi(\mathbf{r}_i)$ and $\mathbf{v}(\mathbf{r}_i)$ are given by the approximation of Eq. (5.6) [29]

$$\mathbf{V} = \left(\mathbf{I}_{4N\times 4N} + \boldsymbol{\Gamma}\mathbf{A}\right) \times \mathbf{V}_{inc}. \tag{5.10}$$

5.7. References

[1] Silva, G. T., and Bruus, H., 2014, "Acoustic Interaction Forces between Small Particles in an Ideal Fluid," Phys. Rev. E, **90**(6), p. 063007.

[2] Sepehrirahnama, S., Lim, K.-M., and Chau, F. S., 2015, "Numerical Study of Interparticle Radiation Force Acting on Rigid Spheres in a Standing Wave," J. Acoust. Soc. Am., **137**(5), pp. 2614–2622.

[3] Baasch, T., Leibacher, I., and Dual, J., 2017, "Multibody Dynamics in Acoustophoresis," J. Acoust. Soc. Am., **141**(3), pp. 1664–1674.

[4] Crum, L. A., 1975, "Bjerknes Forces on Bubbles in a Stationary Sound Field," J. Acoust. Soc. Am., **57**(6), pp. 1363–1370.

[5] Zhang, S., Qiu, C., Wang, M., Ke, M., and Liu, Z., 2016, "Acoustically Mediated Long-Range Interaction among Multiple Spherical Particles Exposed to a Plane Standing Wave," New J. Phys., **18**(11), p. 113034.

[6] Sepehrirhnama, S., and Lim, K.-M., 2020, "Generalized Potential Theory for Close-Range Acoustic Interactions in the Rayleigh Limit," Phys. Rev. E, **102**(4), p. 043307.

[7] Azarpeyvand, M., Alibakhshi, M., and Self, R., 2012, "Effects of Multi-Scattering on the Performance of a Single-Beam Acoustic Manipulation Device," IEEE Trans. Ultrason. Ferroelectr. Freq. Control, **59**(8), pp. 1741–1749.

[8] Doinikov, A. A., 2001, "Acoustic Radiation Interparticle Forces in a Compressible Fluid," J. Fluid Mech., **444**, pp. 1–21.

[9] Lopes, J. H., Azarpeyvand, M., and Silva, G. T., 2016, "Acoustic Interaction Forces and Torques Acting on Suspended Spheres in an Ideal Fluid," IEEE Trans. Ultrason. Ferroelectr. Freq. Control, **63**(1), pp. 186–197.

[10] Zheng, X., and Apfel, R. E., 1995, "Acoustic Interaction Forces between Two Fluid Spheres in an Acoustic Field," J. Acoust. Soc. Am., **97**(4), pp. 2218–2226.

[11] Sepehrirahnama, S., Chau, F. S., and Lim, K.-M., 2016, "Effects of Viscosity and Acoustic Streaming on the Interparticle Radiation Force between Rigid Spheres in a Standing Wave," Phys. Rev. E, **93**(2), p. 023307.

[12] Noparast, S., Guevara Vasquez, F., Francoeur, M., and Raeymaekers, B., 2023, "Measuring and Simulating the Local Packing Density Resulting From Ultrasound-Directed Self-Assembly of Spherical Microparticles into Specific Patterns," Phys. Rev. Appl., **19**(6), p. 064087.

[13] Greenhall, J., Guevara Vasquez, F., and Raeymaekers, B., 2013, "Continuous and Unconstrained Manipulation of Micro-Particles Using Phase-Control of Bulk Acoustic Waves," Appl. Phys. Lett., **103**(7), p. 074103.

[14] Grinenko, A., Wilcox, P. D., Courtney, C. R. P., and Drinkwater, B. W., 2012, "Proof of Principle Study of Ultrasonic Particle Manipulation by a Circular Array Device," Proc. R. Soc. Math. Phys. Eng. Sci., **468**(2147), pp. 3571–3586.

[15] Courtney, C. R. P., Demore, C. E. M., Wu, H., Grinenko, A., Wilcox, P. D., Cochran, S., and Drinkwater, B. W., 2014, "Independent Trapping and Manipulation of Microparticles Using Dexterous Acoustic Tweezers," Appl. Phys. Lett., **104**(15), p. 154103.

[16] Greenhall, J., Guevara Vasquez, F., and Raeymaekers, B., 2016, "Ultrasound Directed Self-Assembly of User-Specified Patterns of Nanoparticles Dispersed in a Fluid Medium," Appl. Phys. Lett., **108**(10), p. 103103.

[17] Cherkaev, E., Guevara Vasquez, F., Mauck, C., Prisbrey, M., and Raeymaekers, B., 2021, "Wave-Driven Assembly of Quasiperiodic Patterns of Particles," Phys. Rev. Lett., **126**(14), p. 145501.
[18] Ochiai, Y., Hoshi, T., and Rekimoto, J., 2014, "Three-Dimensional Mid-Air Acoustic Manipulation by Ultrasonic Phased Arrays," PLoS ONE, **9**(5), p. e97590.
[19] Prisbrey, M., Greenhall, J., Guevara Vasquez, F., and Raeymaekers, B., 2017, "Ultrasound Directed Self-Assembly of Three-Dimensional User-Specified Patterns of Particles in a Fluid Medium," J. Appl. Phys., **121**(1), p. 014302.
[20] Hoshi, T., Ochiai, Y., and Rekimoto, J., 2014, "Three-Dimensional Noncontact Manipulation by Opposite Ultrasonic Phased Arrays," Jpn. J. Appl. Phys., **53**(7S), p. 07KE07.
[21] Niendorf, K., and Raeymaekers, B., 2020, "Quantifying Macro- and Microscale Alignment of Carbon Microfibers in Polymer-Matrix Composite Materials Fabricated Using Ultrasound Directed Self-Assembly and 3D-Printing," Compos. Part Appl. Sci. Manuf., **129**, p. 105713.
[22] Prisbrey, M., and Raeymaekers, B., 2019, "Aligning High-Aspect-Ratio Particles in User-Specified Orientations with Ultrasound-Directed Self-Assembly," Phys. Rev. Appl., **12**(1), p. 014014.
[23] Scholz, M.-S., Drinkwater, B. W., and Trask, R. S., 2014, "Ultrasonic Assembly of Anisotropic Short Fibre Reinforced Composites," Ultrasonics, **54**(4), pp. 1015–1019.
[24] Prisbrey, M., and Raeymaekers, B., 2018, "Ultrasound Noncontact Particle Manipulation of Three-Dimensional Dynamic User-Specified Patterns of Particles in Air," Phys. Rev. Appl., **10**(3), p. 034066.
[25] Prisbrey, M., Guevara Vasquez, F., and Raeymaekers, B., 2020, "Arranging Ellipsoidal Particles in Three-Dimensional User-Specified Orientations with Ultrasound-Directed Self-Assembly," Phys. Rev. Appl., **14**(2), p. 024026.
[26] Greenhall, J., Guevara Vasquez, F., and Raeymaekers, B., 2014, "Dynamic Behavior of Microscale Particles Controlled by Standing Bulk Acoustic Waves," Appl. Phys. Lett., **105**(14), p. 144105.
[27] Kinsler, L. E., Frey, A. R., Coppens, A. B., and Sanders, J. V., 2000, *Fundamental of Acoustic*, John Wiley & Sons, Inc, New York.
[28] Huang, K., Solna, K., and Zhao, H., 2010, "Generalized Foldy-Lax Formulation," J. Comput. Phys., **229**(12), pp. 4544–4553.
[29] Martin, P. A., 2006, *Multiple Scattering: Interaction of Time-Harmonic Waves with N Obstacles*, Cambridge University Press, Cambridge.
[30] Haynes, W. M., Lide, D. R., and Bruno, T. J., 2014, *CRC Handbook of Chemistry and Physics*, CRC Press, Boca Raton.
[31] Settnes, M., and Bruus, H., 2012, "Forces Acting on a Small Particle in an Acoustical Field in a Viscous Fluid," Phys. Rev. E, **85**(1), p. 016327.
[32] "DLMF: NIST Digital Library of Mathematical Functions" [Online]. Available: https://dlmf.nist.gov/. [Accessed: 14-Feb-2024].
[33] Yarin, L. P., 2012, *The Pi-Theorem: Applications to Fluid Mechanics and Heat and Mass Transfer*, Springer, Berlin, Heidelberg.
[34] St. Clair, N., Davenport, D., Kim, A. D., and Kleckner, D., 2023, "Dynamics of Acoustically Bound Particles," Phys. Rev. Res., **5**(1), p. 013051.
[35] Pavlic, A., Ermanni, L., and Dual, J., 2022, "Interparticle Attraction along the Direction of the Pressure Gradient in an Acoustic Standing Wave," Phys. Rev. E, **105**(5), p. L053101.

[36] Doinikov, A. A., 1997, “Acoustic Radiation Force on a Spherical Particle in a Viscous Heat-Conducting Fluid. II. Force on a Rigid Sphere,” J. Acoust. Soc. Am., **101**(2), pp. 722–730.

CHAPTER 6

CONCLUSION

The research in this dissertation illustrates an experimentally validated theoretical model to determine the steady-state locations where spherical particles assemble during ultrasound DSA as a function of medium viscosity and particle volume fraction and an experimentally validated theoretical model to quantify the steady-state and transient local packing density of spherical particles within the pattern features that result from ultrasound DSA.

First, we quantify and predict the locations where spherical particles assemble during ultrasound DSA in a viscous medium, considering the effects of medium viscosity and particle volume fraction. The locations where spherical particles assemble during ultrasound DSA are different in a viscous and inviscid medium and depend on particle volume fraction Φ and medium viscosity η_m. The deviation between locations where particles assemble during ultrasound DSA in viscous and inviscid media increases with increasing particle volume fraction and medium viscosity because the sound propagation velocity of the mixture of particles and viscous medium changes compared to that of the inviscid medium.

Second, we quantify and predict the steady-state local particle packing density of spherical particles within the pattern features that result from ultrasound DSA. We also characterize the effect of process parameters such as particle size a, particle volume fraction φ, and medium

viscosity η_m on the steady-state local particle packing density. The local particle packing density at the pattern features increases with increasing particle volume fraction Φ or decreasing particle size *a*, because they determine the number of particles that assemble in one location, and how they pack together. The medium viscosity η_m does not affect the local particle packing density. The maximum achievable local particle packing density is 45%, independent of particle size *a* and medium viscosity η_m.

Third, we quantify and predict the transient local particle packing density of spherical particles within the pattern features that result from ultrasound DSA. We also characterize the effect of process parameters such as particle size *a*, particle volume fraction φ, and medium viscosity η_m on the transient local particle packing density. The local particle packing density increases with increasing time, due to increasing number of particles that assemble at a specific location, then reaches steady-state when almost all particles have assembled into the specific location. Increasing the particle volume fraction Φ first increases and then decreases the packing time due to ultrasound wave scattering, collision between particles, and the change in initial and final local particle packing densities. Increasing the particle size or decreasing fluid medium viscosity both increase the velocity with which particles move towards the locations where they assemble and, thus, decreases the packing time.

Finally, we implement single and multiple scattering in the calculation of the acoustic radiation force for spherical particles in a viscous medium and characterize and quantify their relative contributions to the calculation of the acoustic radiation force as a function of ultrasound DSA operating parameters and material properties. The deviation between the acoustic radiation force derived from single and multiple scattering may reach up to 100%. Thus, neglecting multiple scattering in favor of computationally efficient single scattering is not always correct. The

maximum deviation between the acoustic radiation force derived from single and multiple scattering increases with decreasing particle size, increasing medium viscosity, increasing density ratio ρ_p/ρ_m, or increasing compressibility ratio β_p/β_m, largely driven by increasing dipole scattering. Comparing a fundamental three-particle system to a large-scale system of particles demonstrates that increasing the particle volume fraction Φ increases the need to account for multiple scattering.

These results provide a physical understanding of the ultrasound DSA process in a viscous medium and enable characterizing the effect of the ultrasound DSA process parameters on the steady-state and transient location and local packing density of spherical particles that results from ultrasound DSA. In addition, these results enable quantifying and predicting the location where spherical particles assemble and the local packing density of spherical particles during and after ultrasound DSA in a viscous medium, as a function of ultrasound DSA process parameters and time. Both measurements are crucial in the context of using ultrasound DSA in engineering applications, in particular manufacturing engineered polymer matrix composite materials with tailored properties whose properties depend on the spatial organization and packing density of particles in the matrix material.